AD NUMBER
ADC018009
CLASSIFICATION CHANGES
TO: unclassified
FROM: secret
LIMITATION CHANGES
TO: Approved for public release, distribution unlimited
FROM: Controlling DoD Organization. Naval Electronic Systems Command, Washington, DC 20360.
AUTHORITY
ONR ltr, 31 Jan 2006; ONR ltr, 31 Jan 2006

ARL-TR-78-1

Copy No. 19

MOORED SURVEILLANCE SYSTEM FIELD VALIDATION TEST SENSOR PERFORMANCE ANALYSIS (U)

Final Report under Contract N00039-77-C-0003, Items 0003 and 0004

VOLUME I
DATA COLLECTION AND MEASUREMENT SYSTEM DESCRIPTION (U)

Steven L. Watkins
Clark S. Penrod

APPLIED RESEARCH LABORATORIES
THE UNIVERSITY OF TEXAS AT AUSTIN
POST OFFICE BOX 8029, AUSTIN, TEXAS 78712

31 December 1978

Final Report

10 January 1977 - 31 March 1978

Prepared for:

NAVAL ELECTRONIC SYSTEMS COMMAND
DEPARTMENT OF THE NAVY
WASHINGTON, D.C. 20360

NATIONAL SECURITY INFORMATION
UNAUTHORIZED DISCLOSURE
SUBJECT TO CRIMINAL SANCTIONS

SECURITY CLASSIFICATION OF THIS PAGE (When Data Entered)

REPORT DOCUMENTATION PAGE		READ INSTRUCTIONS BEFORE COMPLETING FORM
1. REPORT NUMBER	2. GOVT ACCESSION NO.	3. RECIPIENT'S CATALOG NUMBER
4. TITLE (and Subtitle) MOORED SURVEILLANCE SYSTEM FIELD VALIDATION TEST SENSOR PERFORMANCE ANALYSIS. (U) VOLUME I. DATA COLLECTION AND MEASUREMENT SYSTEM DESCRIPTION (U).		5. TYPE OF REPORT & PERIOD COVERED final report. 10 JAN 77 - 31 MAR 78. 6. PERFORMING ORG. REPORT NUMBER ARL-TR-78-1
7. AUTHOR(s) Steven L. Watkins Clark S. Penrod		8. CONTRACT OR GRANT NUMBER(s) N00039-77-C-0003
9. PERFORMING ORGANIZATION NAME AND ADDRESS Applied Research Laboratories The University of Texas at Austin Austin, Texas 78712		10. PROGRAM ELEMENT, PROJECT, TASK AREA & WORK UNIT NUMBERS Items 0003 and 0004
11. CONTROLLING OFFICE NAME AND ADDRESS Naval Electronic Systems Command Department of the Navy Washington, DC 20360		12. REPORT DATE 31 December 1978 13. NUMBER OF PAGES
14. MONITORING AGENCY NAME & ADDRESS (if different from Controlling Office)		15. SECURITY CLASS. (of this report) SECRET 15a. DECLASSIFICATION/DOWNGRADING SCHEDULE See reverse side.

16. DISTRIBUTION STATEMENT (of this Report)

None

17. DISTRIBUTION STATEMENT (of the abstract entered in Block 20, if different from Report)

18. SUPPLEMENTARY NOTES

19. KEY WORDS (Continue on reverse side if necessary and identify by block number)

rapidly deployable surveillance system
moored surveillance system
DIFAR

20. ABSTRACT (Continue on reverse side if necessary and identify by block number)

(U) Volume I of the Moored Surveillance System Field Validation Test Senso. Performance Analysis contains a description of the systems employed to collect and extract measurements from the recorded data. Included are descriptions of both the ACODAC systems and the ARL:UT measurement system.

DD FORM 1 JAN 73 1473 EDITION OF 1 NOV 65 IS OBSOLETE

15a.

DD 254, 12/10/76,
Cont. N00039-77-C-0003
CLASSIFIED BY OPNAVINST S5510.72C, 4 Sep 73
EXEMPT FROM GDS OF E.O. 11652
EXEMPTION CATEGORY 3
DECLASSIFIED ON 31 Dec 2007

"NATIONAL SECURITY INFORMATION"

"Unauthorized Disclosure Subject to Criminal Sanctions"

TABLE OF CONTENTS

(The reverse of this page is blank.)

LIST OF FIGURES

LIST OF FIGURES (Cont'd)

LIST OF TABLES

(The reverse of this page is blank.)

I. INTRODUCTION

(C) During November 1975, the Moored Surveillance System (MSS) Field Validation Test (FVT) was conducted under the sponsorship of the MSS Project Office (PME 124-30) of Naval Electronic Systems Command. Applied Research Laboratories, The University of Texas at Austin (ARL:UT), participated in the processing and analysis of he acquired data. This report contains the results of the work performed under Contract N00039-77-C-0003. The purpose of this report is to provide measurements and analyses of candidate sensor performance based on data from the MSS-FVT.

(U) This report is partitioned into four volumes. Volume I describes the data collection system and the measurement system used to obtain these results. Volume II contains the detailed data products obtained with standard frequency resolution processing. Volume III contains the detailed data products obtained with vernier frequency resolution processing. Volume IV contains the background information, summary data products, and analysis.

(U) Since the MSS-FVT was completed, the name of the MSS program has been changed to Rapidly Deployable Surveillance System (RDSS). Not only the name but also the scope and requirements of the program have undergone major revisions. To avoid ambiguity, the term MSS will be used throughout this report; however, the issues addressed herein are those of current interest to RDSS, as specified by the project office at the time that this report was written.

(U) Volume I is intended to provide a description of the complete data collection and measurement system used to obtain the results contained in Volumes II through IV. The contents of this volume are divided into seven sections. Section II describes the sensors whose performance is

(U) evaluated by this report. Section III briefly describes the data collection and preprocessing systems that input to the ARL:UT measurement system (Fig. I-1). The fourth through sixth sections describe the three major components of the ARL:UT system (Fig. I-2): A/D Conversion and Data Reduction, Ambient Sound Field Measurement Techniques, and cw Measurement Techniques. The final section contains recommendations pertaining to future performance analyses.

(C) The sensor performance measurements and analyses contained in this report do not address the entire MSS processing scheme. This effort was designed to directly address the following issues.

- DIFAR and differenced DIFAR beamformer performance improvements over an omnidirectional sensor.
- Signal, noise, and array gain measurements for an MSS candidate deep moored sensor.
- Bearing accuracy/performance achievable with the ACODAC system/MSS candidate acoustic array.
- Clutter related (line loading) statistics for a deep moored acoustic array.

Issues involving signature formation, classification, interbuoy target formation, localization, field management, or field performance are not directly addressed.

(C) At the time that this work was initiated, the ARL:UT measurement system did not contain many of the required features (i.e., DIFAR beamforming and clutter measurements). The sponsor provided ARL:UT with an outline of the desired measurement system characteristics and a set of suggested algorithms (Ref. 1). Much of the time and resources expended on this effort were used to implement these features. It was then found that the specified line formation and line tracking algorithms did not perform well on these data. These algorithms were subsequently revised by ARL:UT because a reasonable performance level was required for the execution of this work.

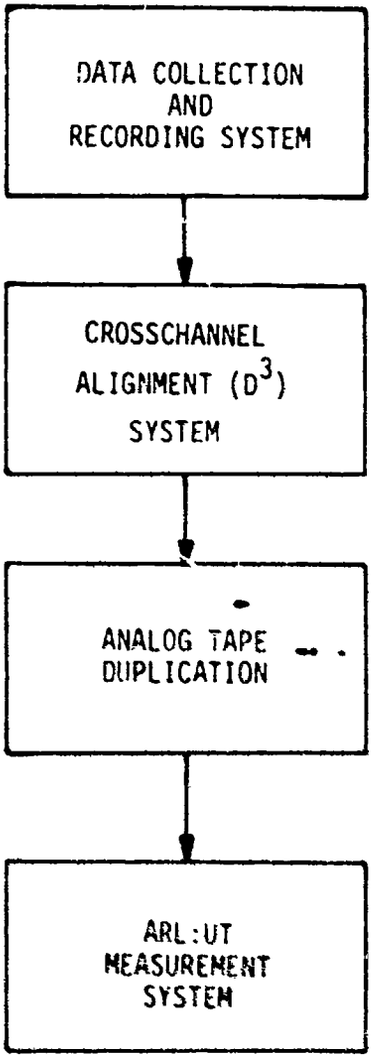

FIGURE 1-1
PREPROCESSING DATA PATH

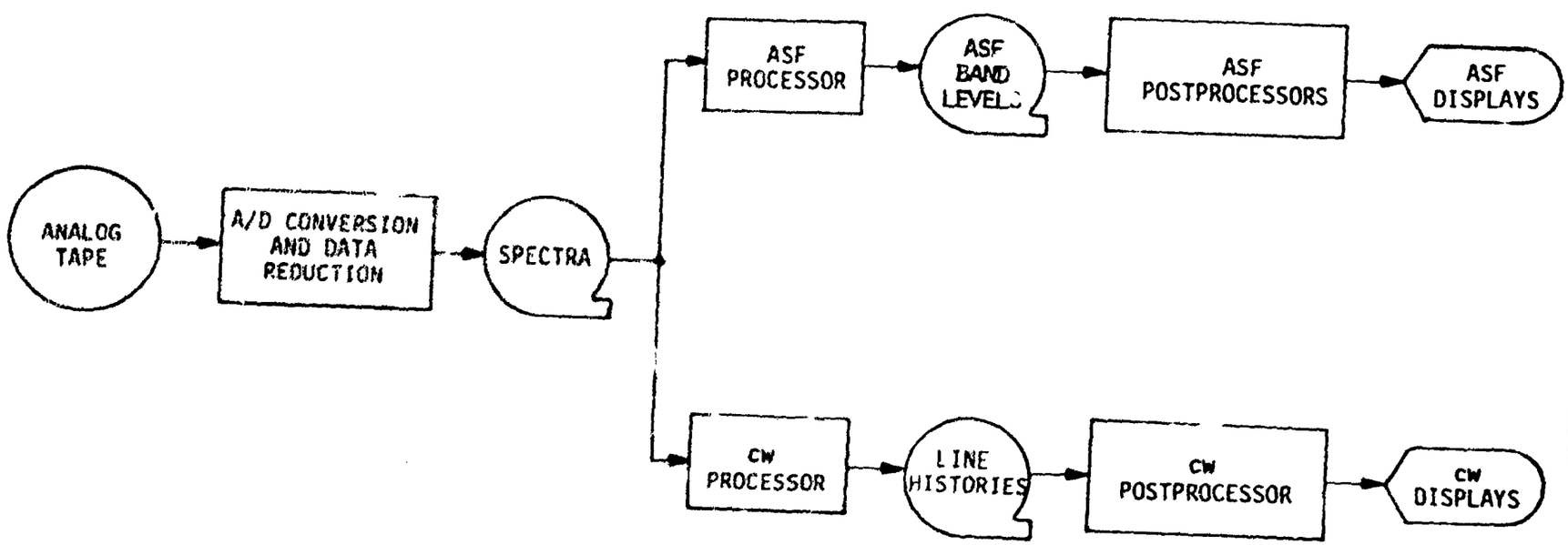

FIGURE I-2
ARL:UT MEASUREMENT SYSTEM OVERVIEW

AS-79-32

(U) There are currently in existence several different systems which have been used to measure sensor performance. Each of these systems was designed with different constraints and goals, and their designers frequently chose to use significantly different algorithms. This report is intended to furnish sensor performance measurements which can be compared with those from other measurement systems. To help facilitate such comparisons, the ARL:UT algorithms and their associated assumptions and models are herein described. Since the ARL:UT system functions in a laboratory environment without the usual realtime or tactical constraints, most of the timing, hardware, and formatting details have been deleted.

(The reverse of this page is blank.)

II. SENSOR DESCRIPTIONS

(C) The MSS candidate sensors for this study were derived from the outputs of a pair of DIFAR arrays. Each DIFAR array outputs three channels of information. The first channel contains the output of an omnidirectional hydrophone. The other two channels contain the output of collocated horizontal first-order pressure gradients. One gradient channel has its main response axis oriented north/south, and the other east/west. The output on each of these channels due to a plane wave of frequency f and amplitude p which is incident horizontally to the array at an angle θ east of north can be expressed as

$x_o(t) = p \sin\omega t$ Omnidirectional Channel,
$x_c(t) = p \cos\theta \sin\omega t$ North/South (cosine) Channel, and
$x_s(t) = p \sin\theta \sin\omega t$ East/West (sine) Channel,

where $\omega=2\pi f$. These gradient channels have the familiar dipole directivity pattern (Fig. I-3).

(C) It will be assumed that the response function of each channel is rotationally symmetric about its main response axis. Therefore, if the above described plane wave is now incident at an angle γ above horizontal, the three outputs can be expressed as

$$x_o(t) = p \sin\omega t \quad ,$$
$$x_c(t) = p \cos\theta \cos\gamma \sin\omega t \quad , \text{ and}$$
$$x_s(t) = p \sin\theta \cos\gamma \sin\omega t \quad .$$

It should be noted that both gradient channels null out any signals arriving from directly above or below ($\gamma=\pm 90°$) the array.

(U) DIFAR horizontal beamforming is usually accomplished as a weighted summation of the three channels:

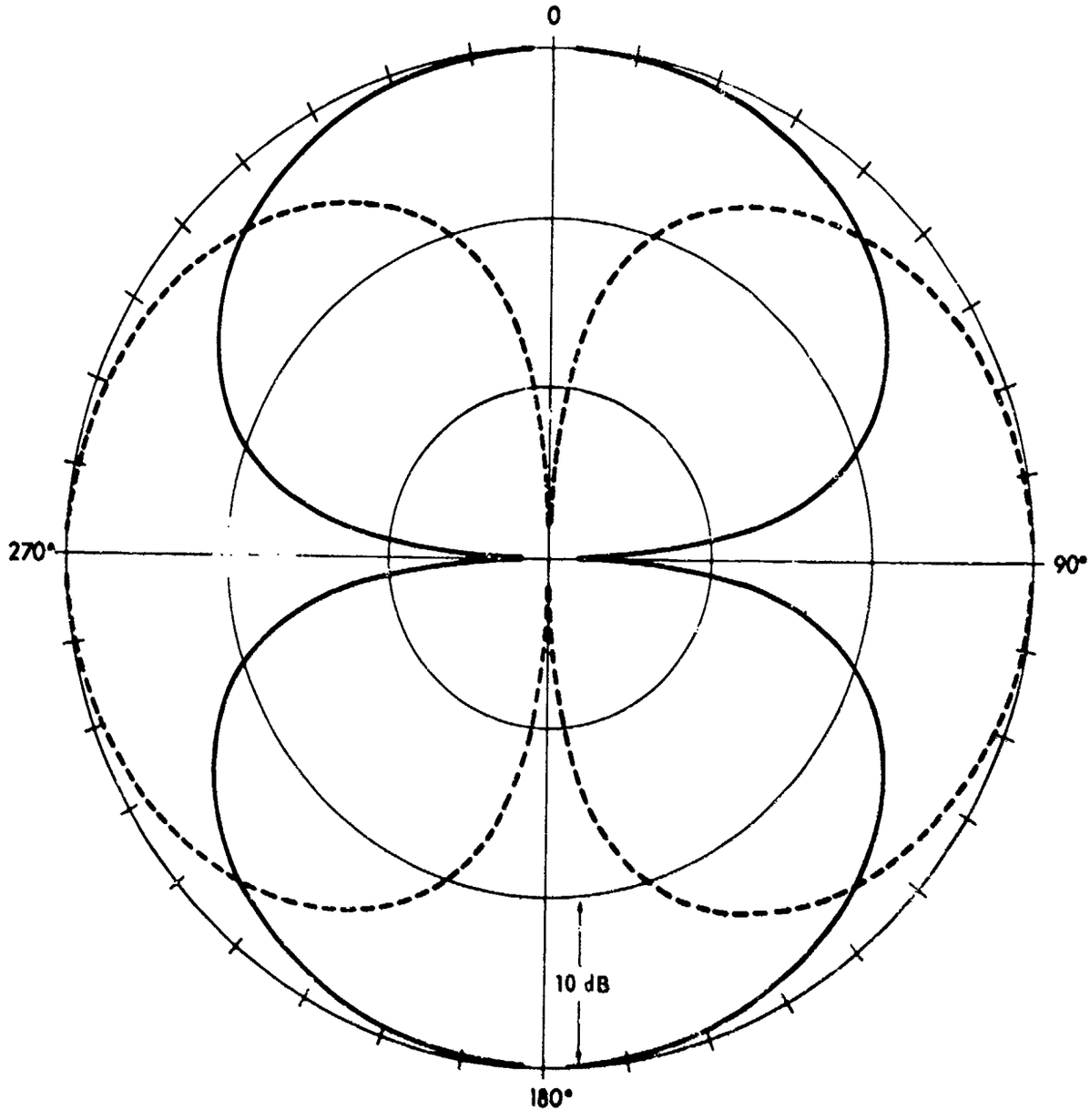

FIGURE I-3
DIFAR ELEMENT BEAM PATTERNS

ARL-UT
AS-70-49
SLW-GA
3-8-78

(C) $$y(t,\phi) = [\alpha x_o(t)+\cos\phi x_c(t)+\sin\phi x_s(t)]/(1+\alpha)$$

$$= p\ \sin\omega t[\alpha+\cos\gamma(\cos\phi\ \cos\theta+\sin\phi\ \sin\theta)]/(1+\alpha) \quad . \tag{1}$$

The present formulation assumes that both directional channels are weighted by the same nondirectional constant which has been equivalently represented as a single omni weight factor α. When a beam is formed towards the incoming plane wave ($\phi=\theta$),

$$y(t,\theta) = p\ \sin\omega t[\alpha+\cos\gamma]/(1+\alpha) \quad .$$

Note that, if the plane wave is not horizontally incident ($\gamma=0$), the beamformer response will be less than that of the omnidirectional channel. The beam patterns of the above described DIFAR beamformer are termed limacons. The shape of these limacons can be controlled by the omni weight factor α. Limacon plane wave beam patterns for typical omni weight factors are shown in Fig. I-4. Each of these responses is also rotationally symmetric about this main response axis. The limacon formed by setting $\alpha=1.0$ is referred to as a cardioid.

(C) Some of the MSS candidate sensors currently under consideration consist of four orthogonal limacons. Their beamformer can be expressed from Eq. (1) as

$$y(t,0°) = [\alpha x_o(t)+x_c(t)]/(1+\alpha) \quad \text{North,}$$

$$y(t,90°) = [\alpha x_o(t)+x_s(t)]/(1+\alpha) \quad \text{East,}$$

$$y(t,180°) = [\alpha x_o(t)-x_c(t)]/(1+\alpha) \quad \text{South, and}$$

$$y(t,270°) = [\alpha x_o(t)-x_s(t)]/(1+\alpha) \quad \text{West} \quad .$$

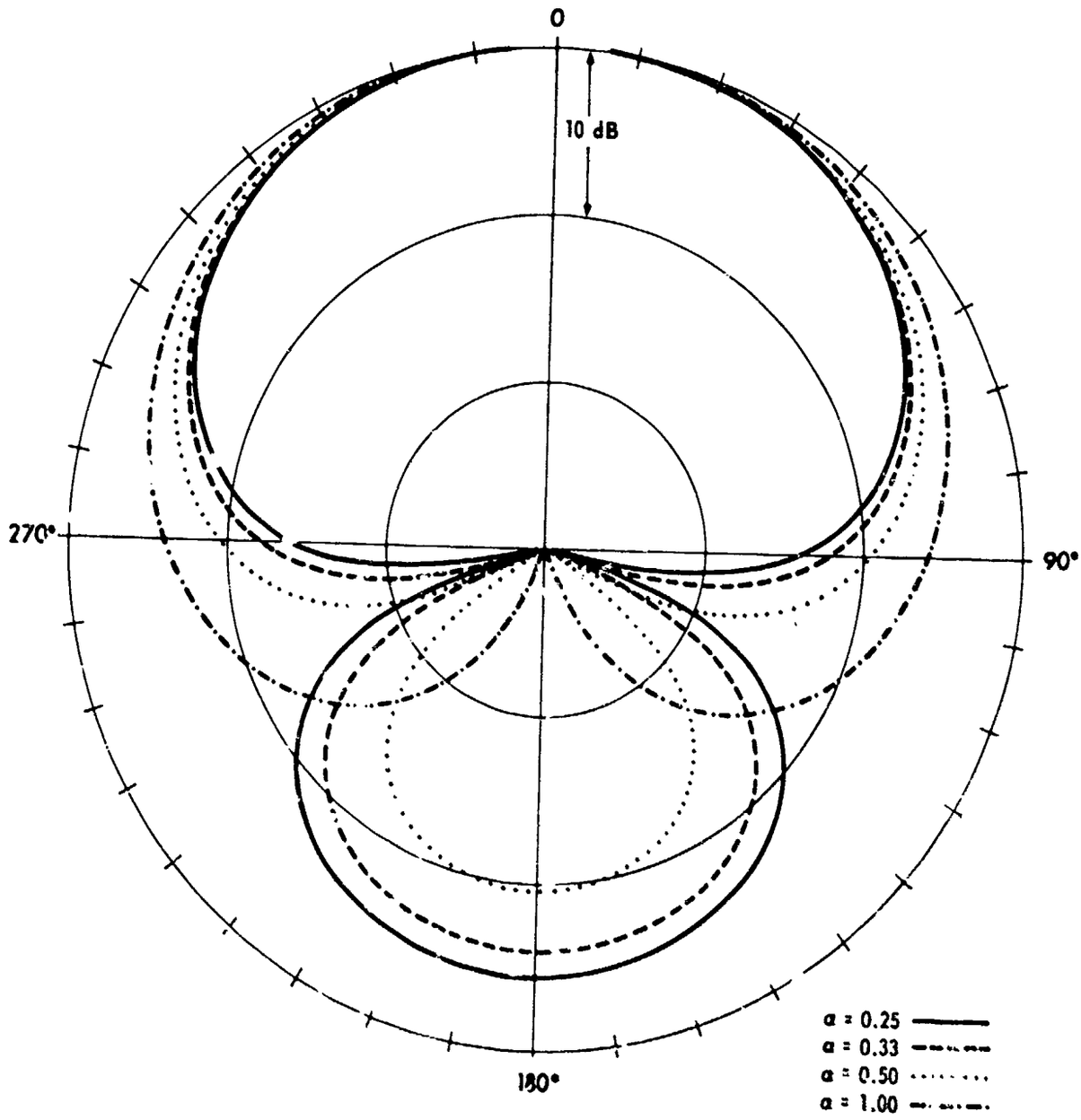

FIGURE I-4
LIMACON BEAM PATTERNS

ARL:UT
AS-78-492
SLW-GA
3-8-78

(C) A simplified block diagram of this beamformer, through Automatic Line Integration (ALI), is shown as Fig. I-5. When the omni weight factor is set to 1.0, the beamformer output consists of four cardioids (Fig. I-6). This configuration is termed the single cardioids sensor and will be referred to throughout this report.

(C) The time domain beamformer discussed earlier is not an efficient technique, because each of the four output channels must be Fourier transformed. A more efficient technique would be to transform each of the three input channels before beamforming. Let the Fourier transform of each DIFAR channel be approximated by

$$X(f) = \frac{1}{N} \sum_{t=0}^{N-1} x(t) e^{-i\omega t/N} \quad ,$$

where $i=\sqrt{-1}$. Letting Y(f) be an observation vector,*

$$Y(f) = \begin{bmatrix} X_o(f) \\ X_c(f) \\ X_s(f) \end{bmatrix} \quad ,$$

and $V(\phi)$ be a steering vector,

$$V(\phi) = \begin{bmatrix} \alpha \\ \cos\phi \\ \sin\phi \end{bmatrix}$$

---

*Much of the following discussion follows that of Ref. 2.

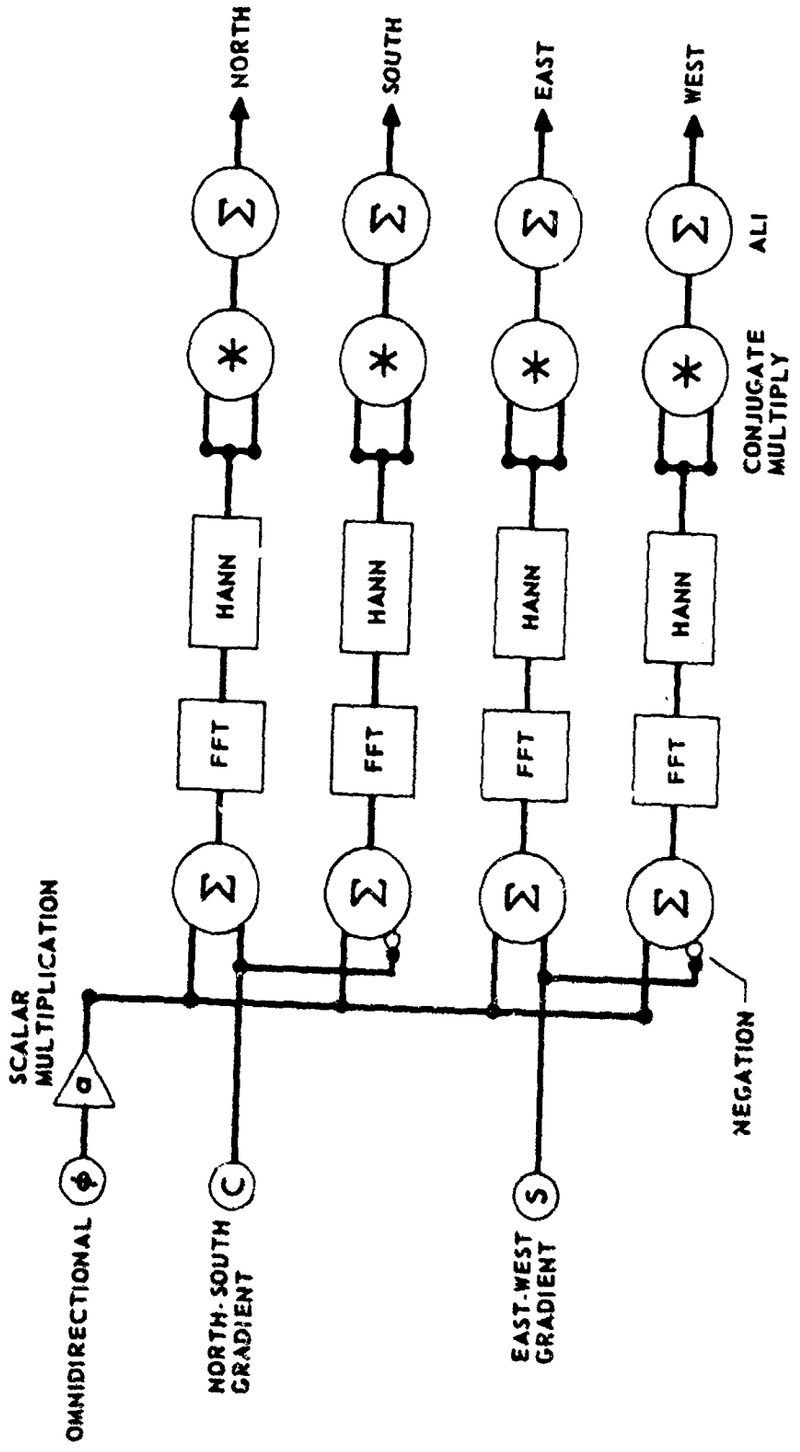

FIGURE I-5
TIME DOMAIN LIMACON BEAMFORMER (U)

ARL:UT
AS-78-647
SLW-GA
4-20-78

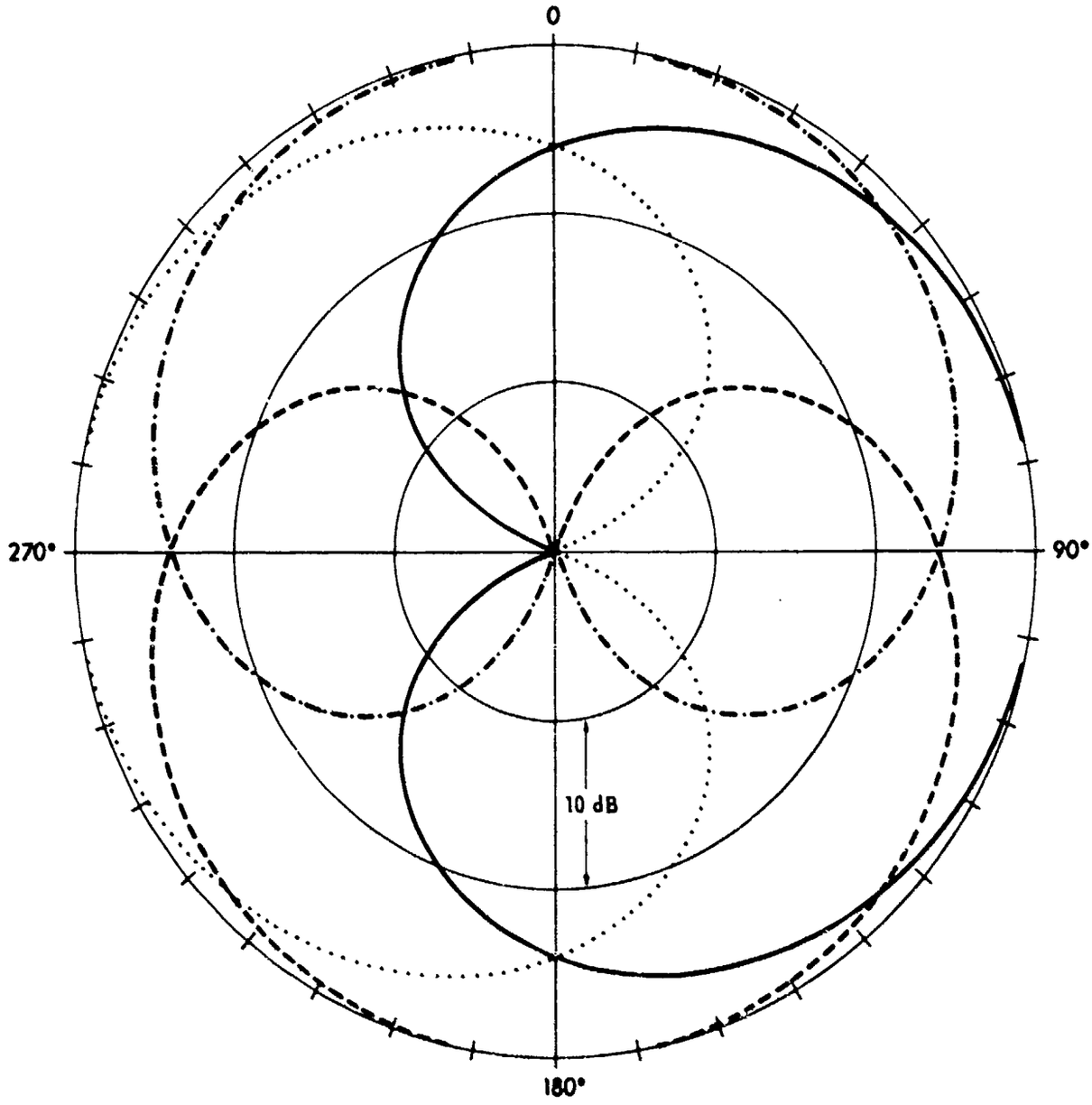

FIGURE I-6
ORTHOGONAL CARDIOID BEAM PATTERNS

ARL UT
AS-78-493
SLW-GA
3-8-78

(C) The beamformer output becomes

$$A(f,\phi) = V^*(\phi)\ Y(f) \quad ,$$

where * denotes the complex conjugate transpose operation. For sensors composed of our orthogonal limacons, $A(f,\phi)$ becomes

$$A(f,0°) = [\alpha X_o(f)+X_c(f)] \quad \text{North} \quad ,$$

$$A(f,90°) = [\alpha X_o(f)+X_s(f)] \quad \text{East} \quad ,$$

$$A(f,180°) = [\alpha X_o(f)-X_c(f)] \quad \text{South} \quad ,$$

$$A(f,270°) = [\alpha X_o(f)-X_s(f)] \quad \text{West} \quad .$$

The beamformer angular power response is then computed as

$$\sigma(f,\phi) = A(f,\phi)A^*(f,\phi) \quad .$$

A block diagram of this Fourier coefficient beamformer is shown as Fig. I-7.

(C) The ARL:UT measurement is intended to serve as a tool for investigating sensor performance. As an investigative tool, it is desirable to save the DIFAR data at a point prior to where it is formed into specific beams, but after it has incurred most of its computational overhead (i.e., FFT). For the time domain beamformer, this would require saving the time series. For Fourier coefficient beamforming, this would require saving each complex Fourier transform. An alternative technique, which meets the desired criteria, is to compute and save cross-spectra

$$Q(f) = \frac{1}{N} \sum_{K=1}^{N} Y_K(f)\ Y_K^*(f) \quad .$$

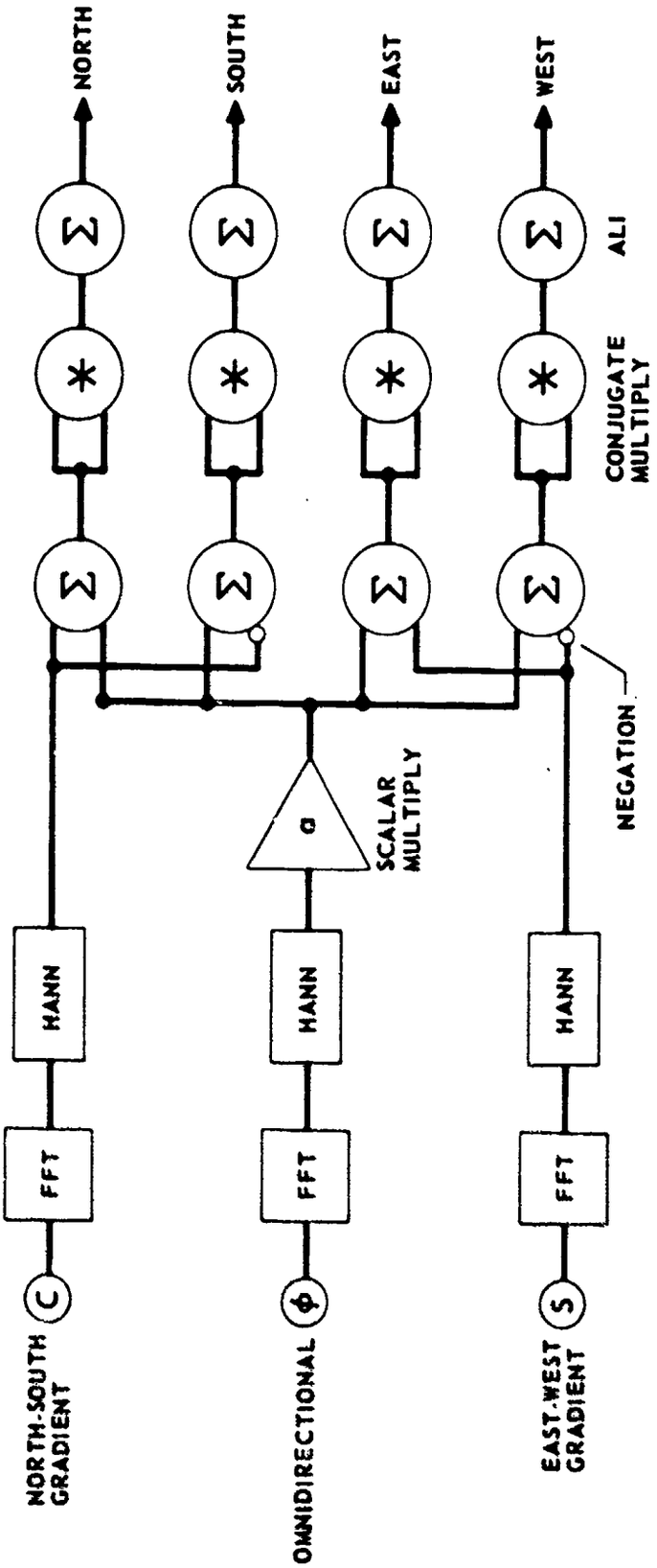

FIGURE I-7
FOURIER COEFFICIENT LIMACON BEAMFORMER (U)

ARL UT
AS-78-648
SLW-GA
4-20-78

(C) The properties of DIFAR cross-spectra are discussed in Ref. 2. A few of the most important properties are summarized below.

(1) Because the DIFAR elements are spaced much less than a wavelength apart, the acoustic signals on all three channels are in phase.

(2) Because the channels are all in phase, each element q_{ij} of Q is real.

(3) Q is symmetric about its main diagonal, that is, $q_{ij}=q_{ji}$.

(4) If the signal and noise are zero mean Gaussian, then Q contains all of the information contained in the sequence of observations. The DIFAR beamformer angular response now becomes

$$\sigma(f,\phi) = V^*(\phi)\ Q(f)\ V(\phi) \quad .$$

Carrying out the indicated matrix operations yields

$$\sigma(f,\phi) = (C_1+C_2\cos\phi+C_3\sin\phi+C_4\cos 2\phi+C_5\sin 2\phi)/(1+\alpha)^2 \quad , \qquad (2)$$

where

$$C_1 = \alpha^2 q_{11} + (q_{22}+q_{33})/2$$

$$C_2 = 2\alpha q_{12}$$

$$C_3 = 2\alpha q_{13}$$

$$C_4 = (q_{22}-q_{33})/2$$

$$C_5 = q_{23} \quad .$$

It should be noted that the above expression has the form of a Fourier series in ϕ. This implies that Q contains information about an isotropic term, as well as two directional terms. This further implies that this beamformer can discriminate between two signal arrivals in the same frequency cell. The Fourier series also suggests that an inverse FFT can be used to efficiently form a large number of equispaced beams.

(C) For the special case of four orthogonal limacons, the beamformer outputs become

$$\sigma(f,0°) = C_1 + C_2 + C_4 = (\alpha^2 q_{11} + 2\alpha q_{12} + q_{22})/(1+\alpha)^2 \quad \text{North} \quad ,$$

$$\sigma(f,90°) = C_1 + C_3 - C_4 = (\alpha^2 q_{11} + 2\alpha q_{13} + q_{33})/(1+\alpha)^2 \quad \text{East} \quad ,$$

$$\sigma(f,180°) = C_1 - C_2 + C_4 = (\alpha^2 q_{11} - 2\alpha q_{12} + q_{22})/(1+\alpha)^2 \quad \text{South, and}$$

$$\sigma(f,270°) = C_1 - C_3 - C_4 = (\alpha^2 q_{11} - 2\alpha q_{13} + q_{33})/(1+\alpha)^2 \quad \text{West} \quad .$$

A block diagram of this beamformer is shown as Fig. I-8. It should be noted that both the FFT and ALI occur prior to beam formation. This is the beamformer configuration used for this study. The cross-spectra were preserved following ALI. Preservation of Q required saving six real numbers for each frequency cell, only five of which are used by the four-limacon beamformer. The complete presentation of Q allows beams to be formed in any direction via Eq. (2). It also permits application of optimal and/or adaptive techniques such as those described in Ref. 3 and applied to DIFAR in Ref. 2.

(C) The various limacon beams described above can be formed from a single DIFAR array. Because of their rotational symmetry, the horizontal response of such beams is also their vertical response. As stated earlier, the array configuration for this study consisted of a pair of DIFAR arrays. These arrays were arranged one above the other with a spacing of 6.1 m (20 ft). The lower DIFAR array (B) was used as described above to form various limacons, and its omnidirectional channel was used as the reference for measuring relative performance between sensors. Each channel of the upper DIFAR array (A) was subtracted from the corresponding channel of the lower DIFAR array (B-A) to yield what is termed differenced DIFAR channels. This can be expressed as

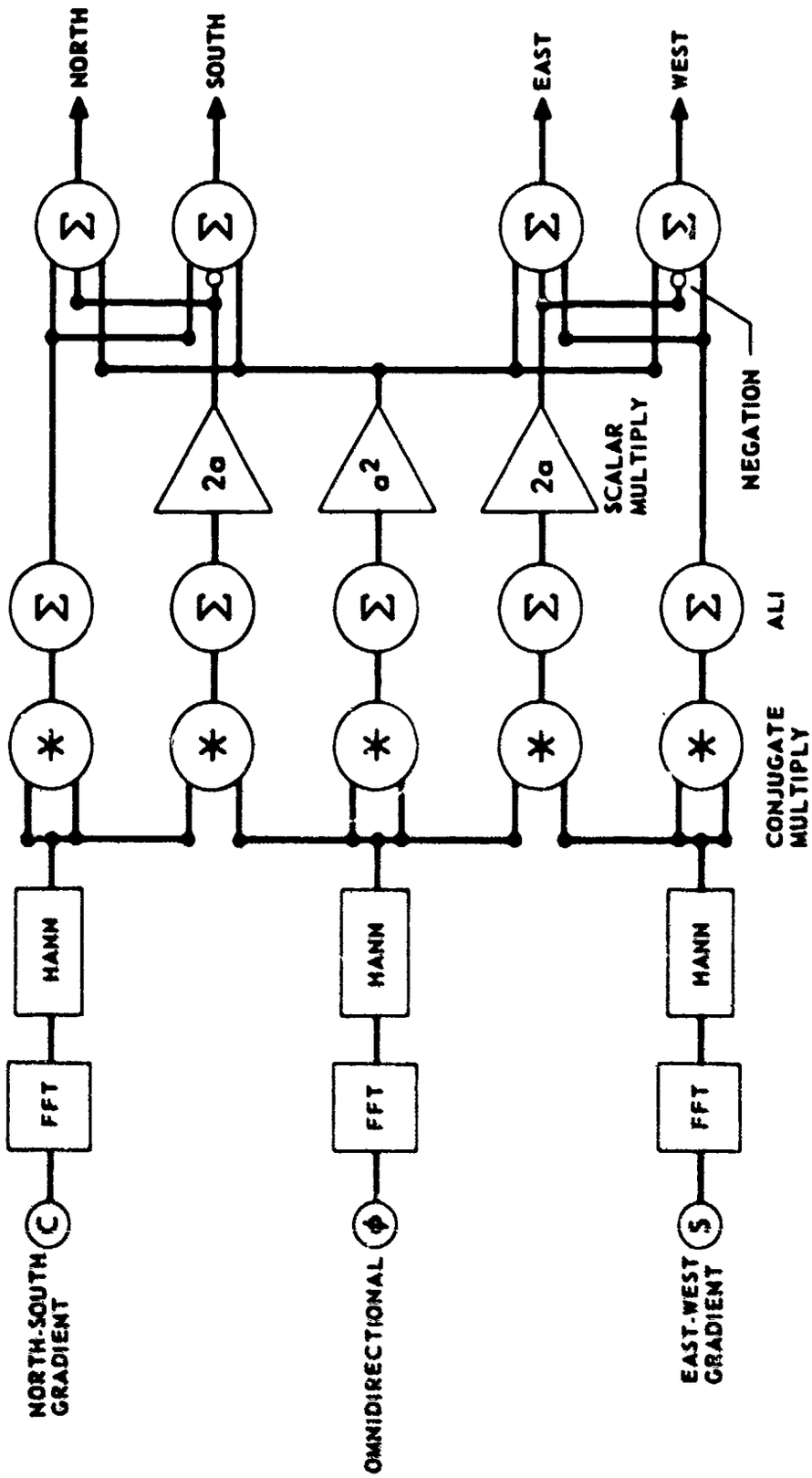

FIGURE I-8
CROSS-SPECTRAL MATRIX LIMACON BEAMFORMER (U)

ARL UT
AS-78446
SLW-GA
4-20-78

(C) $x_o^{B-A}(t) = x_o^B(t) - x_o^A(t)$ Differenced Omnidirectional Channel,

$x_c^{B-A}(t) = x_c^B(t) - x_c^A(t)$ Differenced North/South (cosine) Channel, and

$x_c^{B-A}(t) = x_s^B(t) - x_s^A(t)$ Differenced East/West (sine) Channel .

The purpose of this arrangement was to achieve a horizontal null at all frequencies. The horizontal response of these differenced channels is the same as the response of the single DIFAR channels. However, the vertical response is different and is frequency dependent.

(C) Given a plane wave of frequency f incident to the array at a horizontal bearing angle $\theta°$ east of north, and a vertical angle $\gamma°$ above horizontal, the response of a single DIFAR array limacon with a horizontal steer angle of ϕ, relative to the response of the omnidirectional sensor, is

$$b_s(\theta,\gamma,\phi,a) = [a+\cos\gamma(\cos\phi\cos\theta+\sin\phi\sin\phi)]/(1+a) \quad .$$

The angle θ then corresponds to the horizontal bearing of the incident plane wave in degrees east of north, while ϕ is the horizontal steering angle for the DIFAR beam, also in degrees east of north. The angle γ is the vertical incidence angle of the plane wave measured in degrees above horizontal. Without loss of generality, choose $\phi=0°$; then

$$b_s(\theta,\gamma,a) = (a+\cos\gamma\cos\theta)/(1+a) \quad .$$

The response of the differenced omnidirectional channel is

$$b_{vp}(f,\gamma) = \sin\left(\frac{\pi f d}{c_o}\sin\gamma\right) \quad ,$$

where d is the hydrophone separation and c_o is the sound speed in the vicinity of the array. This sensor will be referred to throughout this

(C) report as the vertical dipole sensor. Vertical plane wave beam patterns at approximate frequencies of interest are shown in Fig. I-9. In this figure and Fig. I-10, 0° and 180° correspond to horizontal arrival angles, while 90° corresponds to a vertical arrival angle from the surface. The response of the differenced DIFAR array limacons can be obtained, by the product theorem (Ref. 4), as the product of the single limacon and vertical dipole responses,

$$b_D(f,\theta,\gamma,\alpha) = b_s(\theta,\gamma,\alpha)\, b_{vd}(f,\gamma)$$

$$= (\alpha+\cos\gamma\cos\theta)\, \sin\frac{\pi f d}{c_o}\sin\gamma)/(1+\alpha) \quad .$$

The only differenced limacons included in this study were differenced cardioids (α=1). Differenced cardioid vertical plane wave patterns at approximate frequencies of interest are shown in Fig. I-10.

(C) The receiving directivity index (DI) of a beam is defined as (Ref. 4)

$$DI = 10 \log \frac{\int_s d\Omega}{\int_s b^2(\theta,\gamma)\, d\Omega} \quad .$$

For 3-dimensional isotropic noise, the single limacon directivity index is (Fig. I-11(a))

$$DI(\alpha) = 10 \log \left[(1+\alpha)^2 \Big/ \left(\alpha^2+\frac{1}{3}\right)\right] \quad .$$

The directivity index for single cardioids (α=1) is 4.77 dB. The maximum DI occurs at α=1/3, where the DI is 6.02 dB. Single DIFAR array limacons formed with α=1/3 are referred to in this study as maximum gain limacons.

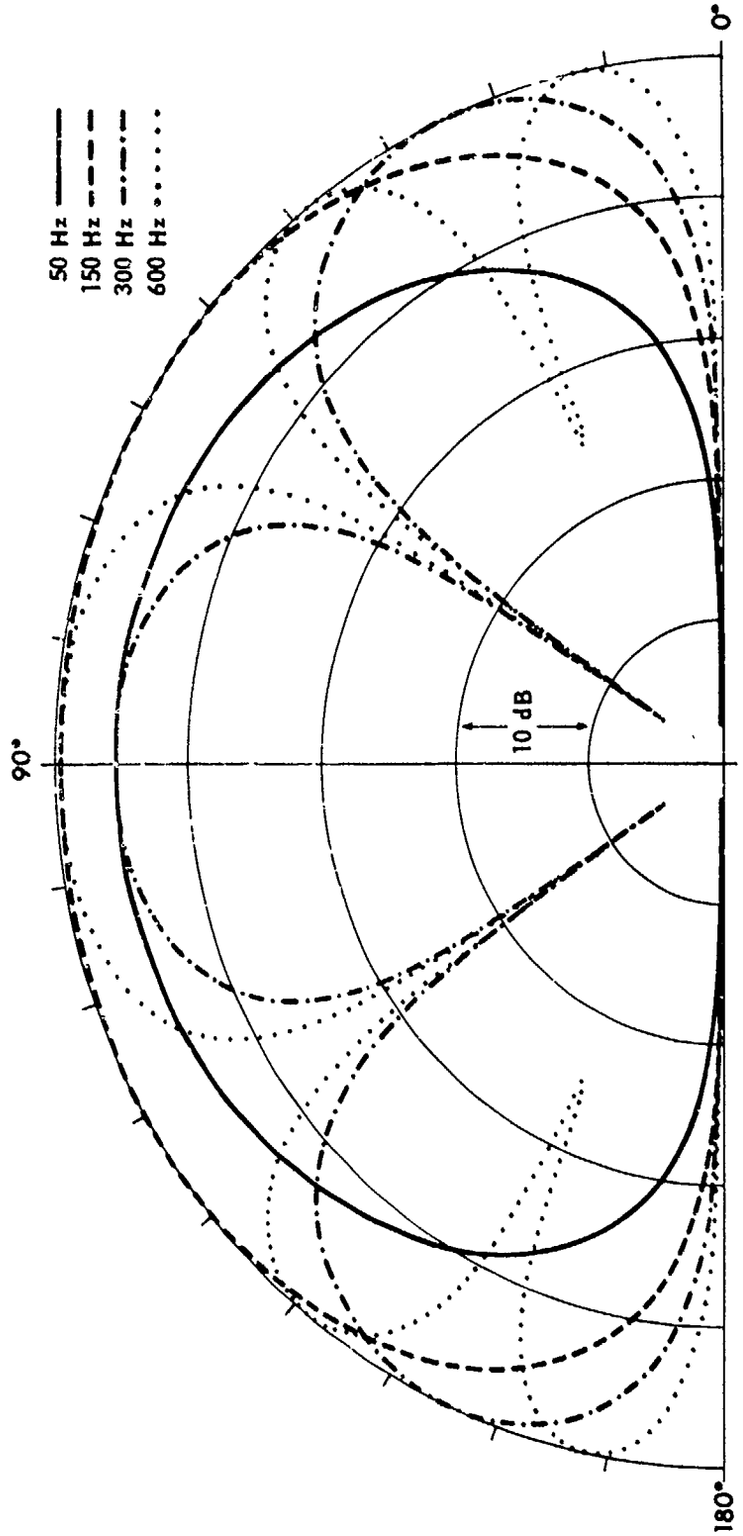

FIGURE I-9
VERTICAL DIPOLE VERTICAL BEAM PATTERNS

ARL:UT
AS-78-494
SLW-GA
3-8-78

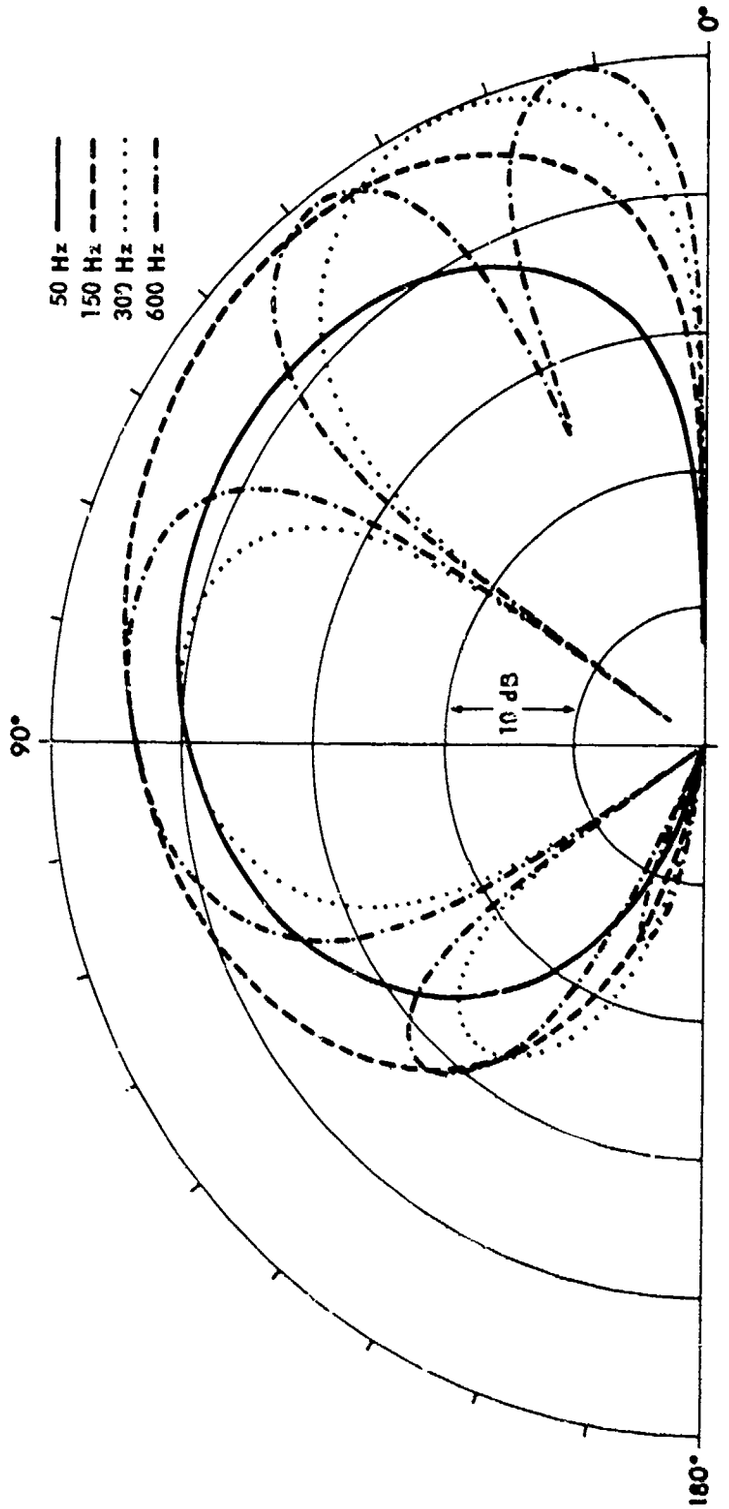

FIGURE I-10
DIFFERENCED CARDIOID VERTICAL BEAM PATTERNS

ARL:UT
AS-78-495
SLW-GA
3-8-78

(C) In an environment where all of the noise is arriving horizontally at the array, it is appropriate to compute DI with a 2-dimensional horizontally isotropic noise field. This result is (Fig. I-11(a))

$$DI(\alpha) = 10 \log\left[(1+\alpha)^2 \Big/ \left(\alpha^2 + \frac{1}{2}\right)\right] \quad .$$

The corresponding DI for single cardioids is 4.26 dB, and the maximum DI occurs at α=0.5, where the DI is 4.77 dB. This type of noise field has been assumed for BEARTRAP DIFAR/KANDE processing (Ref. 5).

(C) All of the DIFAR derived sensors considered in this study consist of four orthogonal limacons. The minimum horizontal response of such sensors will occur halfway between the main axis of adjacent beams (45°). The response at selected angles relative to that of the omnidirectional sensor is shown in Fig. I-11(b). The minimum response for the single cardioids sensor is -1.38 dB, and is -2.15 dB for the maximum gain limacons sensor.

(C) The directivity index of the vertical dipole sensor in a 3-dimensional isotropic noise field is (Ref. 6)

$$DI(f) = 10 \log\left[\frac{2}{1 - J_o(2\pi fd/c_o)}\right]$$

$$= 3.01 - 10 \log[1-J_o(0.025f)] \quad ,$$

where $J_o(x)$ is the Bessel function of the first kind and zero order. (Recall that at frequencies below approximately 125 Hz, the peak array response is less than unity, and therefore the above expression is not the usual DI.) This result is plotted as a function of frequency in Fig. I-11(c). This sensor was primarily intended for use only below 2[illegible] Hz, where the hydrophone spacing is less than a wavelength. At frequencies less than approximately 125 Hz, the main response axis is vertical and the maximum plane wave response is always less than that

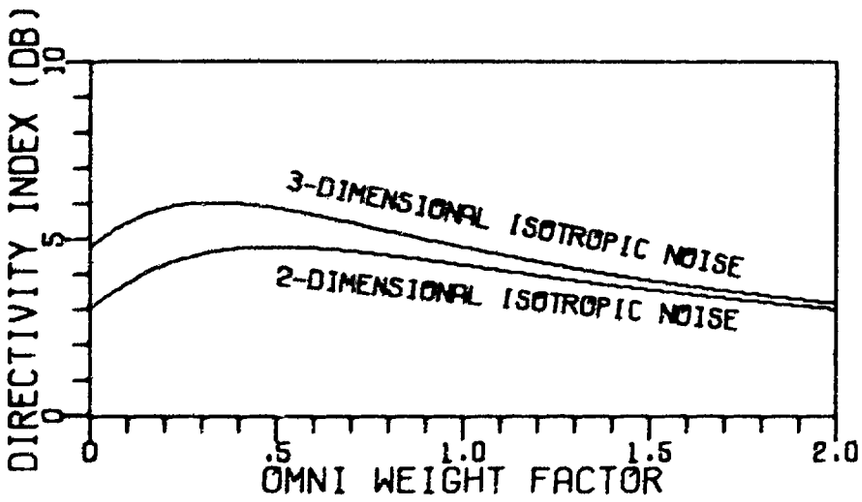

A) LIMACON DIRECTIVITY INDEX VS. OMNI WEIGHT FACTOR

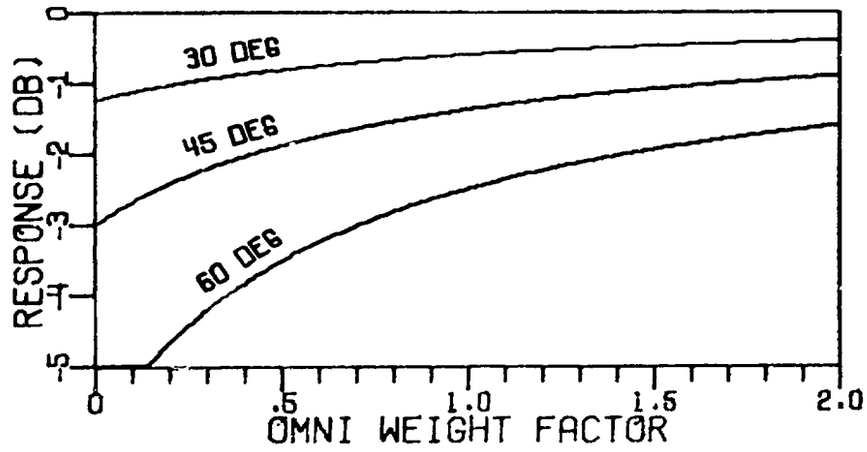

B) LIMACON RESPONSE VS. OMNI WEIGHT FACTOR

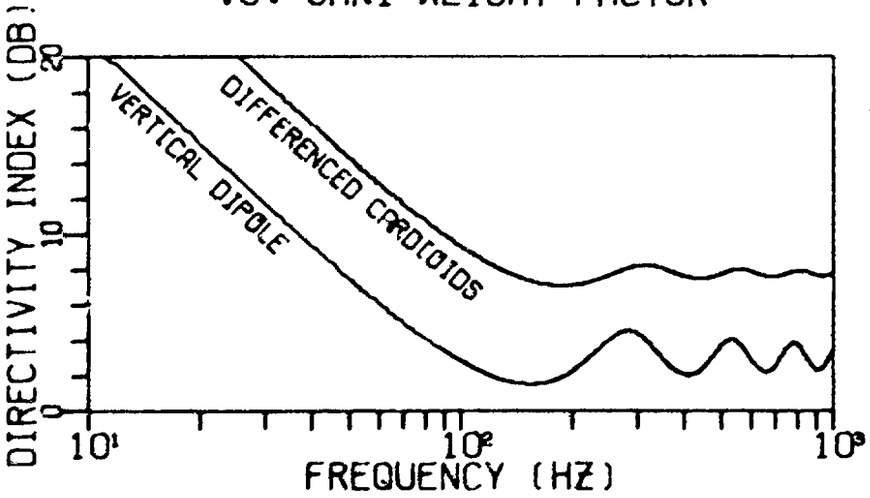

C) DIFFERENCED LIMACON DIRECTIVITY INDEX VS.FREQUENCY

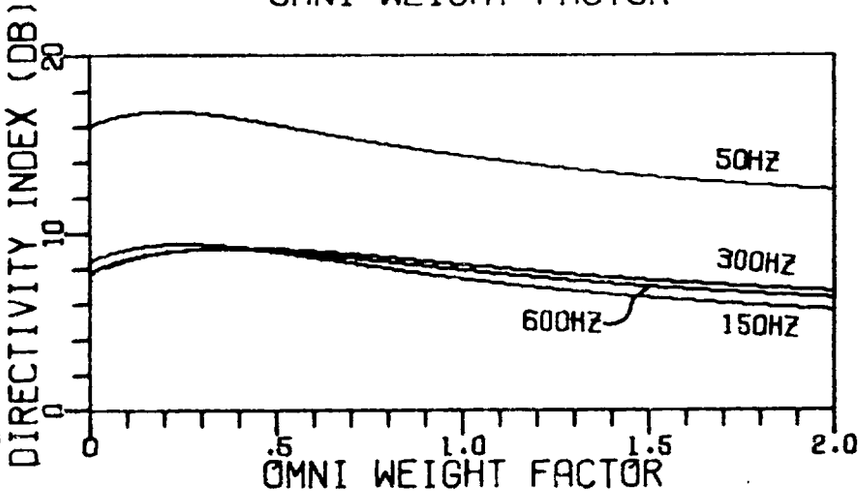

D) DIFFERENCED LIMACON DIRECTIVITY INDEX VS. OMNI WEIGHT FACTOR

FIGURE I-11
SENSOR DIRECTIVITY CHARACTERISTICS (U)

AS-79-36

(C) of the omnidirectional sensor. At very low frequencies (<10 Hz) the hydrophone spacing is only a small fraction of a wavelength; therefore the vertical dipole response to plane wave inputs should be very small (<-18 dB//omni).

(C) The directivity index of the differenced limacons is (Ref. 6)

$$DI(f,\alpha) = 10 \log \left\{ \frac{4(1+\alpha)^2}{(2\alpha^2+1)\left(1 - \frac{\sin 2a}{2a}\right) - \frac{1}{3} + \left(\frac{2a-1}{4a^3}\right)\sin 2a + \frac{\cos 2a}{2a^2}} \right\} ,$$

where $a=\pi fd/c_o \sim 0.0126f$. This result has been plotted as a function of frequency (Fig. I-11(c)) and omni weight factor (Fig. I-11(d)). The above comments on the frequency dependence of the vertical dipole also apply to the differenced limacons.

(C) The actual array gains of the single DIFAR, vertical dipole, and differenced DIFAR arrays is a function not only of the directional properties of the signal and ambient sound fields, but also of the interchannel phase and amplitude balance, and the self-noise of the array. A discussion of the DIFAR array gain degradation due to these effects is found in Ref. 7.

(S) Following signal detection, one of the next operations to be performed for each DIFAR sensor is bearing estimation. As stated earlier, the current MSS approach is to compose each DIFAR sensor of four orthogonal limacons. Consider now a plane wave of frequency f incident to the single DIFAR array at a horizontal angle θ east of north and a vertical angle γ above horizontal. In the absence of noise, the four beamformer outputs will be

(S)
$$\sigma(f,0°) = (\alpha+\cos\gamma\cos\theta)^2/(1+\alpha)^2 \quad \text{North} \quad ,$$
$$\sigma(f,90°) = (\alpha+\cos\gamma\sin\theta)^2/(1+\alpha)^2 \quad \text{East} \quad ,$$
$$\sigma(f,180°) = (\alpha-\cos\gamma\cos\theta)^2/(1+\alpha)^2 \quad \text{South, and}$$
$$\sigma(f,270°) = (\alpha-\cos\gamma\sin\theta)^2/(1+\alpha)^2 \quad \text{West} \quad .$$

The current bearing estimator is (Ref. 1)

$$B = \tan^{-1}\left[\frac{\sigma(f,90°) - \sigma(f,270°)}{\sigma(f,0°) - \sigma(f,180°)}\right]$$
$$= \tan^{-1}\left[\frac{2\cos\gamma\sin\theta}{2\cos\gamma\cos\theta}\right]$$
$$= \theta \quad .$$

Real signals, however, are seldom encountered without any noise. To minimize the effect of noise on the estimated bearing, an estimate of the background noise level on each beam is subtracted from the beamformer outputs prior to bearing estimation

$$\sigma_S(f,\phi) \sim \sigma_{S+N}(f,\phi) - \overline{\sigma_N(f,\phi)} \quad ,$$

where the bar indicates an estimated quantity. This is sometimes termed acoustic debiasing. The same bearing estimator can be shown to apply to the differenced limacon sensors.

(C) As stated earlier, the DIFAR cross-spectral beamformer can discriminate between two signal arrivals in the same frequency cell. A maximum entropy bearing estimation technique for DIFAR data has been developed (Ref. 5) which estimates two bearings directly from the cross-spectral matrix. This technique could be investigated for application to MSS. Another technique has been developed by Pryor (Ref. 8), where a generalized limacon is used to automatically null out the effects of broadband directional noise. When the omnidirectional channel is

(C) replaced with this generalized limacon, the bearings re automatically debiased and detection performance improved. This technique may also merit further investigation.

(U) The principal characteristics of each of the sensors included in this study are given in Table I-1.

(C) In the process of documenting this study, it became apparent that a sensor with a response similar to that of the vertical dipole could be formed from a single DIFAR array. Consider a beam formed from the power on each of the three DIFAR channels by

$$X_v^2(f) = X_o^2(f) - X_c^2(f) - X_s^2(f) \quad .$$

Substituting the response of each of the DIFAR channels yields

$$X_v^2(f) = 1 - \cos^2\theta \cos^2\gamma - \sin^2\theta \cos^2\gamma$$

$$= 1 - \cos^2\gamma$$

$$= \sin^2\gamma \quad .$$

Thus the response of this sensor is

$$b_v(\gamma) = \sin|\gamma| \quad ,$$

where γ is the vertical angle above horizontal.

(C) This sensor has several advantages over the vertical dipole: Because only power terms are used, it is insensitive to phase imbalance between DIFAR channels; it has the same response at all frequencies; and it does not rely on the coherence of the acoustic field across a 6.1 m (20 ft)

(C)

TABLE I-1

SENSOR CHARACTERISTICS (U)

Sensor	Description	Bearing Available	Frequency Range (Hz)	Directivity Index (dB)
Omnidirectional (O)	Omnidirectional channel from lower DIFAR array (B)	No	10 to 600	0
Single Cardioids (SC)	4-orthogonal cardioids (α=1.00) from lower DIFAR array	Yes	10 to 600	4.77
Maximum Gain Limacons (MGL)	4-orthogonal limacons (α=0.33) from lower DIFAR array	Yes	10 to 600	6.02
Vertical Dipole (VD)	Differenced omnidirectional channel (B-A) providing a horizontal null at all frequencies	No	10 to 250	7.52 at 50 Hz 1.54 at 150 Hz 4.36 at 300 Hz
Differenced Cardioids (DC)	4-orthogonal differenced (B-A) cardioids (α=1.00) providing a horizontal null at all frequencies	Yes	10 to 250	14.34 at 50 Hz 7.43 at 150 Hz 8.21 at 300 Hz

(C) aperture. The DI of this sensor is the same as that of a gradient channel (4.77 dB). Because of time constraints, this sensor was not included in this study, but does appear to merit further investigation.

(The reverse of this page is blank.)

III. DATA COLLECTION AND PREPROCESSING

(C) Data collection was accomplished via three specially modified ACODAC (Acoustic Data Capsule) systems. Each ACODAC system consisted of an instrumentation pressure vessel (IPV) containing a 7-channel tape recorder and associated signal conditioning, timing, and control circuits (Ref. 9). Prior to the FVT exercise, extensive modifications were made to these systems (Ref. 10). The resultant array configuration is shown in Fig. I-12. DIFAR arrays were located 18.3 m (60 ft) and 24.4 m (80 ft) above the ocean floor. The electronics were contained within the sensor housings, junction boxes, and IPV (Fig. I-13). The directional channels of each DIFAR array were independently compass corrected to magnetic north. Each of the six alog data channels was summed with an amplitude modulated reference tone. The seventh channel contained IRIG C timecode which encoded the day, hour, minute, system ID, and AGC settings. The data collection characteristics are summarized in Table I-2.

(C) The two pressure gradient channels of each DIFAR array were each obtained from the difference of two geophones. Since these are velocity sensors, they will be even more sensitive to flow noise than hydrophones.

(C) Because of the very low ACODAC tape speeds (normally 15/160 ips), significant crosschannel alignment errors are incurred during recording, duplication, and reproduction of these tapes. Since the FVT ACODAC data were primarily intended for DIFAR processing, special procedures were required to improve crosschannel alignment. The calibration accuracy required to achieve acceptable DIFAR performance (Ref. 10) is summarized in Table I-3. Achieving this accuracy from the ACODAC recordings required a special playback facility. This playback facility used the reference signal on each data channel to align the three channels of each DIFAR set. This procedure has frequently been termed D^3 (dewow, deskew, and deflutter). The aligned outputs of this facility were re-recorded in

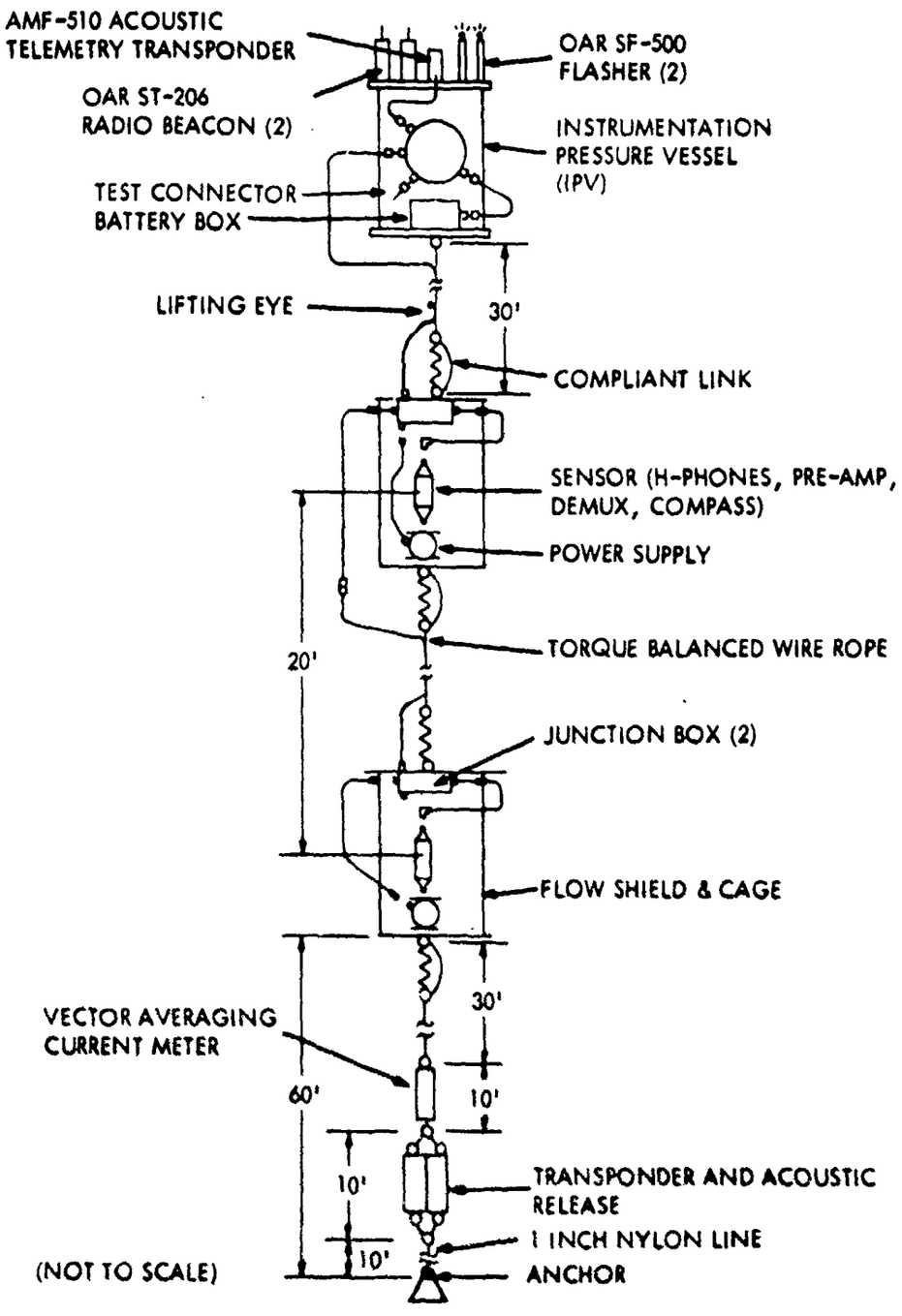

FIGURE I-12

ACODAC/MSS ARRAY CONFIGURATION (U)

AS-79-37

From ACODAC Systems Final Engineering Report, SAN-EOP-76-1127, Sanders Associates, Inc.

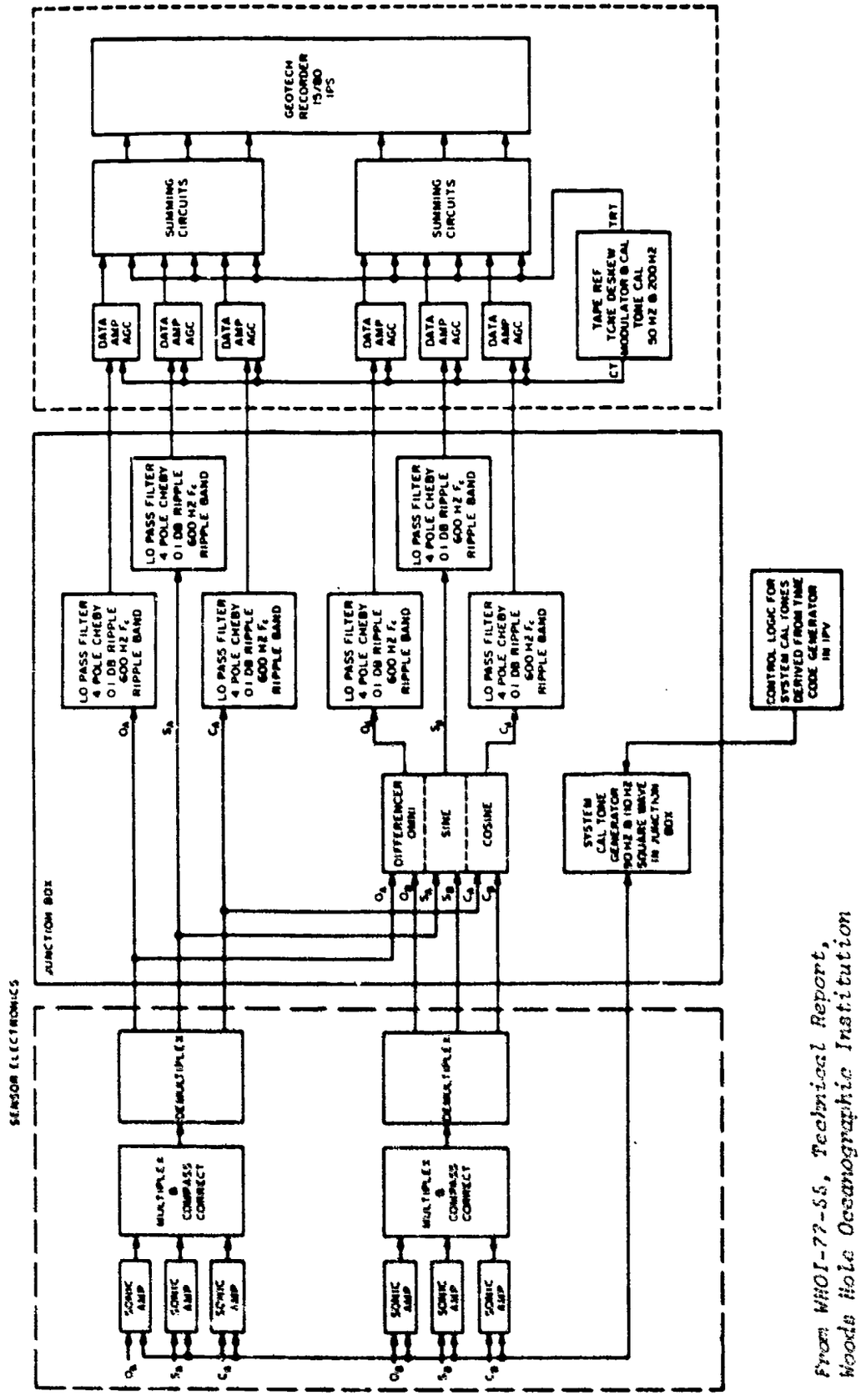

FIGURE I-13

DATA FLOW OF THE MSS-FVT ACODAC FROM HYDROPHONE THROUGH TAPE RECORDER

From WHOI-77-55, Technical Report, Woods Hole Oceanographic Institution

AS-79-38

(C)

TABLE I-2

DATA COLLECTION SYSTEM CHARACTERISTICS (U)

DATA BAND:	10 to 600 Hz
DYNAMIC RANGE:	60 dB (Recorder 27 dB, AGC 30 dB)
RECORDER SPEED:	15/80 ips
RECORDING MODE:	Analog Direct
RECORDING DURATION:	6.5 days (maximum)
AGC:	5 to 35 dB in 10 dB step with 3 dB hysteresis and gain of directionals slaved to omnis
ARRAY GEOMETRY:	Lower DIFAR (B) 18.3 m (60 ft) above bottom Upper DIFAR (A) 24.4 m (80 ft) above bottom Pressure Vessel (IPV) 36.6 m (120 f) above bottom
NUMBER OF CHANNELS:	7 (1/2 in. tape)
CHANNEL ASSIGNMENTS:	1 B cos (North/South) 2 B-A sin (East/West) 3 B omni 4 B-A omni 5 B sin 6 B-A cos 7 IRIG C time code including AGC settings (only AGC settings for channels 3 and 4 are meaningful)
REFERENCE SIGNAL:	1250 Hz sine wave with 125 Hz amplitude modulation recorded in parallel on all data channels (1 through 6)

(C)

TABLE I-3

SENSOR CALIBRATION ACCURACY REQUIREMENTS (U)

SINGLE DIFAR ARRAY -

sin to cos Tracking:	15° phase ±1 dB
sin to omni Tracking:	20° phase ±3 dB
Compass Trim:	5° p-p phase ±1 dB
Frequency Range:	20 to 600 Hz

DIFFERENCED DIFAR ARRAY -

omni to omni Tracking:	15° phase ±0.75 dB
cos to cos Tracking:	7.5° phase ±0.5 dB
sin to sin Tracking:	7.5° phase ±0.5 dB
Tilt:	≃3° maximum

(C) FM mode at a much higher tape speed. Recordings of this type are relatively immune from phase and amplitude errors. As many as 20 FM tapes were produced from each ACODAC tape.

(C) After a single set of aligned tapes was produced, the tapes were duplicated and shipped to the various data processors, including ARL:UT. The duplication of FM tapes is usually a simple procedure. The duplication station is usually configured to perform a unity-gain DIRECT-TO-DIRECT mode copy. Since the FM signal is not decoded, no additional errors are incurred. Unfortunately, the duplication station used for these data did not have the required DIRECT mode capacity; therefore, FM-to-FM copies were made. The resultant copies were of poor quality. Small portions of the data were completely destroyed due to overdeviation of the FM carrier. Large amplitude imbalances (6 to 8 dB) were incurred, even between two copies of the same tape. Consequently, the duplication procedure may have significantly increased the amplitude error of these results, which would, in turn, have increased bearing error.

IV. A/D CONVERSION AND DATA REDUCTION

(U) The first major component of the ARL:UT measurement system (Fig. I-2) is termed A/D conversion and data reduction. This component accepts single and/or multichannel inputs in analog format and converts them to time-averaged calibrated autospectra and cross-spectra. These spectra serve as the primary input to both of the remaining measurement system components. For this application, the required steps are shown in Fig. I-14.

(S) Selected portions of the FVT ACODAC data set were processed with two frequency resolutions. The low resolution data were intended to emulate MSS standard resolution (0.2 Hz) data. The high resolution data were intended to emulate MSS vernier resolution (0.0125 Hz) data.

(C) The selected data were first converted from an analog to a digital representation and stored as an intermediate data product on magnetic tape. The available timecode and calibration information were simultaneously extracted. The analog data were reproduced on an Ampex instrumentation tape recorder with intermediate band electronics. Three channels, a DIFAR set, were digitized on each pass through the data set. The analog hardware configuration was dependent on whether standard frequency resolution (Fig. I-15) or vernier frequency resolution (Fig. I-16) was desired. The analog signals were bandpass filtered to prevent aliasing and input to programmable amplifiers under joint computer/operator control. The amplifier gain was automatically varied at 1 min intervals to obtain maximum utilization of the dynamic range of a 12-bit A/D converter. The gains of the gradient channels were slaved to the gain of the omnidirectional channel, except for constant offsets which were frequently required to bring the channels into approximate balance. The A/D converter was preceded by three simultaneous sample and hold (SS+H) circuits, one per channel. Vernier resolution data were also frequency translated prior to the SS+H circuits. The frequency translator consisted

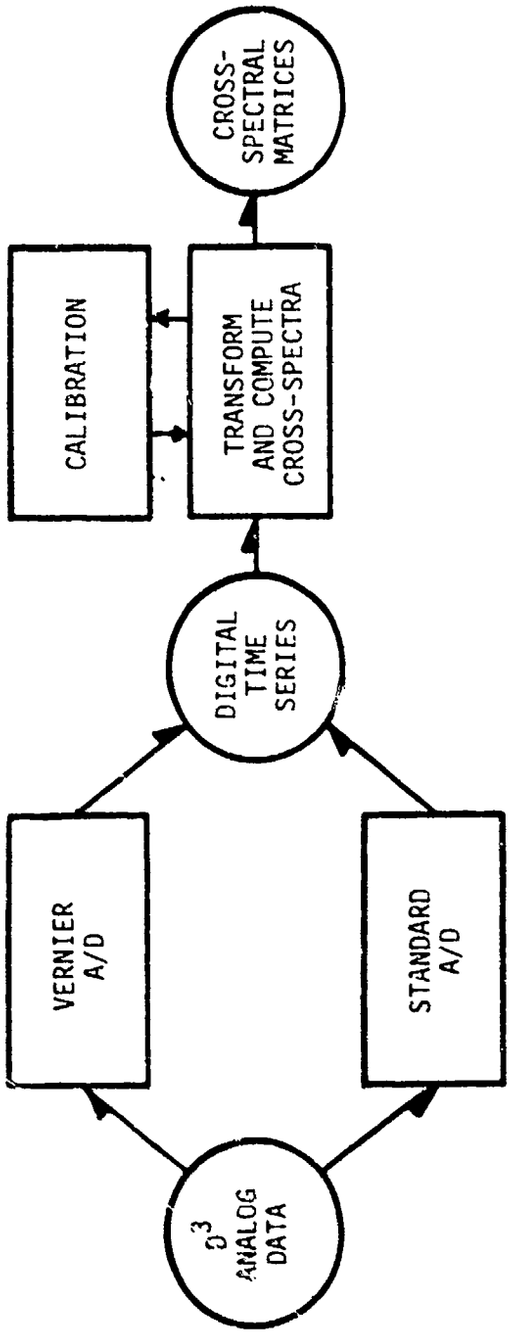

FIGURE I-14
A/D CONVERSION AND DATA REDUCTION OVERVIEW

AS-79-39

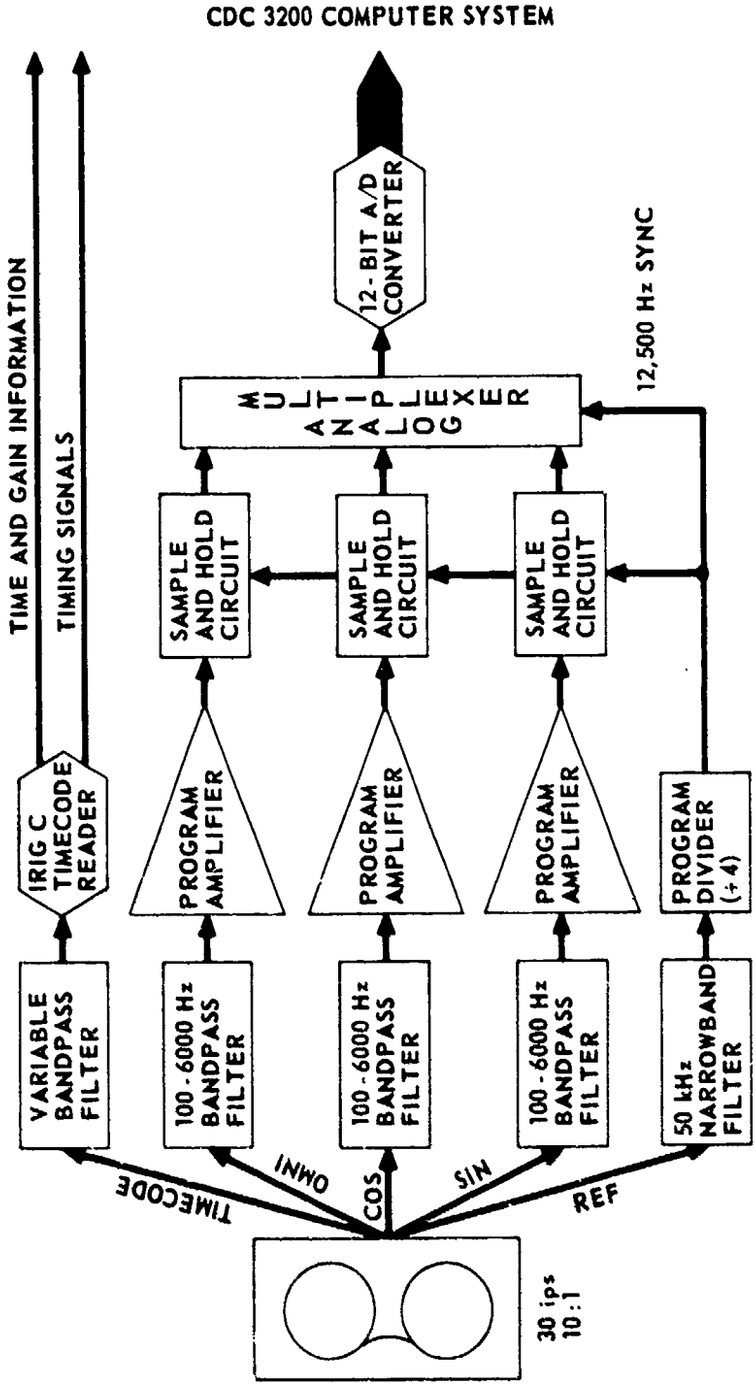

FIGURE I-15
STANDARD RESOLUTION A/D HARDWARE CONFIGURATION

ARL:UT
AS-78-530
SLW-GA
3-22-78

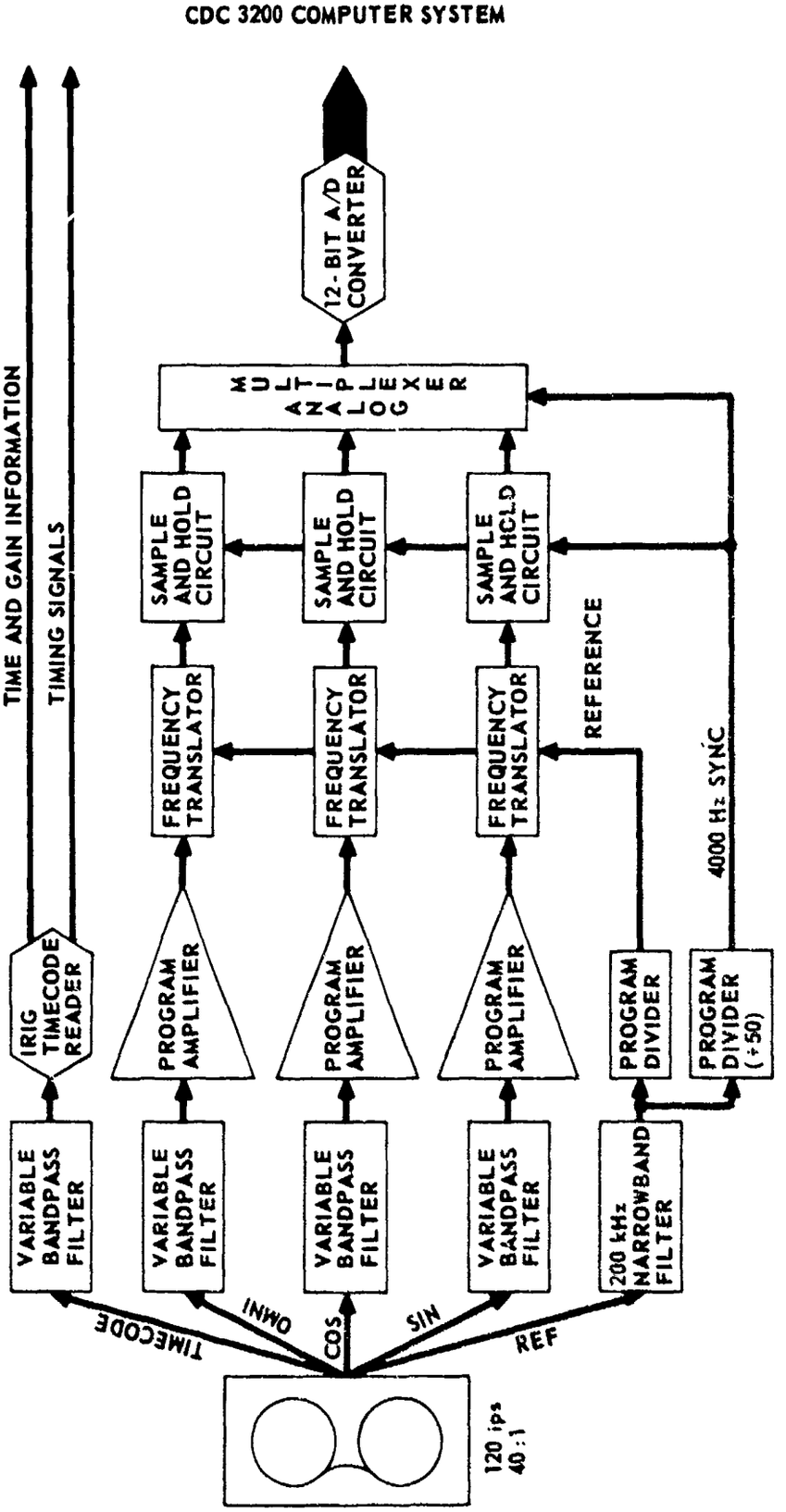

FIGURE I-16
VERNIER RESOLUTION A/D HARDWARE CONFIGURATION

ARL:UT
AS-78-531
SLW-GA
3-22-78

(C) of three custom made double-balance mixers and low pass filters (Ref. 11). The gain of these low pass filters was adjusted so that the linear input range of the mixer corresponded to the range of the A/D converter. The reference for these mixers was derived from the timebase reference signal recorded on each analog tape. The SS+H circuits and A/D converter were also triggered at a rate derived from this reference.

(U) The digitized data were then input to a Control Data 3200 computer system (Fig. I-17). This computer was used to select amplifier settings and to ensure that the data did not exceed the ±10 V range of the A/D converter. The operator had the option of permitting such "clipping," and usually did when high level transient signals were present. Such "clipped" data were automatically tagged and then deleted during data reduction. The digital data were stored on magnetic tape in a format designed to facilitate later processing, along with time, gain, and quality indicators. The computer performed error detection which included timecode monitoring and verification, signal amplitude monitoring, data flow monitoring, and overall synchronization. If synchronization was lost, the process was terminated, and the operator was informed of its cause. After the appropriate corrective action was performed, the process was reinitiated prior to the point where synchronization had been lost. The computer also generated a permanent log of each interruption and the operator's reaction.

(U) The data were digitized in a sequence of four A/D runs, one for each of the three vernier resolution frequency bands and one for the standard resolution frequency band. The playback tape recorder was first equalized so that the header calibration sequences had a flat response across the frequency band of interest. The three analog data channels, from tape recorder output to SS+H circuit output, were then balanced to within 0.1 dB and ±3°. The desired data from each site were then digitized. The external calibration sequence (header cals) for these data were digitized immediately before and after the data digitization. This

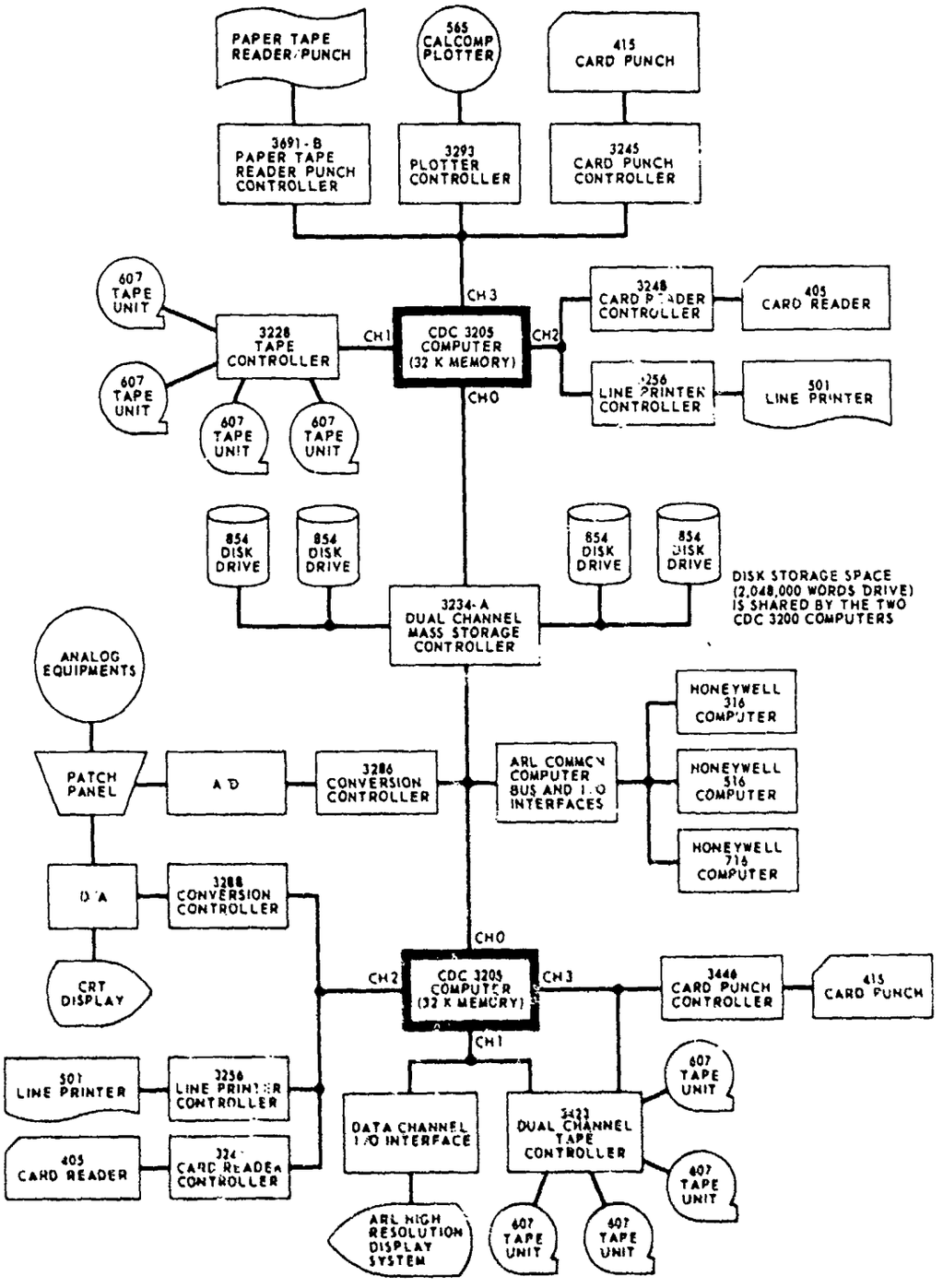

FIGURE I-17
DUAL CDC 3200 COMPUTER SYSTEM

ARL-UT
RS-74-1232
MMD-DR
11-11-74
REV 2-2-76

(U) redundance was used to verify the stability and repeatability of the playback system. Amplitude differences were typically less than 0.1 dB. Interchannel phase differences also remained nearly constant (Appendix I-A). The amplitude transfer functions (T) of the entire record-D^3-duplicate-playback-A/D system were obtained from the measured levels of the calibration signals (M) and their absolute levels (A)

$$T(f) = \frac{A(f)}{M(f)} \quad ,$$

where f is frequency in hertz. The composite transfer function (C) used to calibrate the data to sound pressure level (SPL) in the water was

$$C(f) = \frac{T(f)}{R(f)} \quad ,$$

where R(f) is the amplitude transfer function from the water to the tape recorder, exclusive of AGC. A(f) was furnished by Woods Hole Oceanographic Institution, and R(f) is tabulated in Ref. 10.

(C) The tabulated values of R(f) apply only to single DIFAR arrays and neglect the effect of the differencing network (Fig. I-13). The calibration of the differenced DIFAR data (B-A) was accomplished by using the linear summation of the corresponding values of R(f). The composite calibration factors were therefore computed by

$$C_B(f) = \frac{T_B(f)}{R_B(f)}$$

$$= \frac{A(f)}{[M_B(f)\ R_B(f)]} \quad , \text{ and}$$

(C)
$$C_{B-A}(f) = \frac{T_{B-A}(f)}{[R_A(f)+R_B(f)]}$$

$$= \frac{A(f)}{\left\{M_{B-A}(f)\ [R_A(f)+R_B(f)]\right\}} \quad .$$

As was discussed in section II, at frequencies of less than 125 Hz the response of the differenced DIFAR array channels will always be less than $R_A(f)+R_B(f)$ because the arrays are less than a half-wavelength apart.

(U) Transfer functions for the standard frequency resolution data were computed by log-log interpolation on T and R. The number of calibration signals within each vernier frequency band was inadequate to define its response. Therefore, immediately prior to and following the digitization, the tape recorder was replaced by a white noise generator, and the ARL:UT A/D system response was measured. These curves were then used to interpolate between calibration signals.

(C) The final data reduction step accepts as input the digital time-series data and composite transfer functions, and then computes the outputs time-averaged calibrated cross-spectra. All of the computations of the cross-spectral matrix beamformer (Fig. I-8) through ALI are performed. In addition, computations are performed to edit and normalize the input data and to calibrate the results. The FFT length (8192 samples) was chosen in conjunction with the sample rates to yield the desired frequency range and resolution. The spectral window (Hanning) and overlap (50%) were chosen for their variance reduction properties (Refs. 12 and 13) and low spectral bias (Ref. 14). The ALI type was rectangular integration, where all of the spectra computed during the ALI interval are averaged across each frequency cell. The spectra output for each ALI interval are characterized by the number of equivalent degrees of freedom. These parameters are summarized in Table I-4.

(S) TABLE I-4

A/D CONVERSION AND DATA REDUCTION PARAMETERS (U)

PARAMETER	STANDARD RESOLUTION	VERNIER RESOLUTION
Sample Rate	1250 Hz	100 Hz
Frequency Range	10 to 600 Hz	46 to 84 Hz (low band) 145 to 183 Hz (mid band) 300 to 338 Hz (high band)
FFT Length	6.55 sec	81.92 sec
Spectral Window	Hanning	Hanning
Frequency Spacing	0.1526 Hz	0.0122 Hz
3 dB Bandwidth	0.2197 Hz	0.0176 Hz
Equivalent Noise Bandwidth	0.2289 Hz	0.0183 Hz
FFT Overlap	50%	50%
ALI Interval	1 min	5 min
ALI Type	Rectangular Integration	Rectangular Integration
FFT/ALI (maximum)	18	7
Time Bandwidth Product (maximum)	13.67	5.76
Number of Equivalent Degrees of Freedom (maximum)	32.3	13.4

(U) The number of equivalent degrees of freedom of each spectra is a measure of statistical stability. It has been shown (Ref. 15) that overlapped FFT processing of windowed Gaussian data results in spectral estimates whose distribution is very closely approximated by a chi-square distribution with the appropriate number of equivalent degrees of freedom. Once this distribution is known, it can be used to set detection thresholds and to test data for inhomogeneity. The number of equivalent degrees of freedom for n transforms with 50% overlap and Hanning is approximately (Ref. 15)

$$EDF(n) = \frac{36\ n}{19 - 1/n} \quad .$$

The value of n may vary between spectra because of the editing criteria applied to the input.

V. AMBIENT SOUND FIELD MEASUREMENT TECHNIQUE

(U) The second major component of the ARL:UT measurement system (Fig. I-2) is that which accepts spectra as input, and computes and displays measurements of the ambient sound field (ASF). The goal is to obtain measurements as a function of frequency and time of the ASF levels observed by the omnidirectional sensor and of the noise gains of the directional sensors relative to the omnidirectional sensor. Clutter measurements are also a property of the ASF; however, since such measurements require a cw processor, discussion of them will be deferred to the section on cw processing. Noise gain is herein defined as

$$NG = 10 \log \frac{\text{ASF level observed via directional sensor}}{\text{ASF level observed via omnidirectional sensor}} ,$$

where both levels are determined over the same time interval and frequency band. If the ASF was isotropic, noise gain would be equal to the negative of the directivity indices computed in section II:

$$NG_{\text{isotropic}} = -DI .$$

(U) The ASF measurements were formed over fixed frequency bands. For the vernier resolution data, each band was 1 Hz wide and centered at each integer frequency within the band. For the standard resolution data each band was 1/10-octave wide (W=0.1). The center frequency (f_c), lower limit (f_L), and upper limit (f_u) for each band are obtained from

(U)
$$K = 2^{W/2}$$

$$f_c(i) = 10^{0.3Wi}$$

$$f_L(i) = f_c(i)/K$$

$$f_u(i) = f_c(i) \times K \quad ,$$

where i is the standard band number, and ranged from 43 (f_c = 19.5 Hz) to 92 (f_c = 575 Hz).

(C) Techniques for extracting a representative cross-spectral matrix from a frequency band of such matrices are not well established. If such techniques were available, then the resulting matrix could be used to characterize horizontal directivity and optimum beamforming (Ref. 2). For this study, the elements of each cross-spectral matrix were summed across the desired frequency band; the resulting sums were then normalized to a 1 Hz bandwidth. The resulting matrices from both the single and differenced DIFAR arrays were then merged (Fig. I-18) into a single ASF data base. This data base was then acted upon with the cross-spectral limacon beamformer (Fig. I-8) to yield beam levels and noise gains as a function of frequency, time, site, sensor, direction, and omni weight factor. A description of the three display formats can be found in Volumes II and III.

(U) The expected distribution about the mean value for the ASF measurements through 1/10-octave bands for stationary Gaussian input data is shown in Fig. I-19. These results are derived in Appendix I-B and are based on Ref. 16. Whenever the measured distribution exceeds those of Fig. I-19, this implies that the input data were nonstationary or non-Gaussian (cw signals). The vertical line on Fig. I-19 denotes the expected spread of the vernier resolution measurements.

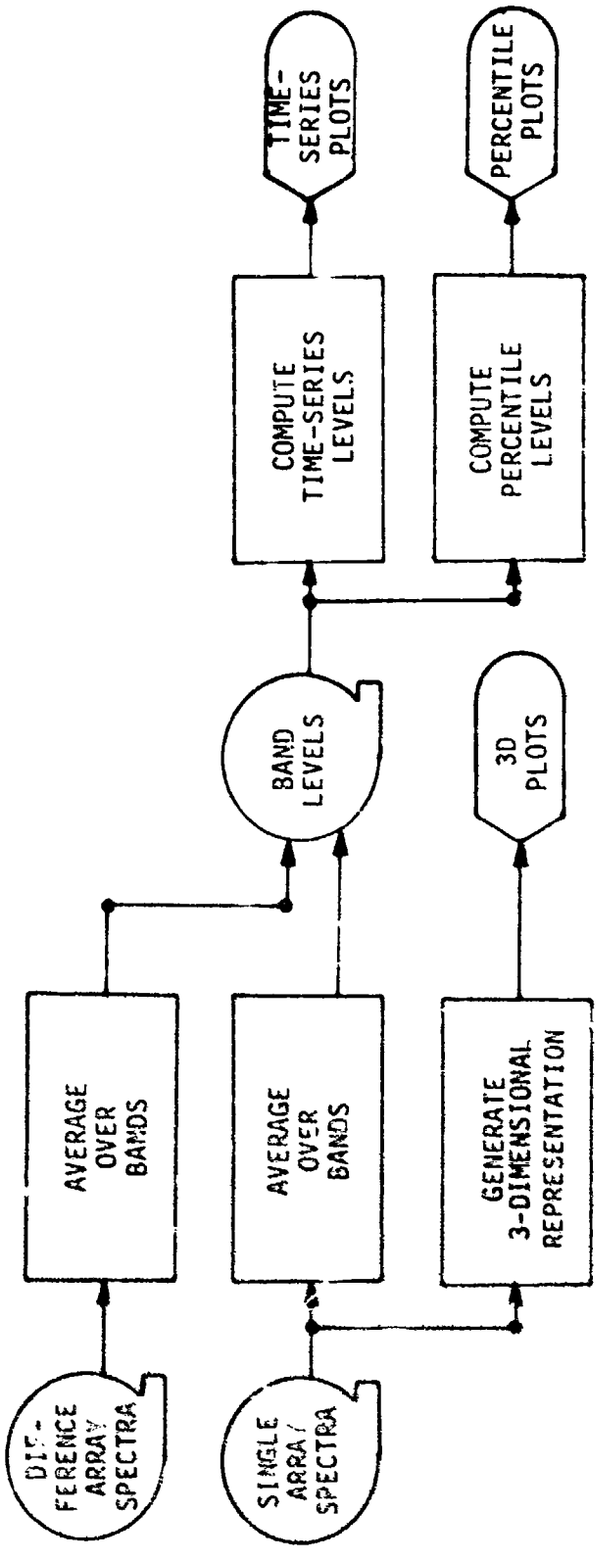

FIGURE I-18
ASF PROCESSOR OVERVIEW

AS-79-40

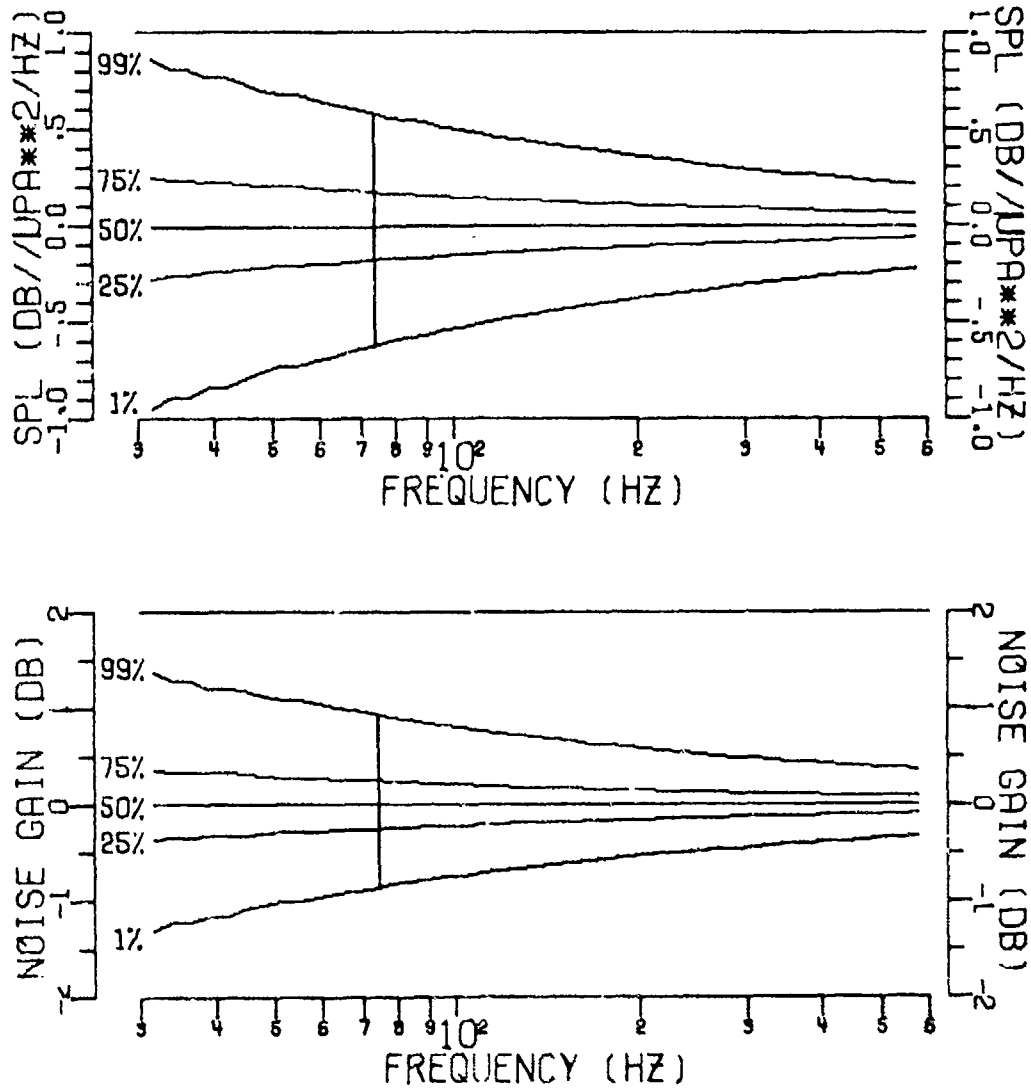

FIGURE I-19
EXPECTED DISTRIBUTION OF AMBIENT SOUND FIELD MEASUREMENTS THROUGH 1/10-OCTAVE BANDS

AS-79-41

(U) An additional test was applied to these data to ensure that the measurements were not contaminated by the electronic noise floor of the record-D^3-duplicate-playback-A/D system. The level of the electronic noise floor (E) was approximated from the measured levels during the first minute of an internal calibration signal (6 h cal). During this minute an open circuit was input to the ACODAC data amplifiers. This electronic noise is always present and biases the resultant measurements (R) above the actual levels (A).

$$R = A + E \quad .$$

If biases of less than 1 dB only are to be tolerated,

$$10 \log(R/A) \leq 1 \quad ,$$

then the acceptable measurement-to-noise floor ratio is

$$10 \log(R/E) \leq -10 \log(1-10^{-0.1}) = 6.87 \text{ dB} \quad .$$

For these data, any measurements within 6 dB of the measured electronic noise floor levels were deleted. This resulted in the elimination of all of the data below 30 Hz.

(U) The ASF processing parameters are summarized in Table 1-5.

(C) TABLE I-5

AMBIENT SOUND FIELD PROCESSOR PARAMETERS (U)

Parameter	Standard Resolution	Vernier Resolution
ALI Interval	1 min	5 min
Bandwidth	0.1 octave	1 Hz
Band Formation Technique	Rectangular Integration	Rectangular Integration
Noise Floor Contamination Criteria	6 dB	6 dB

VI. cw MEASUREMENT TECHNIQUE

(U) The third major component of the ARL:UT measurement system (Fig. I-2) accepts spectra as input, and computes and displays measurements based on received cw signals. All cw signal processors include the functions of signal identification and parameter estimation. The selection of an identification technique is based on the amount of information known about the signal. The parameter estimation technique is selected to provide the desired measurements. Different processing techniques, when applied to the same data, can yield significantly different results.

(C) In an earlier ARL:UT FVT study (Ref. 17), the goal of the cw processor was to obtain cw propagation loss measurements. It was assumed that the frequency and nominal Doppler shift were known a priori for the single projector line of interest. The identification technique was a peak search over a restricted frequency range, and explicit line tracking from one ALI interval to the next was not required. The propagation loss parameter was computed from the cw SPL, which was estimated by summing the received SPL over the band of frequency cells containing the signal and subtracting an estimate of the ASF SPL in the same band. Measurements obtained with this technique are relatively insensitive to Doppler smearing and to the distribution of signal SPL between and within each cell. The error of such measurements is further decreased relative to those based on single cells, because the ASF was summed across multiple cells, thus decreasing the expected error of a mean estimate. Finally, the measurements based on total received signal SPL correspond to those predicted by most propagation models.

(C) In this study, the goal was to obtain performance measurements for candidate MSS sensors coupled to a surveillance processor. This processor had no a priori information on the number of sources, their frequencies, or their locations. It was required to detect and track all of the lines

(C) within the processor frequency band. The desired performance measurements included detection and bearing estimation against simulated target lines, array gain of candidate sensors, and clutter related (processor loading) statistics. The processor was also required to output sufficient ancillary data to permit an interpretation of the performance measurements.

(C) These cw measurements were provided by a sequence of three processors (Fig. I-20). The single cell processor determined which of the frequency cells contained signals, and estimated their parameters. The line related processor formed the detected cells into lines, estimated line parameters, and tracked the lines through time. The editing and display processors were used to identify projector lines and exercise artifacts, and to extract and display the final cw signal and clutter measurements. Each of these processors was implemented as a separate software program and will now be described in detail.

(C) Two versions of the single cell processor were used. The first version provided only for a single beam (omnidirectional or vertical dipole) sensor without bearing estimation, while the second was a 4-beam (single or differenced DIFAR) sensor version with bearing (Fig. I-21). Only the multibeam version will be discussed since it contains all the features of the single beam version.

(C) The first function of the single cell processor, beamforming, was accomplished with the cross-spectral beamformer discussed in section II. The SPL values for each beam were computed in parallel (Fig. I-8) and presented to the autodetect routine in order of decreasing frequency.

(C) The mean background ASF SPL on each beam was estimated by a clipper/replacement technique (Fig. I-22). This technique synthesizes a two-pass estimator. On the first pass, a "clipped" spectrum (y) is created where the narrow high level lines have been replaced with lower levels. On the second pass, the mean background ASF SPL is estimated from

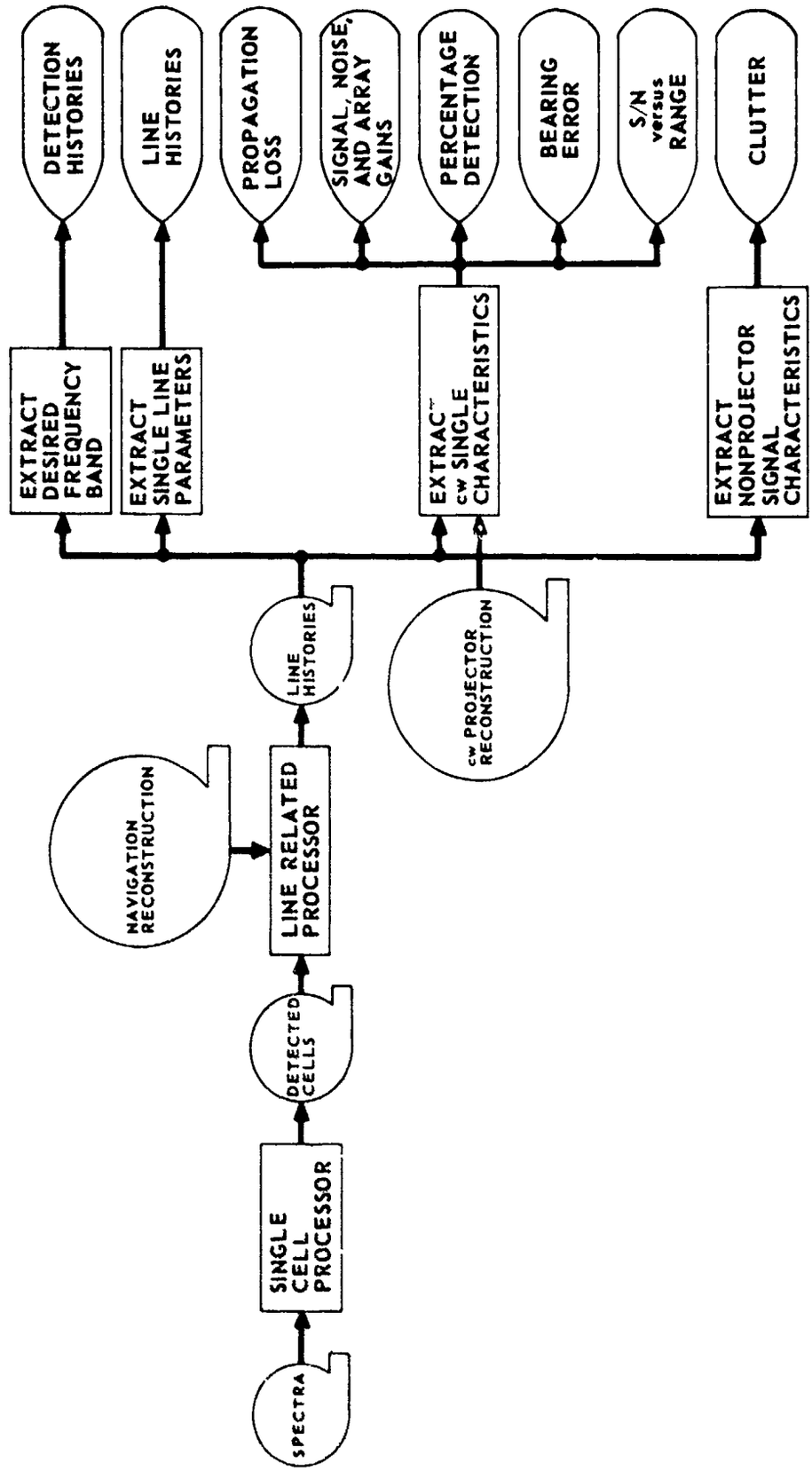

FIGURE I-20
cw PROCESSOR OVERVIEW

ARL:UT
AS-76-532
SLW-GA
3-22-78

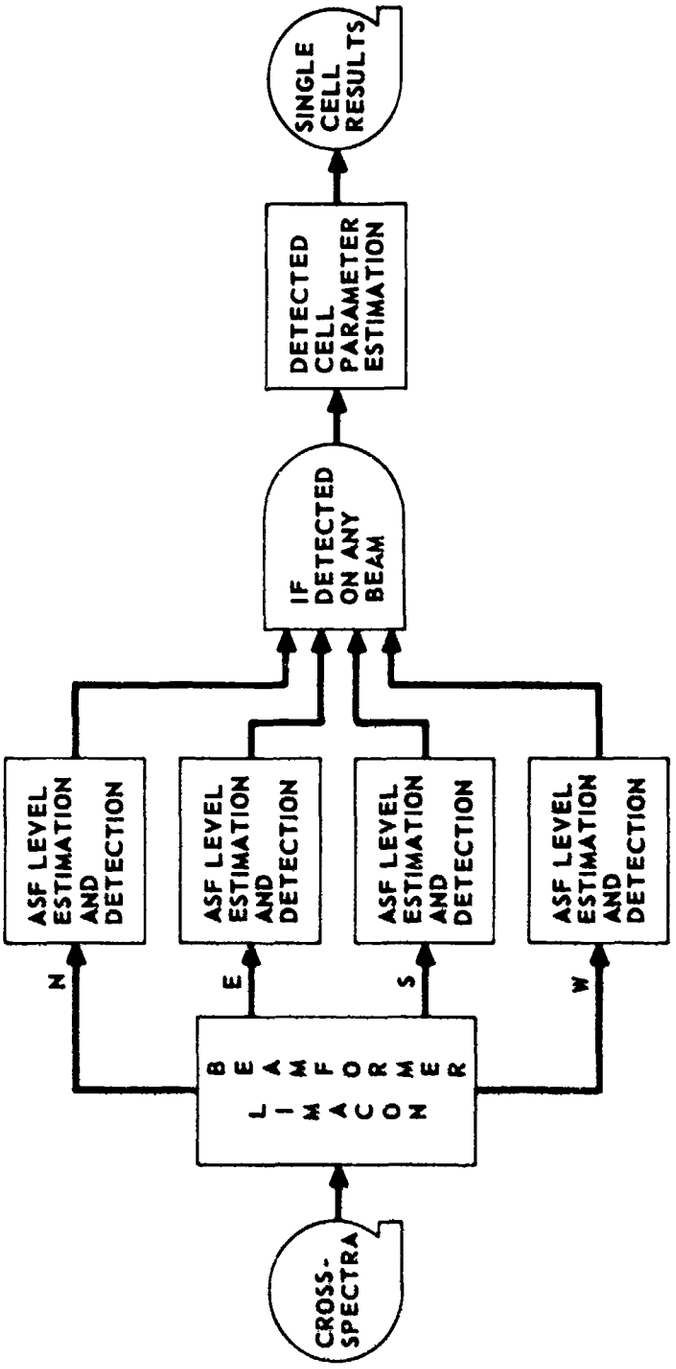

FIGURE I-21
SINGLE CELL PROCESSOR FLOW DIAGRAM (U)

ARL:UT
AS-78-650
SLW-GA
4-20-78

STANDARD FREQUENCY RESOLUTION

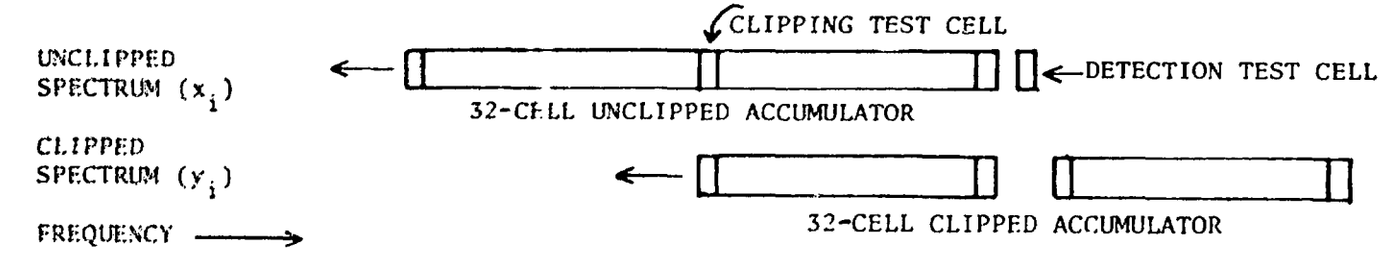

VERNIER FREQUENCY RESOLUTION

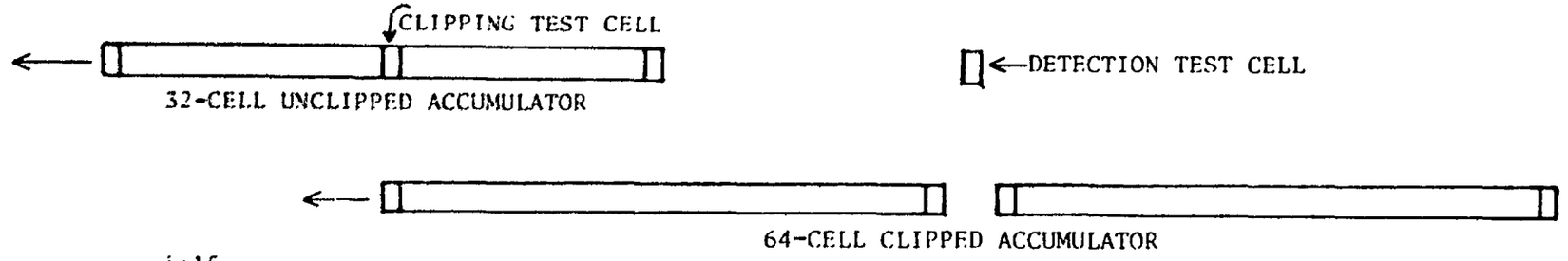

$X_i = \frac{1}{32} \sum_{i-16}^{i+15} x_j$ (unclipped accumulator), $Y_i = \frac{1}{N} \sum y_i$ (clipped accumulator)

IF $x_i > C_c \cdot X_i$, then $y_i = C_r \cdot X_i$; else $y_i = x_i$.

IF $x_i > C_d \cdot Y_i$, then "SIGNAL DETECTED"; else "NO DETECT".

AS-79-43

FIGURE I-22

BACKGROUND NOISE ESTIMATION AND SIGNAL DETECTION ALGORITHM (U)

CONFIDENTIAL

(C) the clipped spectrum. This technique was intended to reduce the ASF estimator bias caused by high level lines.

(C) During the first pass of the estimator, the unclipped spectrum (x) was first averaged over a 32-cell window centered about each test cell,

$$X_i = \frac{1}{32} \sum_{i-16}^{i+15} x_i \quad .$$

If the ratio of the test cell SPL to the average unclipped SPL exceeded a threshold, termed the clipper coefficient,

$$\frac{x_i}{X_i} > C_c \quad ,$$

then the test cell SPL was replaced by the product of the average unclipped SPL and the replacement coefficient,

$$y_i \leftarrow X_i \times C_r \quad ;$$

otherwise

$$y_i \leftarrow x_i \quad .$$

(C) During the second pass of the estimator, the background ASF estimate was obtained by averaging the clipped spectrum over a window of 32 cells for standard resolution and 64 cells for vernier resolution. Each window was centered about a 3-cell gap which contained the detection test cell.

(C) Selection of clipper and replacement coefficients requires a tradeoff in the accuracy of the estimator against high level and low level lines.

(C) By reverting once more to the chi-square approximation for FFT processing of stationary Gaussian input, the clipper and replacement coefficients can be computed as functions of ASF percentile level and the number of equivalent degrees of freedom (Fig. I-23). With a clipper probability of 0.90, 10% of the test cells would be clipped in the absence of any signals. This clipping of nonsignal cells would tend to bias the ASF estimate low (Appendix I-C). Any decrease in the clipper probability would increase this negative bias (Fig. I-24). The effect of a low ASF estimate, in the absence of signals, is to increase the false alarm rate since the detection decision is based upon the estimated ASF levels. Choosing a higher clipper probability would decrease the negative bias in the absence of signals, but would also tend to increase the positive bias of the estimator when signals are present.

(C) This estimator performs well against very narrow signals, but degrades quickly if the signal occupies more than a few cells. This degradation results in high ASF estimates in the vicinity of broad and/or very high level signals. The result of this positive bias is to prevent detection of weak signals near strong signals and to cause errors in the estimated signal parameters (Ref. 18). These biases will be larger for a square-law detector, such as was used for this study, than for a linear detector. For this study the clipper probability was 0.90, the replacement probability was 0.50, and the detection coefficient was adjusted to compensate for the expected estimator bias (Fig. I-24).

(C) The difficulty of automatically obtaining an unbiased background ASF estimate is well known. It has been shown (Ref. 18) that a median based estimate will have a much smaller bias; however, the normal computation technique of ordering the cells within the noise band is too costly for operational realtime systems. An alternative median estimation technique, which is less costly than even the clipper/replacement technique, has recently been suggested. For a reasonably flat spectrum, the suggested procedure, following initialization, is to

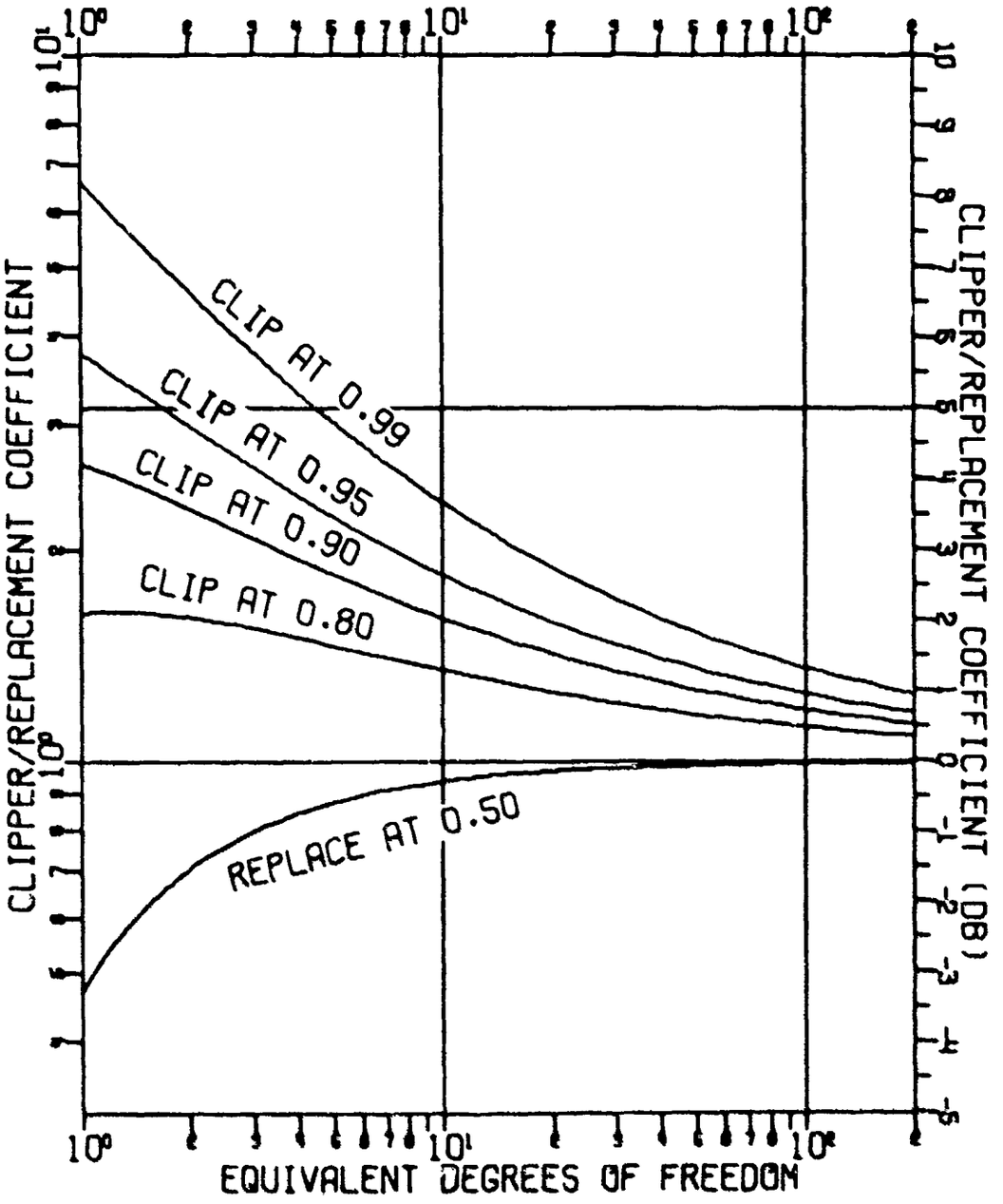

FIGURE I-23
CLIPPER AND REPLACEMENT COEFFICIENTS VS NUMBER OF DEGREES OF FREEDOM AT SELECTED PROBABILITIES (U)

AS-79-44

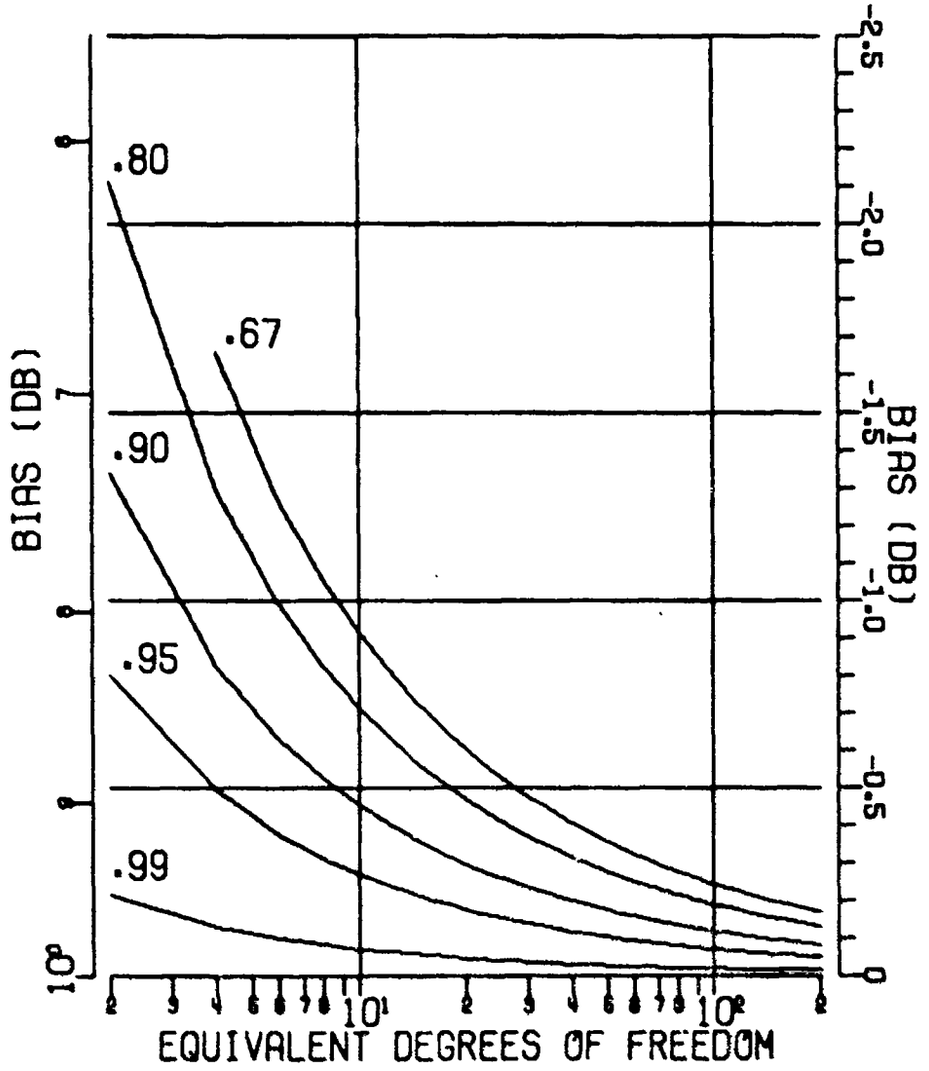

FIGURE I-24
BIAS IN ESTIMATED NOISE LEVEL DUE TO CLIPPING
OF SPECTRUM AT VARIOUS PROBABILITY LEVELS
WITH MEDIAN VALUES AS REPLACEMENTS

AS-79-45

(C) sequentially compare each cell of the unclipped spectrum (x) with the current value of the estimator (X). Depending upon the result of this comparison, the estimator is updated as follows:

$$\text{if } x_i > X_{i-1}, \text{ then } X_i = X_{i-1} + a \quad ;$$

$$\text{if } x_i = X_{i-1}, \text{ then } X_i = X_{i-1} \quad ; \text{ and}$$

$$\text{if } x_i < X_{i-1}, \text{ then } X_i = X_{i-1} - b \quad .$$

The background ASF estimate for cell i is X_i. If a=b, the median value is estimated. Other percentile levels can be estimated by adjusting the ratio of a to b. The stability and response of the estimator are controlled by the magnitudes of a and b. For nonflat spectra, the technique is modified by multiplying by a instead of adding, and by dividing by b instead of subtracting. This can be interpreted as adding and subtracting on a log scale. This technique has been used extensively at ARL:UT for applications such as LOFARGRAM prewhitening, but has not been applied in this study.

(S) Single cell detections were based on the usual Neyman-Pearson criteria, wherein the detection threshold is determined by the distribution of the noise and the desired false alarm rate. Once again the noise was assumed to follow a chi-square distribution, and the false alarm rate (P_{fa}) was set to 10^{-3}. The test cell (x_i) was said to be detected (contain a signal) if

$$\frac{x_i}{y_i} > C_d \quad ,$$

where y_i is the background ASF SPL estimate and C_d is termed the detection coefficient. The detection coefficient is related to the detection threshold (DT) by

(S) $$DT = 10 \log[1.5w(C_d-1)] \quad ,$$

where w is the frequency spacing between cells, and 1.5 is used to normalize the frequency spacing to its equivalent noise bandwidth when the spectrum has been Hanned.

(C) The value of the detection coefficient is computed as a function of the probability of false alarm (P_{fa}) and the number of equivaler degrees of freedom (ν) by (Ref. 19).

$$C_d(P_{fa},r) = \left\{1 - \frac{2}{9\nu} + Z(1-P_{fa})\sqrt{\frac{2}{9\nu}}\right\}^3 \quad ,$$

where Z(P) is a rational approximation for standard normal probabilities such as (Ref. 19). This result is shown in Fig. I-25 for selected ALI intervals.

(U) The minimum detectable signal level (MDS) was predicted by the methods of Ref. 20. These predictions are tabulated with the single cell processor parameters in Table I-6.

(S) The false alarm rate for this study was initially specified as 10^{-4}, but was later changed to 10^{-3} to provide better detections against simulated third generation targets. If the false alarm rate had been left at 10^{-4}, the standard and vernier detection thresholds and MDS would have been raised by 0.9 dB and 1.1 dB, respectively.

(C) The detection decision was made in parallel on all beams of a frequency cell. If a signal was detected on any beam, the following cell parameters were output:

cell number,
background ASF SPL estimate for each beam, and
signal SPL estimate for each beam,

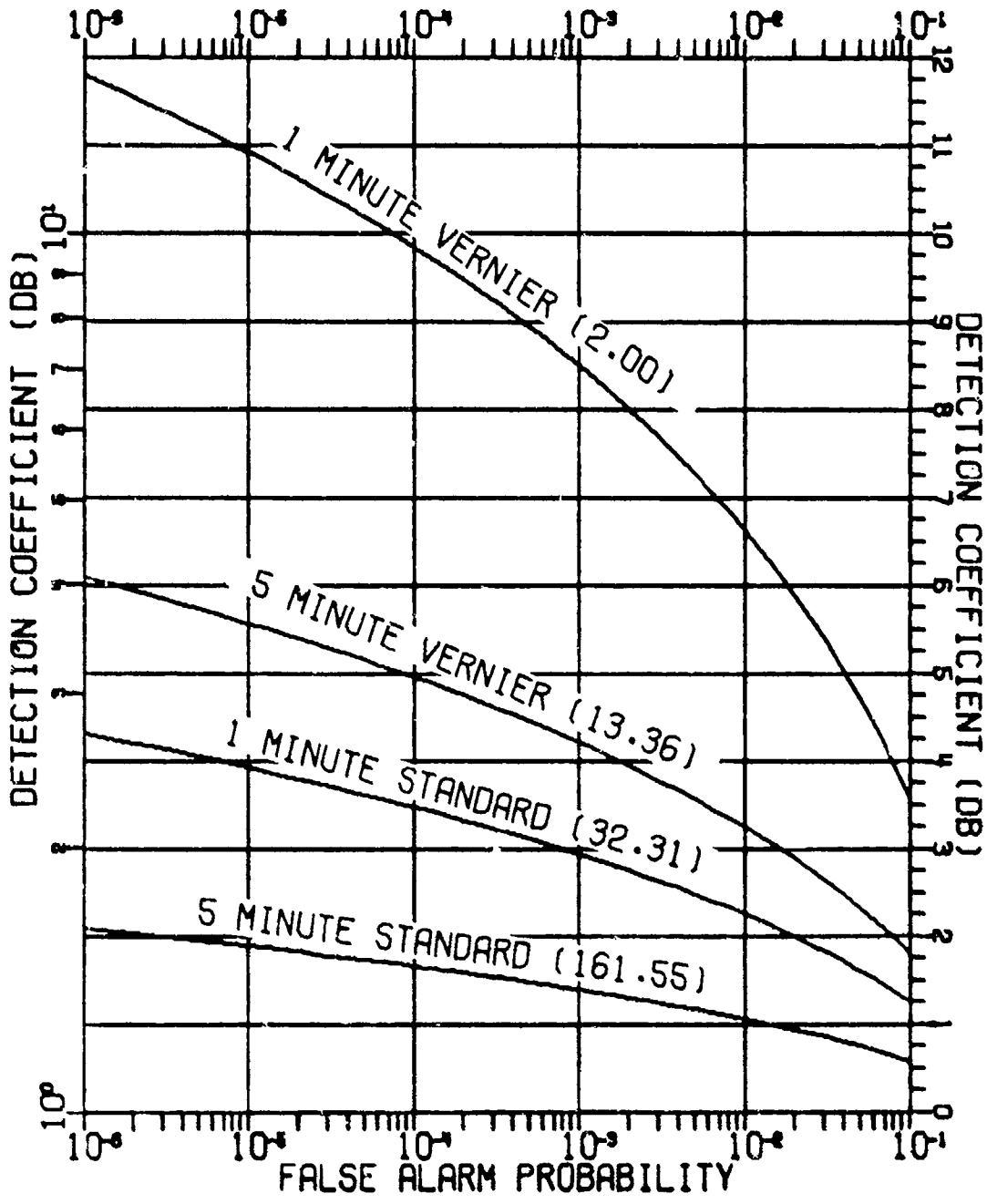

AS-77-1031

FIGURE I-25
DETECTION COEFFICIENT versus FALSE ALARM PROBABILITY
FOR VARIOUS ALI INTERVALS (DEGREES OF FREEDOM) (U)

(S) TABLE I-6

cw PROCESSOR PARAMETERS (U)

Parameter	Standard Resolution	Vernier Resolution
ALI Interval	5 min	5 min
3 dB Bandwidth	0.2197 Hz	0.0176
Number of Equivalent Degrees of Freedom (maximum)	161.6	13.4
Noise Window Width	32 cells (4.88 Hz)	64 cells (0.78 Hz)
Clipper Probability	0.90	0.90
Replacement Probability	0.50	0.50
Expected Estimator Bias	-0.1 dB	-0.4 dB
False Alarm Probability	10^{-3}	10^{-3}
Detection Threshold	-10.6 dB//Hz	-15.2 dB//Hz
Predicted MDS (P_{det} = 50%)	-10.3 dB (1 Hz)	-14.8 dB (1 Hz)

(C) where the signal SPL was estimated as the unclipped SPL of the test cell minus the background ASF SPL estimate on the same beam. These results were stored on tape for input to the line related processor.

(C) First, the line related processor (Fig. I-26) sequentially inputs the detected cell parameters. Based on these parameters, the detected cells for each ALI interval were then formed into lines, and the line parameters were estimated. Finally, the lines were tracked from each ALI interval to the next, and the resulting line histories were stored on tape. The navigation reconstruction (Ref. 21) for each ALI interval was merged with the line histories to be readily available to the editing and display processors. Each of the algorithms for line formation, parameter estimation, and tracking will now be described.

(S) Line formation is the procedure whereby the detected cells from an ALI interval are grouped together as lines on the basis of the cell parameters. Ideally, all of the detected cells with signals emanating from the same source (i.e., projector frequency, auxiliary equipment, or propulsion system harmonic) will be formed into a single line. The parameters of intercell frequency proximity and bearing proximity (multibeam sensors only) were used as the basis for line formation decisions. The S/N of each detected cell could also have been used. However, the algorithm initially specified for use in this study (Ref. 9) ignored this clue; therefore, all successive iterations on the algorithm also ignored it.

(S) The initial algorithm specified that <u>contiguous</u> detected cells be clustered together as cell groups. A bearing gate was then to be applied to each cell group. This bearing gate would cause each cell group to be formed into one or more lines. The bearing gate was specified as ±35° for standard resolution data and ±65° for vernier resolution data.

(S) The performance of the above algorithm was evaluated using known projector lines. It was found that a single projector line frequently

FIGURE I-26
LINE RELATED PROCESSOR FLOW DIAGRAM (U)

AS-79-46

(S) resulted in multiple formed lines. Further investigation revealed that a single projector line would frequently result in multiple cell groups (noncontiguous detected cells) and that the bearing estimates were less stable than the bearing gates permitted. There are several candidate causes for these effects, including Doppler smearing during the 5 min ALI, multipath Doppler differences and frequency interference, source instabilities, and estimator errors due to the low S/N of some of the detected cells in each group. The formation of multiple lines for each projector line resulted in poor line tracker performance. The duration of each of the formed lines was short, resulting in short holding times, even when continuous detections were obtained.

(S) This "overformation" of projector lines was eliminated by broadening the frequency and bearing gates. A brief survey of the data resulted in a frequency gate of 12 cells for vernier data, which was followed by a bearing gate whose width was dependent on the intercell frequency spacing (Fig. I-27). The final line formation algorithm was the following.

(S) Consecutive detected cells are formed into a single line if

(1) the frequency difference between consecutive detections is less than or equal to 12 cells for vernier data or two cells for standard data, or

(2) if bearing estimates are available, the bearing difference in degrees between consecutive detections, times the frequency difference in cells, must be less than or equal to 90.

The bearing estimates were computed via the method described in section II, and were corrected for magnetic variation by the addition of approximately 340°. The bearing difference was computed by

$$\Delta B = \min\left(|B_i - B_j|,\ 360 - |B_i - B_j|\right) \quad .$$

(C) The revised line formation algorithm was found to perform well on projector lines, in that multiple lines were seldom formed. This

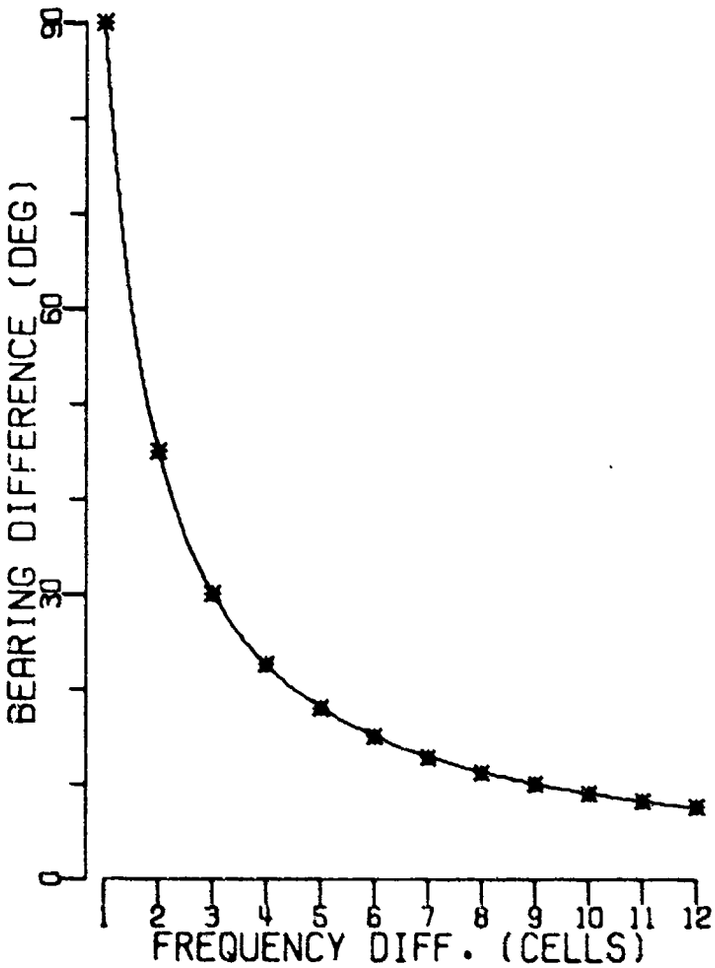

FIGURE I-27
LINE FORMATION BEARING DIFFERENCE TOLERANCE
AS A FUNCTION OF FREQUENCY DIFFERENCE (C)

AS-79-47

(C) reduction in line loading clearly improved line tracker performance. The broadening of the frequency and bearing gates also caused an increase in the false association rate. One possible effect is that closely spaced lines (doublets) may be formed into a single line.

(C) An approximation to the false association rate can be obtained by modeling the occurrence of detected cells in each ALI spectrum as a Bernoulli process, where each Bernoulli trial is an independent single cell detection decision. Initially assume that the success rate P_s is equal to the probability of false alarm. Since the number of successes in n trials of a Bernoulli process is described by the binomial probability mass function (PMF), the probability of not detecting another cell within the next 12 cells can be expressed as

$$P_{ND} = \binom{12}{0} P_s^0 (1-P_s)^{12-0}$$

$$= (1-P_s)^{12} \quad .$$

Therefore, the probability that another detection will occur within the next 12 cells and be incorrectly formed with the previous detections (ignoring the bearing gate) is

$$P_F = 1 - P_{ND}$$

$$= 1 - (1-P_s)^{12} \quad .$$

If the false alarm rate were chosen to be 10^{-3}, the false association rate would be 0.012. This implies that only one line out of 100 would be incorrectly grouped. To verify this model, the distribution of cell gaps between detected cells was measured and fitted with the appropriate binomial PMF (Fig. I-28). The corresponding success (detection) and false association rates are

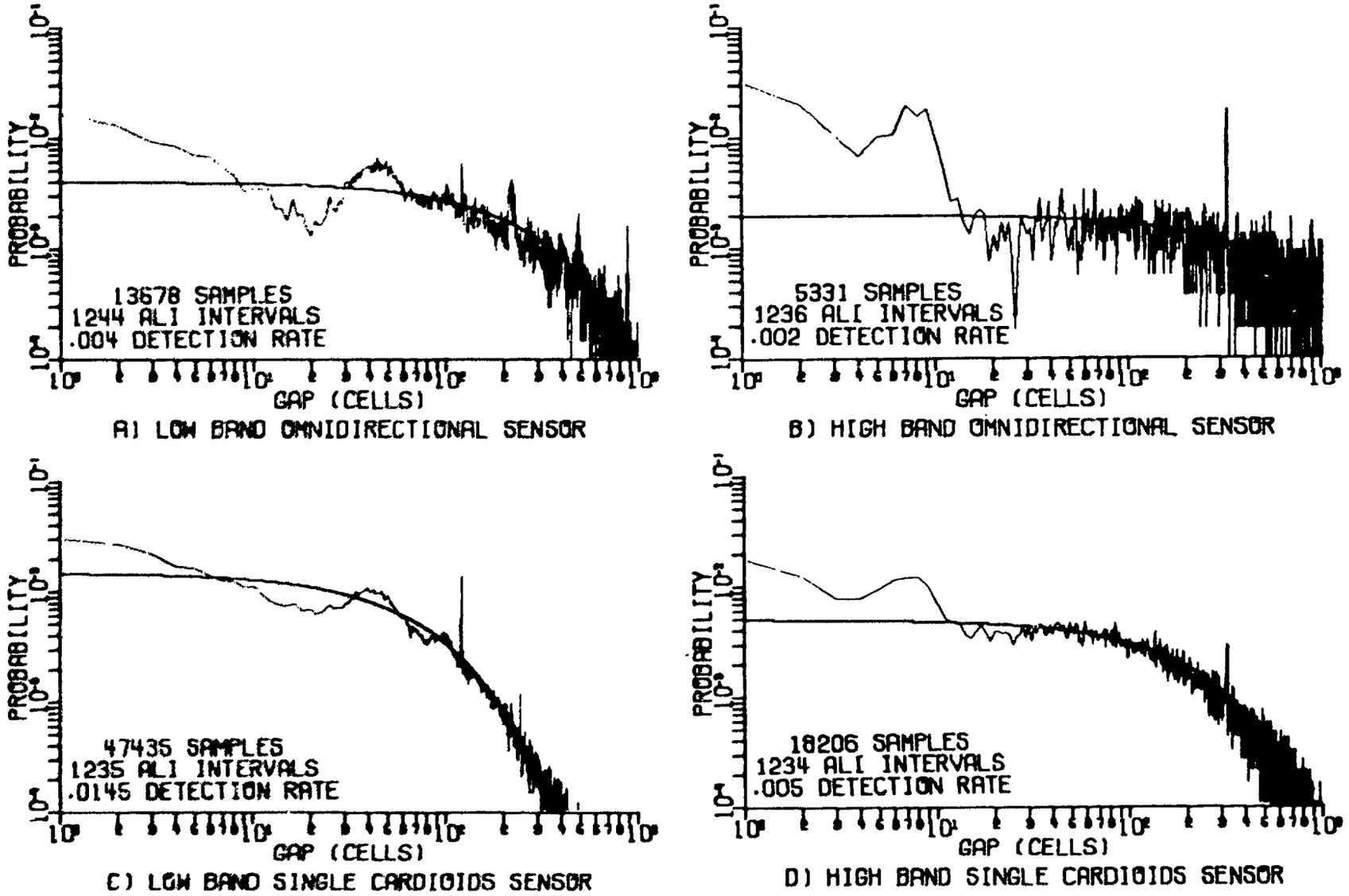

FIGURE I-28
VERNIER RESOLUTION DETECTED CELL GAP DISTRIBUTIONS (U)

ARL:UT
AS-77-2551
JLW
20-3-76

CONFIDENTIAL

(C)

(A)	P_s = 0.004	P_F = 0.047	,
(B)	= 0.002	= 0.024	,
(C)	= 0.0145	= 0.161	, and
(D)	= 0.005	= 0.058	.

The false association rates for (C) and (D) were later reduced by application of bearing gates, and the effect of any residual error was minimized by selecting line parameter estimators which were insensitive to them.

(C) The following parameters were estimated for each beam (i) of a formed line. (Integrals are actually summations over the detected cells.)

- NOISE LEVEL = $\int N_i(f)df / \int df$, where $N_i(f)$ is the mean background ASF level for each detected cell of beam i.
- MAXIMUM S/N = maximum S/N of any detected cell of beam i = the maximum over all detected cells on beam i of $\{\text{signal SPL}/[N_i(f)/(1.5\ \Delta f)]\}$, where Δf is the frequency spacing between Fourier coefficients, and 1.5 Δf is the equivalent noise bandwidth of a Hanned spectra.
- MAXIMUM SIGNAL LEVEL = signal SPL of the maximum S/N cell of beam i normalized by 1.5 to correct for the Hanning window.
- TOTAL SIGNAL LEVEL = $\int S_i(f)df$, where $S_i(f)$ is the signal level estimate for each detected cell of beam i.
- TOTAL S/N = TOTAL SIGNAL LEVEL/NOISE LEVEL.

The maximum estimates are used to address detection issues. The total estimates are similar to those used in the previous ARL:UT FVT study and to those predicted by most models.

(C) The following parameters were estimated for each formed line.

- POWER MEAN FREQUENCY = $\int f s_j(f)df \Big/ \int S_j(f)df$, where j is the beam with the maximum S/N for the detected cell of frequency f.

- rms BANDWIDTH $= \left[\int (f-F)^2 S_j(f)df \Big/ \int S_j(f)df\right]^{1/2}$

$$= \left[\int f^2 S_j(f)df \Big/ \int S_j(f)df - F^2\right]^{1/2} ,$$

where F is the POWER MEAN FREQUENCY.

- SIGNAL BEARING $= \arctan\left\{\dfrac{\int \sin[B_s(f)]\times S_j(f)df}{\int \cos[B_s(f)]\times S_j(f)df}\right\}$,

where $B_s(f)$ is the noise bearing estimate of the detected cell at frequency f.

- NOISE BEARING $= \arctan\left\{\dfrac{\int \sin[B_n(f)] \Big/ S_j(f)df}{\int \cos[B_n(f)] \Big/ S_j(f)df}\right\}$,

where $B_n(f)$ is the noise bearing estimate of the detected cell at frequency f.

Note that the line bearing estimators are simply weighted summations of the cell bearing estimates, where the weight is the signal SPL on the beam with maximum S/N, or its inverse. The detected cell noise bearing estimates are computed in the same manner as the signal bearing estimates.

(C) Any received signal is expected to occupy more than one frequency cell. Even if the analysis bandwidth were made sufficiently coarse and the ALI interval sufficiently short so that Doppler shifts, multipath effects, and source instabilities were contained in a band whose width was less than the analysis resolution, the received signal would still occupy more than one cell because of the sidelobe leakage of the FFT. This suggests that signal detection should be performed by techniques which utilize this phenomenon. Consider for example a detector where two adjacent cells are required to exceed a threshold. The threshold would be determined

(C) so as to maintain the desired false alarm rate against stationary Gaussian input data. This determination would need to account for the crossfrequency correlation induced by overlapped FFT processing. The resultant threshold would be lower than a single cell threshold with the same false alarm rate. This technique could be generalized into a matched bandwidth detector which would contain multiple bandwidths and their associated thresholds. The MDS of the matched bandwidth detector would be significantly lower than that of a single cell detector. Such a technique, for detecting lines instead of single cells, would also eliminate the necessity for line formation, and should lead to better line parameter estimates.

(C) The final function of the line related processor (Fig. I-26) was line tracking. The estimated line parameters were used to link the lines detected during the current ALI interval to the current set of active line histories. If the line could not be linked, a new line history was created. Line histories were purged from the active set after failing to be linked during a specified number of contiguous ALI intervals.

(S) The initial line tracker specification (Ref. 9) used frequency and bearing proximity as the basis for a linking decision. For linking, the current line was required to be within a frequency gate and a bearing gate (±30°) of an active line history. The frequency gate was

$$0.2 \text{ Hz} + 0.01 \times (\text{center frequency of line history})$$

for standard resolution, and

+ 1 cell, - 2 cells in the 50 Hz region,
+ 2 cells, - 4 cells in the 150 Hz region, and
+ 2 cells, - 8 cells in the 300 Hz region

for vernier resolution. After a line was linked, the line history frequency and bearing were to be updated by

(S) updated frequency = (old frequency + new frequency)/2

and

updated bearing = (old bearing + new bearing)/2.

(C) When applied to known cw signals, the performance of this line tracker was found to be poor. Even though the projectors were being towed at low speed (5 kt), the line tracker gates were insufficiently wide to link their detections. The result was that several short line histories were formed for each projector line. Line tracker performance measures (i.e., holding time) were not evaluated by this study, but a fair performance level was required so that the desired measures (i.e., percentage detection) could be obtained. To provide this performance level, a new tracking algorithm was evolved. The sole selection criteria applied to this algorithm was its performance against known projector lines.

(C) The revised line tracking algorithm consists of a distance function and a four-step link selection procedure. The distance function was designed to provide a measure of the similarity between a line and a line history. The parameters used by this measure were frequency proximity, bearing proximity (if available), and S/N. Other clues such as bandwidth and line dynamics were not investigated. A general purpose link selection procedure was first devised, and then used to evaluate several distance functions.

(C) During the first step of the link selection procedure, the distance between each formed line and each line history was computed. If the distance was less than some fixed maximum (D_{max}), the line history was added to the list of candidate links for that formed line. As many as seven candidate links were allowed for each line. During the second step, the preferred link was selected from the list of candidate links for each sensor. The highest preference was given to the line history with the most detections (longest). If the longest histories were of

(C) equal length, the closest (smallest distance) history was preferred. If the histories were equally close, the highest frequency history was preferred. This ordering was evolved through many iterations on the data. The longest history criterion is especially essential for the proper tracking of known cw signals. For example, because of a course change within an ALI interval, two lines were sometimes formed at significantly different frequencies from a single projector line. If the longest history criterion was not applied during the following ALI interval, the precourse change history would not be linked to postcourse change detections. Two examples of this, during a single projector tow, will be shown in Fig. I-31.

(C) During the third step of the link selection procedure, conflicts are resolved between lines having the same preferred line history. Preference is given to the closest line. Finally, when all of the conflicts have been resolved, the fourth step is performed. All of the formed lines for which links have been selected are now associated with the specified line histories. The line history parameters (frequency, bandwidth, S/N, and bearing) are updated by

$$\text{updated value} = (\text{old value} + \text{new value})/2 \quad .$$

Those formed lines for which no link was selected are used to create new line histories.

(C) Line histories were purged from the active list after six consecutive ALI intervals during which no new links were generated. The active list had a capacity of 400 line histories.

(C) The form of the distance function was designed to meet the anticipated worst case tracker requirements for these data. When the projector platform was proceeding along a straight line radial track at a significant range (>10 nmi) from the receiver, the frequency and bearing gates were required to be only as wide as the frequency and bearing estimator errors.

(C) Since the track was usually nonradial, the gates were widened to account for Doppler and bearing rates. Because of the low platform speed (<5 kt), these rates were small and could have been tracked by the initial algorithm.

(C) The tow platforms underwent frequent course changes, sometimes in excess of 120° (see Volume IV). Such course changes caused very large and rapid Doppler frequency shifts while leaving the bearing relatively constant. The normalized frequency shift for a course reversal along a 5 kt radial tow is 0.34% of the signal frequency, where the effect of receiver depth has been ignored. The revised line tracker was therefore provided with a broad frequency gate whose width is proportional to the line history center frequency.

(C) The tow platforms frequently passed within close proximity of the receiver sites. Unlike course changes, both the Doppler frequency rate and bearing rate can become large at CPA. The maximum Doppler frequency rate occurs when the platform is directly above the receiver, and is equal to V^2/rc where V is the platform speed, r is the range at CPA, and c is the velocity of sound. For a 5 kt speed, 1525 m (5000 ft) deep receiver, and a 5 min ALI, the Doppler shift becomes approximately 0.09% of the signal frequency. The bearing estimate could change by 180° between two consecutive ALI intervals about CPA. In addition, the bearing estimates become less stable when the platform is directly above the DIFAR sensor.

(C) The large frequency shifts and small bearing shifts due to course changes, and the smaller frequency shifts and large bearing shifts at CPA, suggested that the line tracker use a distance function of the following form.

$$D = \alpha\Delta f/f + \beta\Delta b \quad ,$$

(C) where Δf and Δb are the frequency (hertz) and bearing (degree) differences between a line and its candidate line history, f is the frequency (hertz) of the line history, and α and β are constants. This function allows one gate to broaden as the other narrows, thus matching the anticipated conditions.

(C) When values for α and β were chosen to permit the line tracker to perform well with the known projector lines, the performance against clutter was extremely poor. Unrelated, spurious detections were tracked as lines, resulting in increased processor loading. The predominant characteristic of these false line histories was that they were composed of lines with very low S/N. The form of the distance function was therefore modified to discriminate against such links by narrowing the frequency and bearing gates for low S/N lines.

$$D = \alpha\Delta f/f + \beta\Delta b - \gamma\left[(S/N)_L + (S/N)_H\right] \quad ,$$

where S/N_L and S/N_H are the signal-to-noise ratios (dB//Hz) of the line and the candidate line history.

(S) After several iterations, it was heuristically determined that a frequency difference of 1.5 vernier cells at 50 Hz was equivalent to 1 dB S/N, which was equivalent to 0.1° bearing difference. The generalized form of the distance function was

$$D = 6144\,\frac{\Delta f(\mathrm{Hz})}{f(\mathrm{Hz})} + 0.1\,\Delta b(\mathrm{deg}) - \left[S/N_L(\mathrm{dB//Hz}) + S/N_H(\mathrm{dB//Hz})\right] \quad .$$

The maximum distances for which linking was allowed (D_{max}) were chosen as 36, if bearing was available, and 30, if not. For example, lines on single beam (no bearing) sensors with vernier threshold levels (-15 dB) were not allowed any frequency difference, whereas high level signals (0 dB) were allowed frequency rates of up to 0.49%. Little weight was placed on bearing because of the rapid changes expected at short range. The value of this clue would be increased if it were known when the

(S) source was at short range. It should be possible to obtain such a clue from the DIFAR estimate of vertical arrival angle achievable with the vertical sensor discussed in section II. Time did not permit this investigation to be included in this study.

(C) The form of the line tracker distance function involves the implicit assumption that the signal should occur at the same frequency and bearing during each ALI interval. Any deviation from the historic values causes an increase in the distance measure. Also, the historic values are updated in a manner that implies that only a portion of the measured change is real. The effect, when the line is undergoing real frequency and bearing shifts, is to successively increase the distance along the real link, and thus increase the probability of error. Another technique that merits consideration is that used in the BEARTRAP program (Ref. 22). The frequency and/or bearing rates could be estimated from recent line history values and used to predict the future values of these parameters. The distance function would then be based on the predicted values. In addition to decreasing the chance of error, this technique furnishes estimates of line dynamics which are of value for other functions such as signature formation. Also, if a target was being tracked, but insufficient lines were available for classification, these parameter estimates could be used to key a dynamic line integrator (DLI) process (Ref. 23) and thereby increase the probability of detection on other related target lines.

(C) The line tracker distance function was evaluated for several edited projector line histories, and the values plotted in Figs. I-29 and I-30. The lines on each figure denote the restrictions on linking imposed by the current function. These figures reveal that most, but not all, of the links could survive more stringent restrictions. The advantage of tighter linking criteria is a lower clutter (line/processor loading) rate. The figures also reveal that a few of the correct links were rejected by the current criteria. These links were added in a later manual editing stage. Automatic generation of accurate line histories

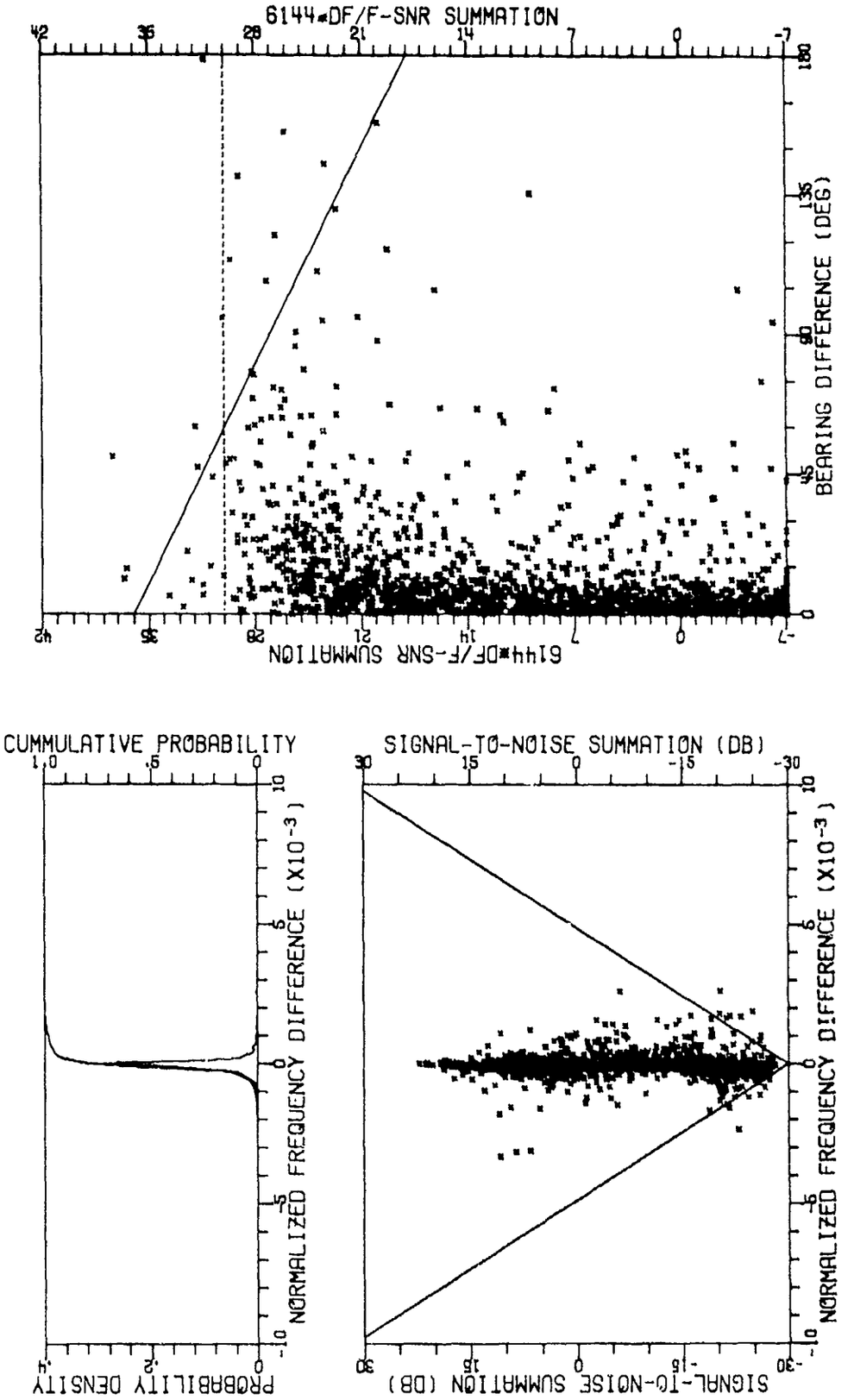

FIGURE I-29
LINE TRACKER DISTANCE FUNCTION VALUES FOR THE 17 NOV PROJECTOR LINES AS OBSERVED WITH THE SINGLE CARDIOIDS SENSORS AND VERNIER RESOLUTION (U)

AS-79-48

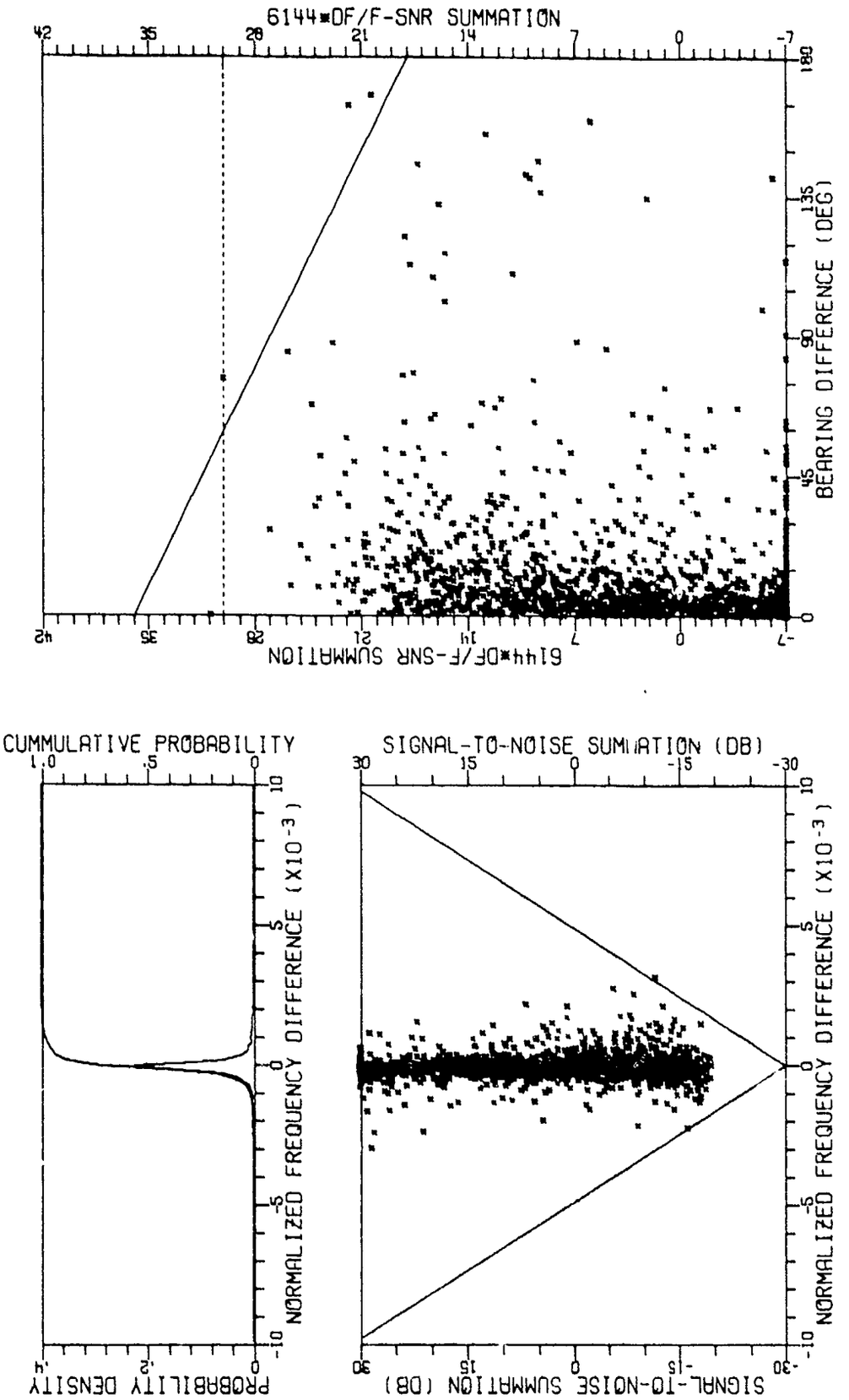

FIGURE I-30
LINE TRACKER DISTANCE FUNCTION VALUES FOR THE 17 NOV PROJECTOR LINES
AS OBSERVED WITH THE SINGLE CARDIOIDS SENSORS AND STANDARD RESOLUTION (U)

AS-79-49

(C) may also require a post-line-tracker routine which associates terminated line histories with new histories that have similar characteristics.

(S) Finally, the line formation and tracking algorithms that were developed for these data might not perform well on real data. Further revisions would be required to track high speed (≥10 kt) targets and/or those with unstable lines (Ref. 24).

(C) The line histories output by the line related processor were manually edited prior to the generation of final data products. This editing was accomplished by means of high resolution detection history plots such as Fig. I-31. All of the detected lines in a 2 Hz band centered about each projector frequency were plotted as a function of time. Detections based only on a single cell of a single beam are denoted by X's. Multicell and/or multibeam detections are denoted by O's. Linking is denoted by dashed lines. Bearing is denoted by a solid line emanating from each detection. The length of this line is proportional to S/N. Ground truth range nautical miles (nmi) and bearing (degrees) are plotted across the top. These kinds of displays were used to select which history, histories, or segments of histories corresponded to each projector line. Following history selection, the measured cw signal parameters were plotted as a function of time in the format of Fig. I-32. These line history plots and a description of their contents can be found in Volumes II and III. Following this editing and parameter extraction, detailed and summary cw data products were generated. These products and their descriptions are found in Volumes II through IV.

(C) The last data products to be generated by the cw measurement system, clutter statistics, were actually a measure of the ambient sound field. As such, it was desirable to eliminate any exercise induced artifacts. For example, Fig. I-33 contains all of the line histories from the single cardioids sensor at site A1 during the 17 November field event. Figure I-34 is an example of the corresponding clutter display for these data. Numerous lines were held throughout the 12 h interval. Closer inspection reveals

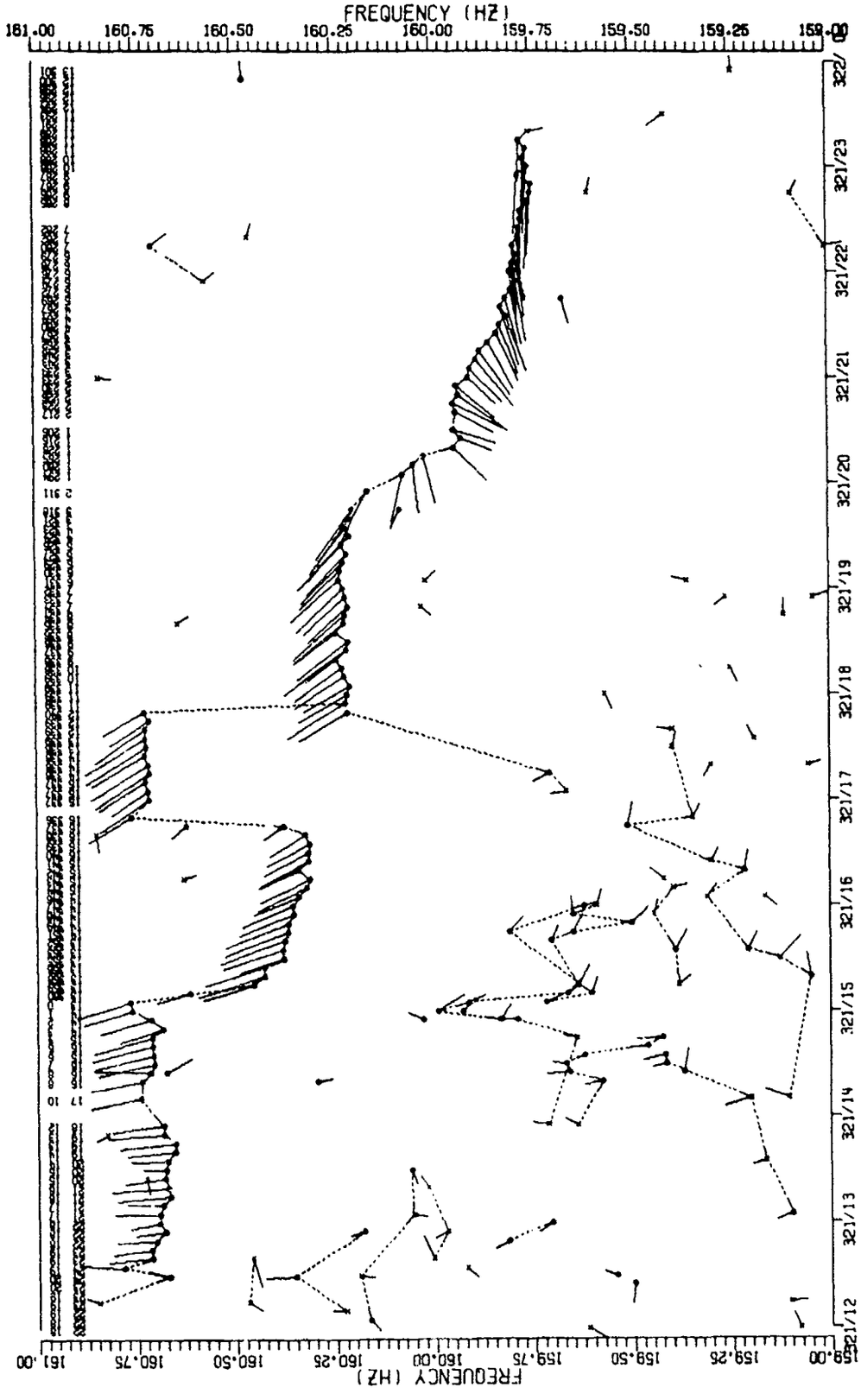

FIGURE I-31
EXAMPLE OF AN EXPANDED DETECTION HISTORY DISPLAY USED FOR TRACKER ASSESSMENT AND LINE HISTORY EDITING (U)

AS-79-50

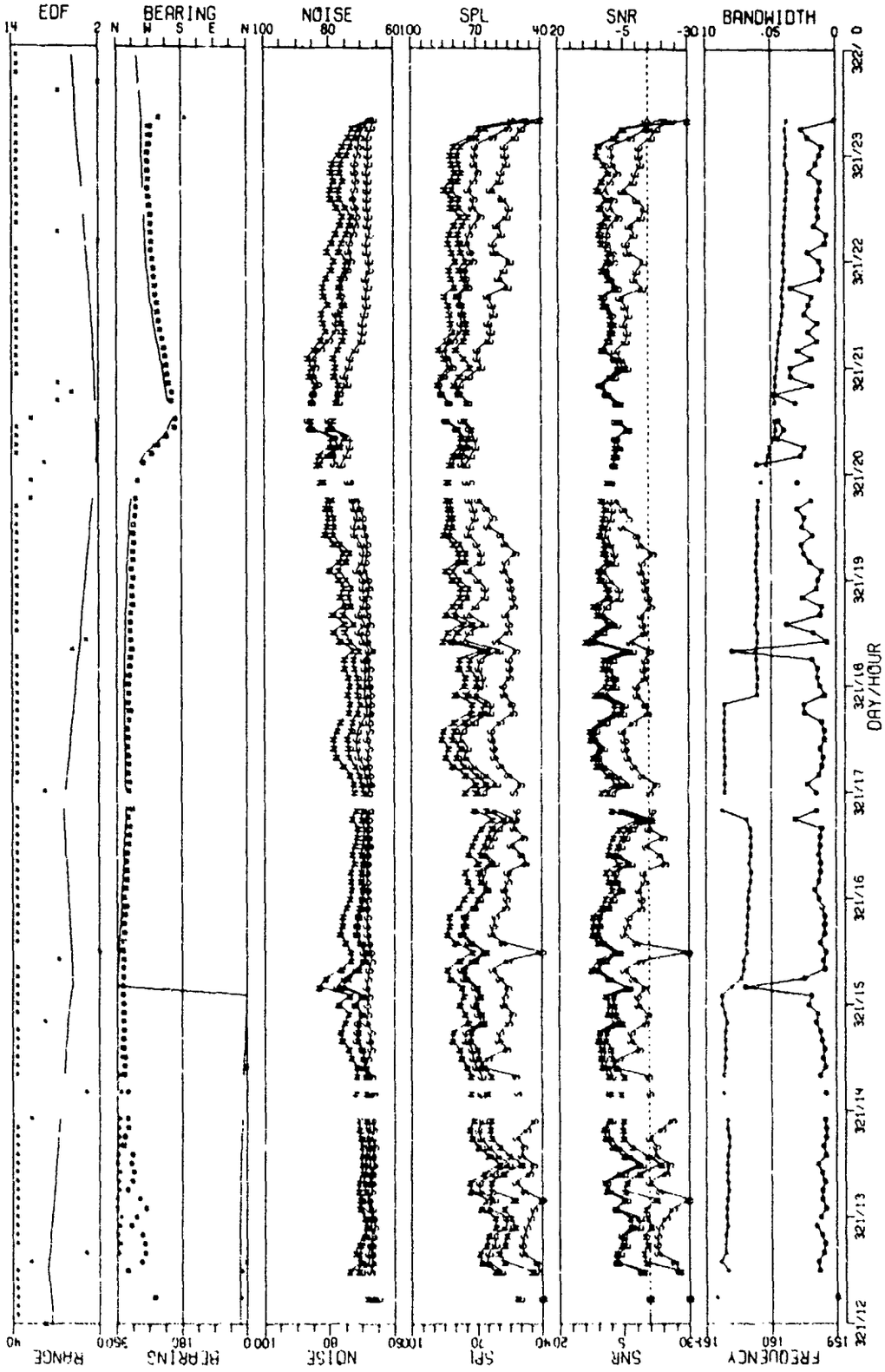

MSS-FVT 160 HZ LINE HISTORY AS OBSERVED VIA THE SINGLE CARDIOIDS SENSOR AT SITE A3 DURING THE 17 NOV FIELD EVENT WITH VERNIER RESOLUTION (U)

FIGURE I-32
EXAMPLE OF A LINE HISTORY DISPLAY (U)

AS-79-51

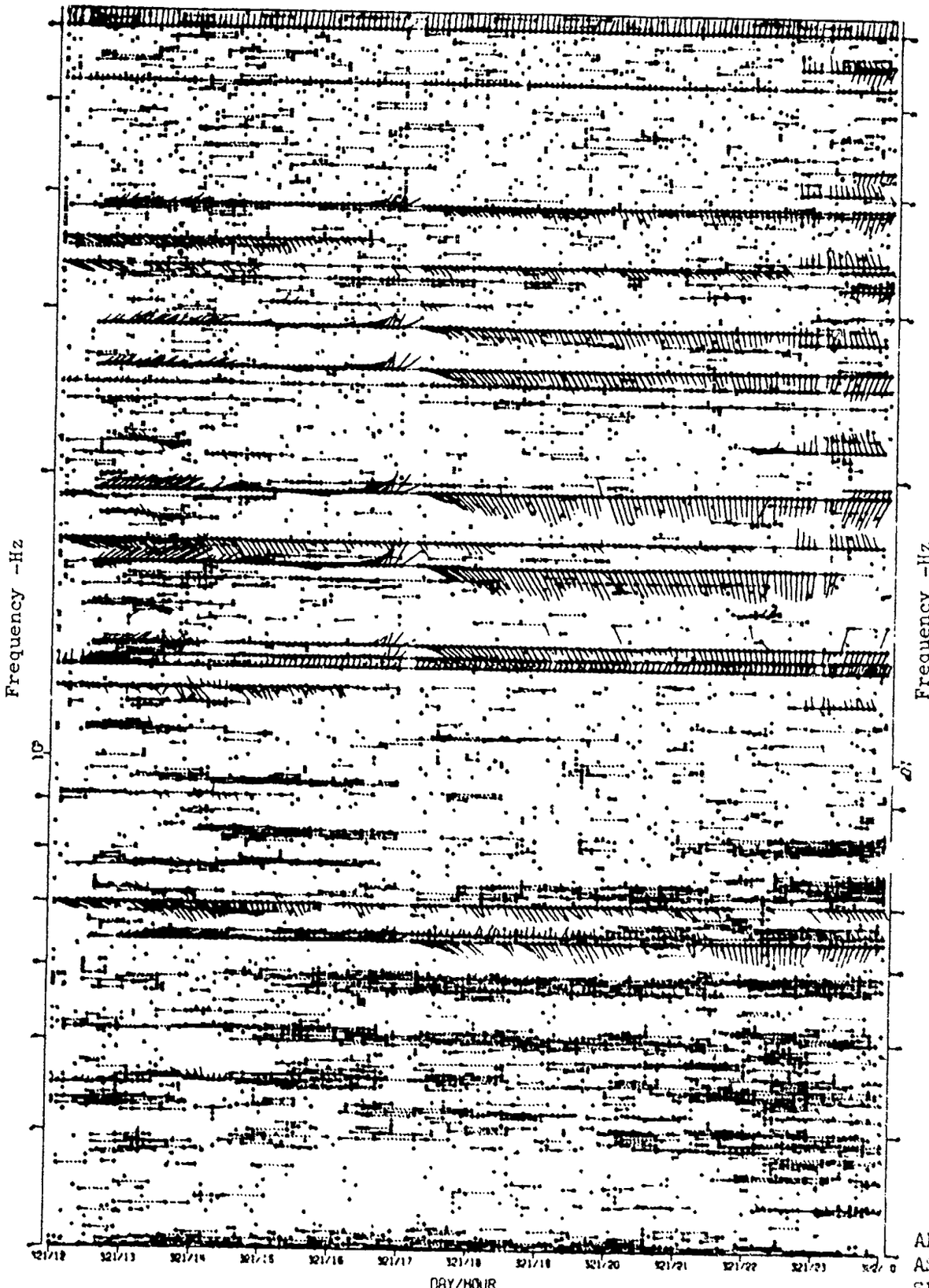

FIQURE I-33
MSS-FVT DETECTION OVERVIEW FOR SINGLE CARDIOIDS SENSOR
AT SITE A1 INCLUDING ALL EXERCISE RELATED LINES (U)

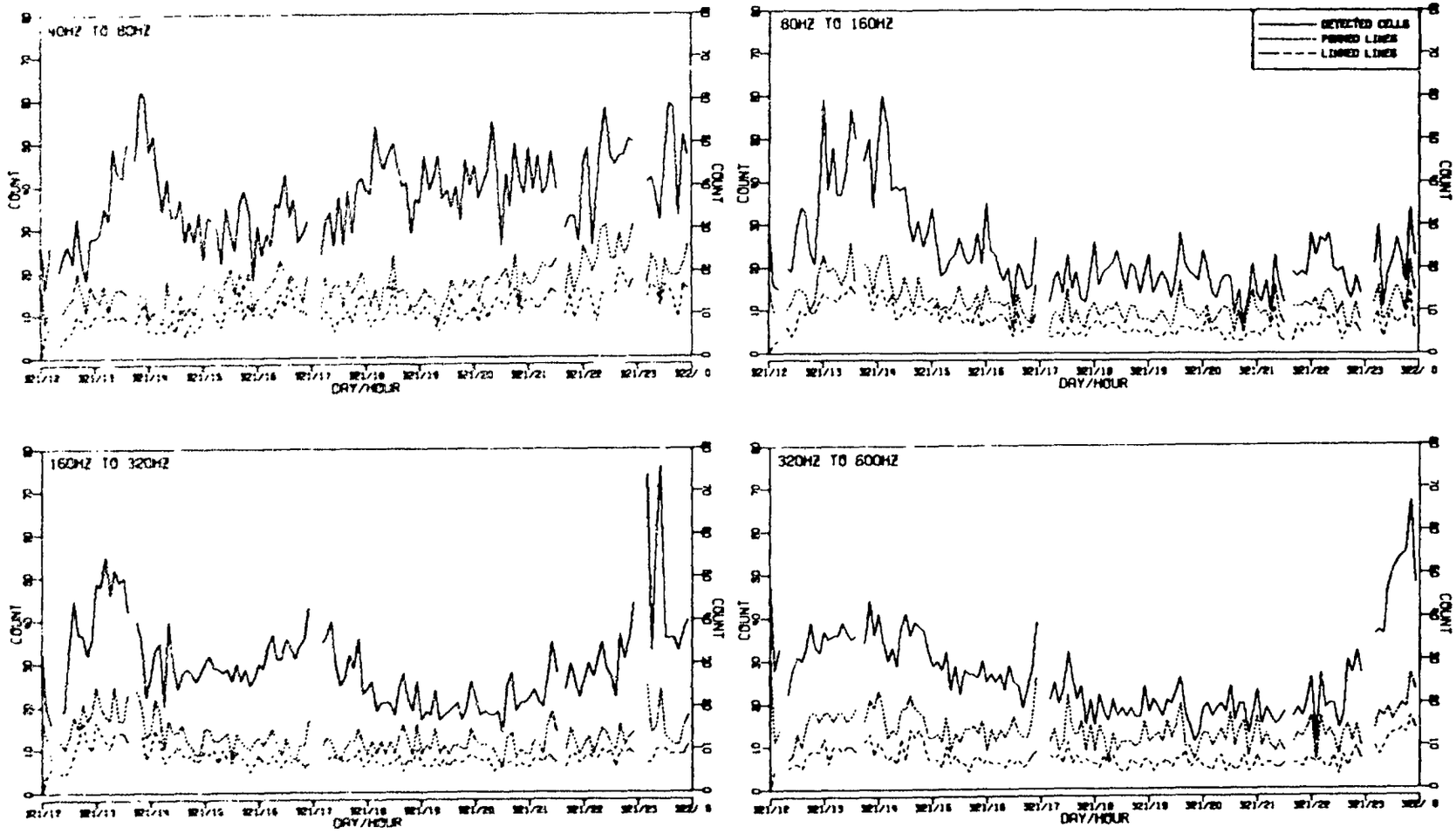

FIGURE I-34
MSS-FVT CLUTTER TIME SERIES FOR SINGLE CARDIOIDS SENSOR
AT SITE A1 INCLUDING ALL EXERCISE RELATED LINES (U)

AS-79-52

CONFIDENTIAL

(C) that many of these lines (Fig. I-35) emanated from a single projector platform (CFAV KAPUSKACING), even though only three lines appear in the projector operations logs. Many of the remaining lines (Fig. I-36) can also be attributed to exercise related sources (ACODAC, CFAV QUEST, and R/V CHAIN). When all of these known lines were eliminated (Fig. I-37), the remaining detections provided more accurate clutter measurements (Fig. I-38). All of the clutter results in this study were derived with a similar editing procedure. Even after editing, some exercise artifacts remain to bias the clutter measurements. The many high frequency lines of Fig. I-37 beginning at 321/2230 were due to the GNATS system aboard USS GREENLING (SSN 614). Additional GNATS lines can be observed at 321/1300 as USS GREENLING passed CPA. However, even if some residual artifacts remain, the edited clutter measurements are much more representative of the true values than the unedited measurements.

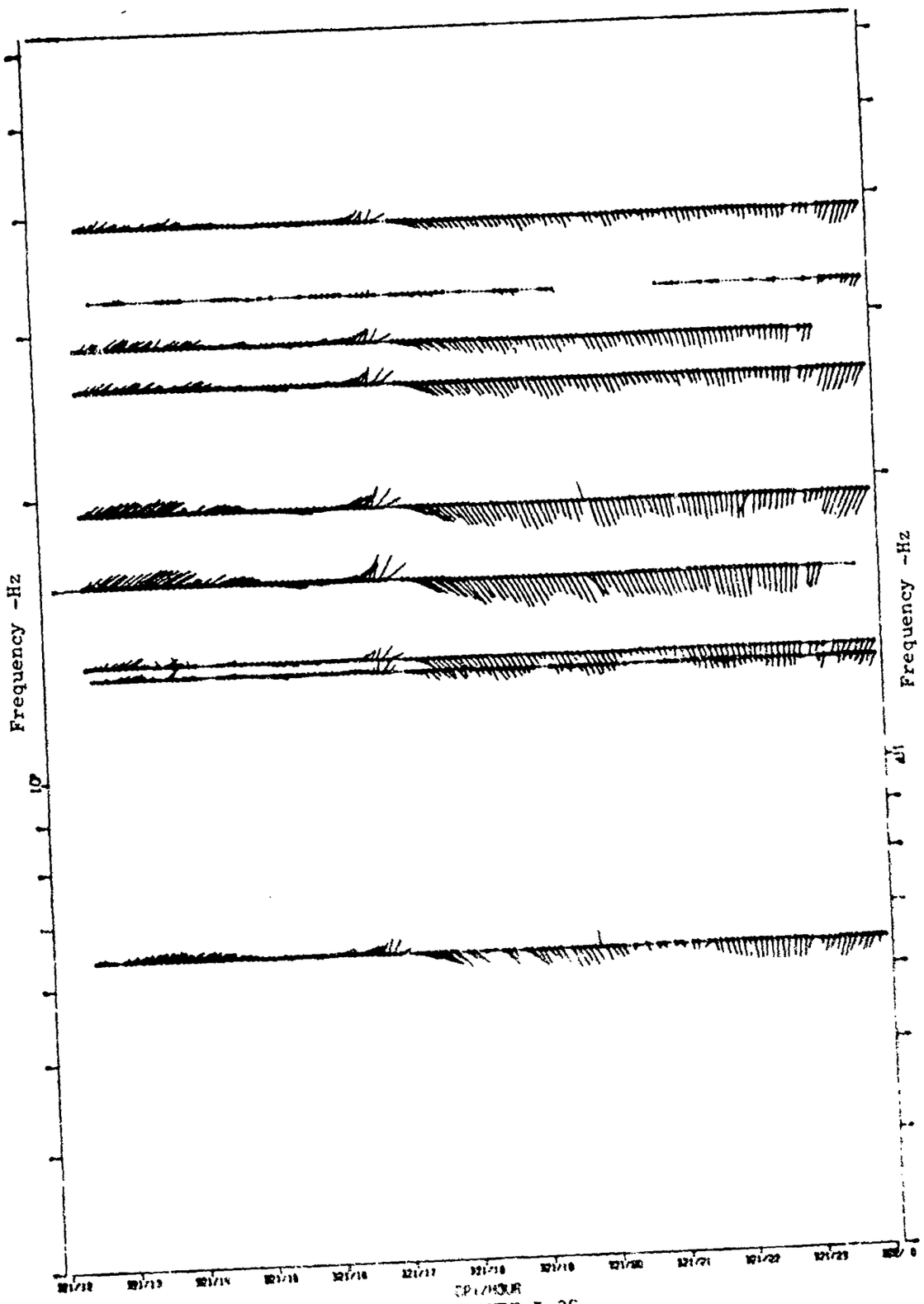

FIQURE I-35
MSS-FVT DETECTION OVERVIEW FOR SINGLE CAROIOIDS SENSOR
AT SITE A1 INCLUDING ONLY CFAV KAPUSKACING RELATED LINES (U)

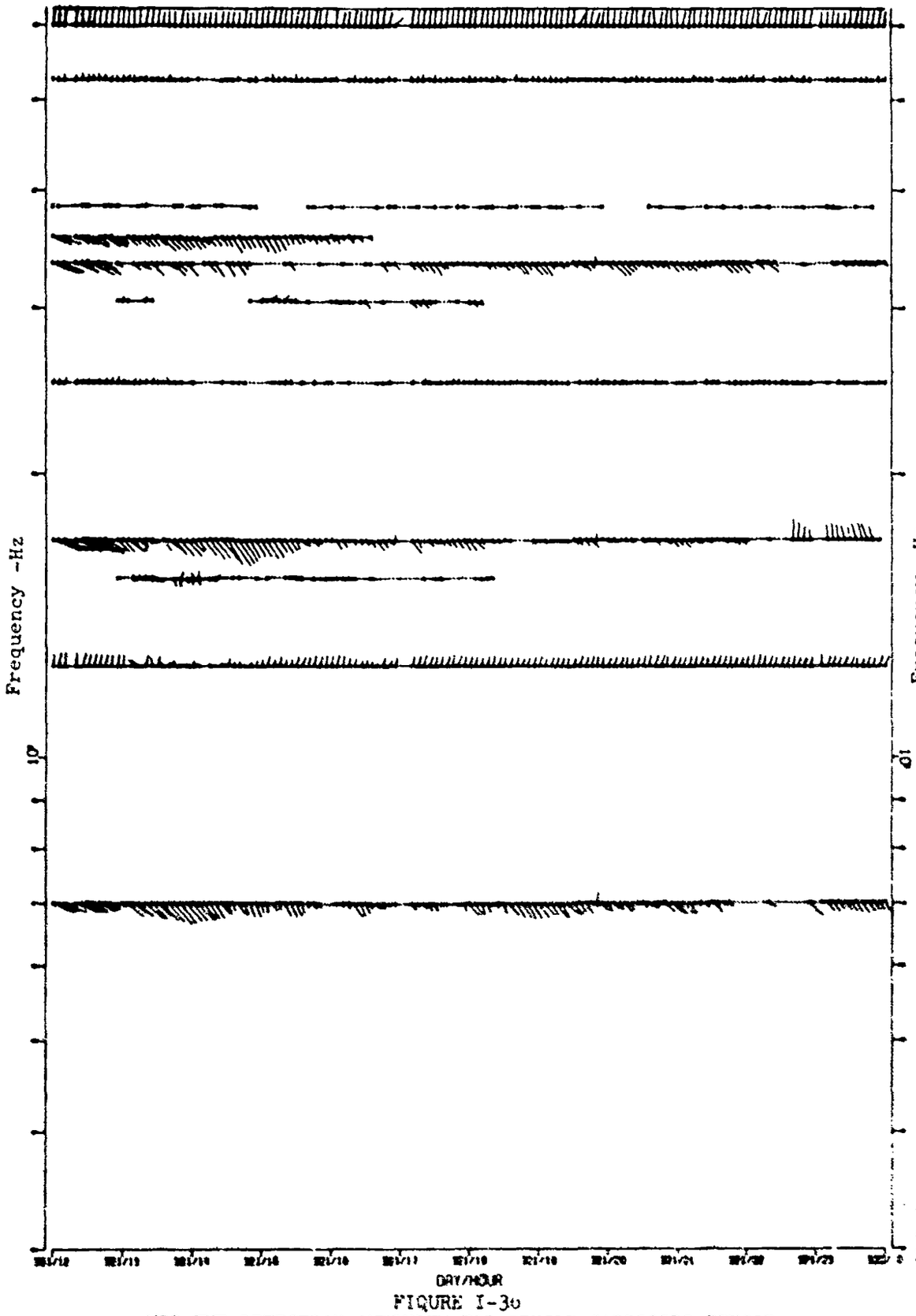

FIGURE I-36
MSS-FVT DETECTION OVERVIEW FOR SINGLE CARDIOIDS SENSOR
AT SITE A1 INCLUDING ONLY NON-KAPUSKACING EXERCISE RELATED LINES (U)

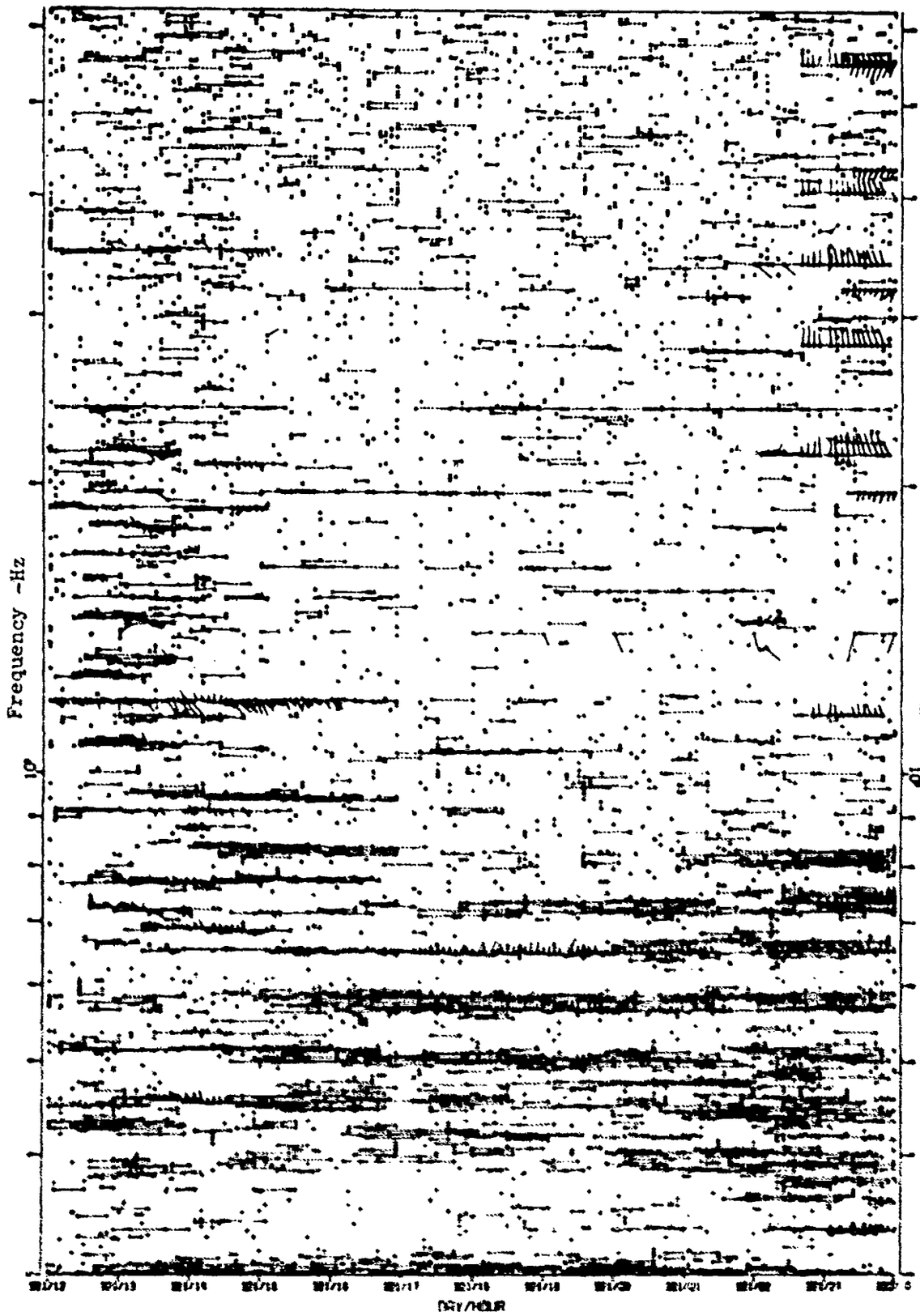

FIQURE I-37
MSS-FVT DETECTION OVERVIEW FOR SINGLE CARDIOIDS SENSOR
AT SITE A1 EXCLUDING ALL EXERCISE RELATED LINES (U)

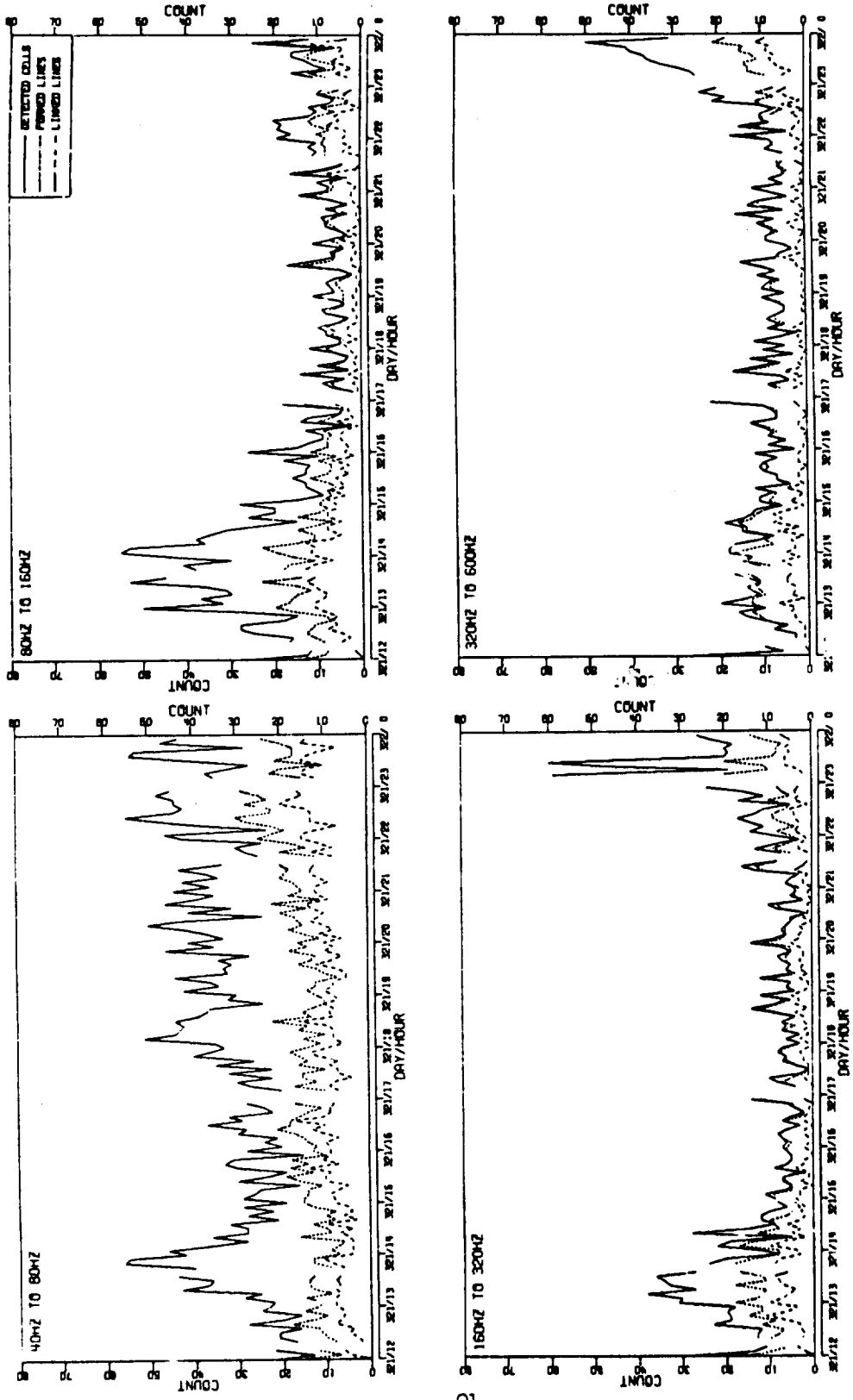

FIGURE I-38
MSS-FVT CLUTTER TIME SERIES FOR SINGLE CARDIOIDS SENSOR
AT SITE A1 EXCLUDING ALL EXERCISE RELATED LINES (U)

AS-79-53

(The reverse of this page is blank.)

VII. CONCLUSIONS AND RECOMMENDATIONS

(C) A measurement system, typical of those envisioned for use by MSS, has been developed at ARL:UT. The design was based on the current ARL:UT measurement system and on the guidelines provided by the sponsor. The algorithms were finalized after many trials and were evaluated on the basis of their performance against known projector lines. While clearly suboptimal, the performance of these algorithms was adequate for the purposes of this study. Several improvements to these algorithms were recommended for further study, including the following.

- Formation of a sensor with a vertical dipole response from a single DIFAR array.
- A recursive technique for background ASF estimation with improved accuracy and efficiency.
- A matched bandwidth detector technique with a lower MDS than that of the single cell detector currently in use.
- Use of a linear predictor by the line tracker to provide more accurate tracks and estimates of line dynamics for signature formation.
- A technique for vertical arrival angle estimation from a single DIFAR array, which in turn would furnish a range estimate to improve line tracker and signature formation performance.

(U) Finally, future sensor performance analysis will not necessarily require this type of processor, except to obtain clutter results. Rather, a cw measurement technique which takes advantage of the known source and source platform parameters would more readily provide projector line histories. Such histories would include measurements at low S/N, many of which would not be detected by the current processor. These histories could then be used to predict what would have been

(U) observed by other types of processors. These results would be more complete and more easily obtained.

REFERENCES

1. L. K. von Perbandt, "Contract N00039-77-C-0003 Government Furnished Information: for use in connection with, forwarding of" (U), Ser S690 of 22 April 1977. SECRET

2. M. H. Stripling and R. S. Hebbert, "Performance of DIFAR Using Adaptive Beamforming" (U), Naval Ordnance Laboratory Technical Report No. 73-202 (NOLTR 73-202), Naval Ordnance Laboratory, White Oak Laboratory, Silver Spring, Maryland, 27 November 1973. CONFIDENTIAL

3. D. J. Edelblutte, J. M. Fisk, and G. L. Kinnison, "Criteria for Optimum-signal-detection theory for arrays," J. Acoust. Soc. Am. 41, 199-205 (1967).

4. Robert J. Urick, Principles of Underwater Sound, 2nd ed. (McGraw-Hill, New York, 1975).

5. John P. Cookson, "BEARTRAP DIFAR/KANDE Processing" (U), Technical Report No. 76-67 (NSWC/WOL/TR-76-67), Naval Surface Weapons Center, White Oak Laboratory, Silver Spring, Maryland, 2 June 1976. CONFIDENTIAL

6. Ken Hawker, private communication, March 1978.

7. J. B. Franklin, "Surface Suspended Superdirective Arravs" (U), 29th U.S. Navy Symposium on Underwater Acoustics, Vol. II, 31 October 1972, p. 333. CONFIDENTIAL

8. C. N. Pryor, "Automatic Cardioid Formation for DIFAR Systems" (U), Technical Report No. 75-141 (NSWC/WOL/TR-75-141), Naval Surface Weapons Center, White Oak Laboratory, Silver Spring, Maryland, 15 August 1975. CONFIDENTIAL

9. Scott C. Daubin, "The ACODAC System," Woods Hole Oceanographic Institution Technical Report No. 72-87 (WHOI-72-87), Woods Hole Oceanographic Institution, Woods Hole, Massachusetts, November 1972 (unpublished manuscript).

10. "MSS Configured ACODAC Systems Final Engineering Report," Sanders Associates Technical Report No. 76-U127 (SAN-BOP- -U127), Sanders Associates, Inc., Nashua, New Hampshire, 15 January 1976. CONFIDENTIAL

11. R. Peterman, "Special Hardware for ARL Analysis of ACODAC Data, Volume II," ARL Technical Report (in preparation).

12. A. H. Nuttall, "Spectral Estimation by Means of Overlapped Fast Fourier Transform Processing of Windowed Data," Naval Underwater Systems Center Technical Report No. 4169 (NUSC-TR-4169), Naval Underwater Systems Center, New London, Connecticut, 13 October 1971.

13. A. H. Nuttall, "Estimation of Cross-Spectra via Overlapped Fast Fourier Transform Processing," Naval Underwater Systems Center Technical Report No. 4169-S (NUSC-TR-4169-S), Naval Underwater Systems Center, New London, Connecticut, 11 July 1975.

14. A. H. Nuttall, "Minimum Bias Windows for Spectral Estimation By Means of Overlapped Fast Fourier Transform Processing," Naval Underwater Systems Center Technical Report No. 4513 (NUSC-TR-4513), Naval Underwater Systems Center, New London, Connecticut, 11 April 1973.

15. A. H. Nuttall, "Probability Distribution of Spectral Estimates Obtained via Overlapped FFT Processing of Windowed Data," Naval Underwater Systems Center Technical Report No. 5529 (NUSC-TR-5529), Naval Underwater Systems Center, New London, Connecticut, 3 December 1976.

16. C. S. Penrod, "Statistical Characteristics of Power Spectral Estimates Derived from Higher Resolution FFTs," ARL Technical Report (in preparation).

17. S. L. Watkins, "MSS-FVT Ambient Sound Field and cw Propagation Measurements for Near-Bottom Sensors at Site A3" (U), Applied Research Laboratories Technical Report No. 76-52 (ARL-TR-76-52), Applied Research Laboratories, The University of Texas at Austin, 1 December 1976. CONFIDENTIAL

18. J. A. Shooter and S. L. Watkins, "Estimation of background ambient noise levels from the spectral analysis of time series with application to cw propagation loss measurements," J. Acoust. Soc. Am. 62, 84-90 (1977).

19. Handbook of Mathematical Functions, National Bureau of Standards, Washington, DC, June 1964.

20. C. N. Pryor, "Minimum Detectable Signal for Spectrum Analyzer Systems," NATO Advanced Study Institute on Signal Processing, Vol. 1, 1972, pp. I-7.1 - I-7.16.

21. E. H. Nosenchuk, "MSS-FVT Track Reconstruction/Navigation Data Assessment Analysis," Naval Air Development Center Technical Report No. 76229-60 (NADC-76229-60), July 1976.

22. J. R. Williams and G. G. Ricker, "Digital Line Trackers," Interstate Electronics Corporation, 10 December 1971.

23. S. J. McCarthy, "Frequency-Line Detection and Tracking Processes" (U), Naval Undersea Center Tech. Publ. No. 492 (NUC TP 492), January 1976. CONFIDENTIAL

24. C. N. Pryor, "Practical Limits of Resolution and Integration" (U), Naval Ordnance Technical Report No. 72-235 (NOLTR 72-235), Naval Ordnance Laboratory, White Oak Laboratory, Silver Spring, Maryland, 31 July 1972. SECRET

(The reverse of this page is blank.)

APPENDIX I-A

STANDARD RESOLUTION INTERCHANNEL PHASE DIFFERENCES

(The reverse of this page is blank.)

(U) The following set of plots contains the measured interchannel phase differences as measured at the output of the ARL:UT measurement system. The first two plots contain measurements of the ARL:UT measurement system alone. The first set of measurements was performed just prior to digitization of the analog data; the second set was performed immediately following this digitization. The remaining plots contain before and after measurements based on the header calibration signals of the government furnished (GFE) analog tapes.

Data Identifier Format:

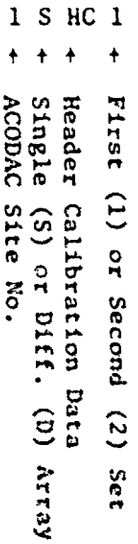

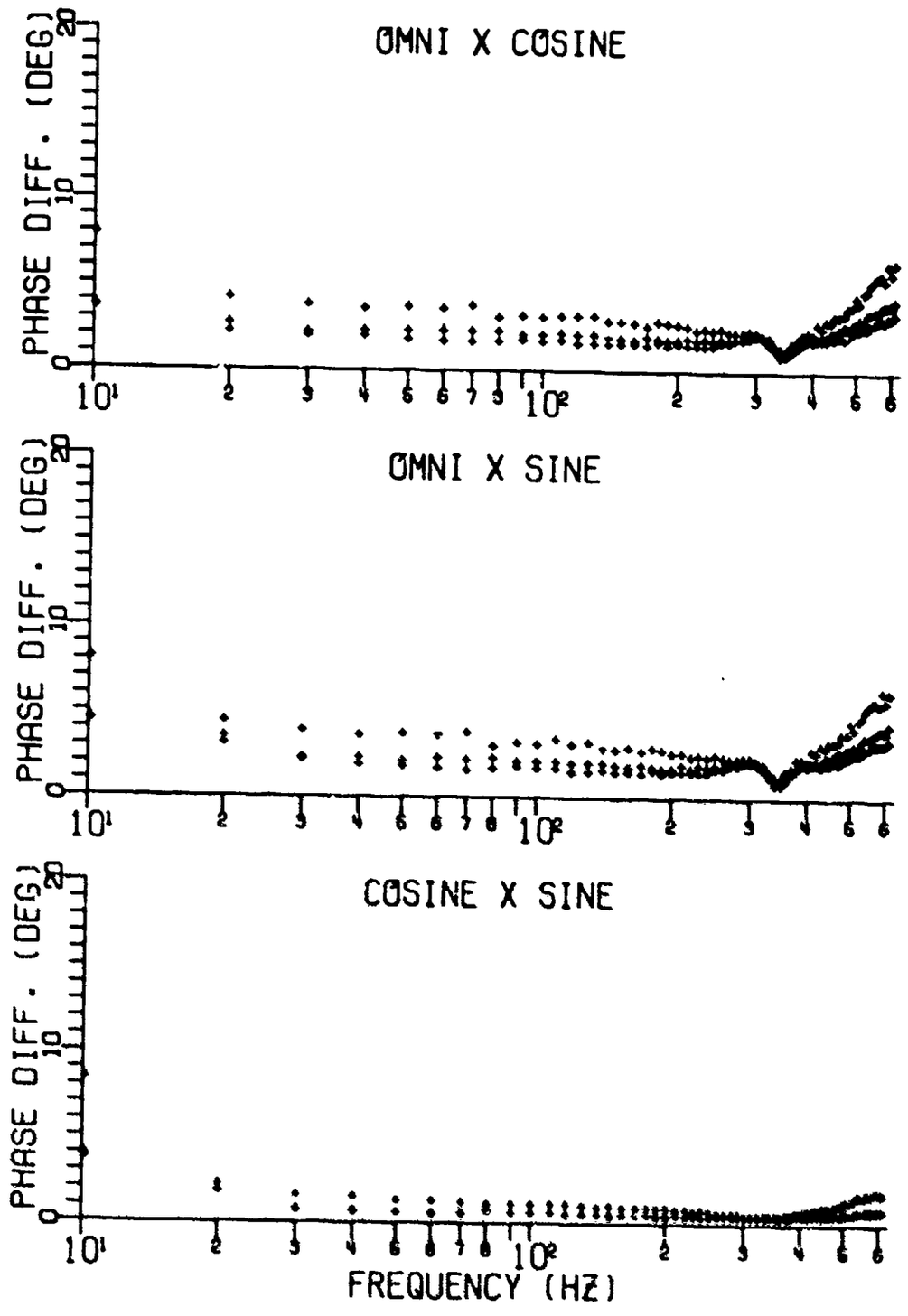

STDHWTST

Figure A-1

AS-79-54

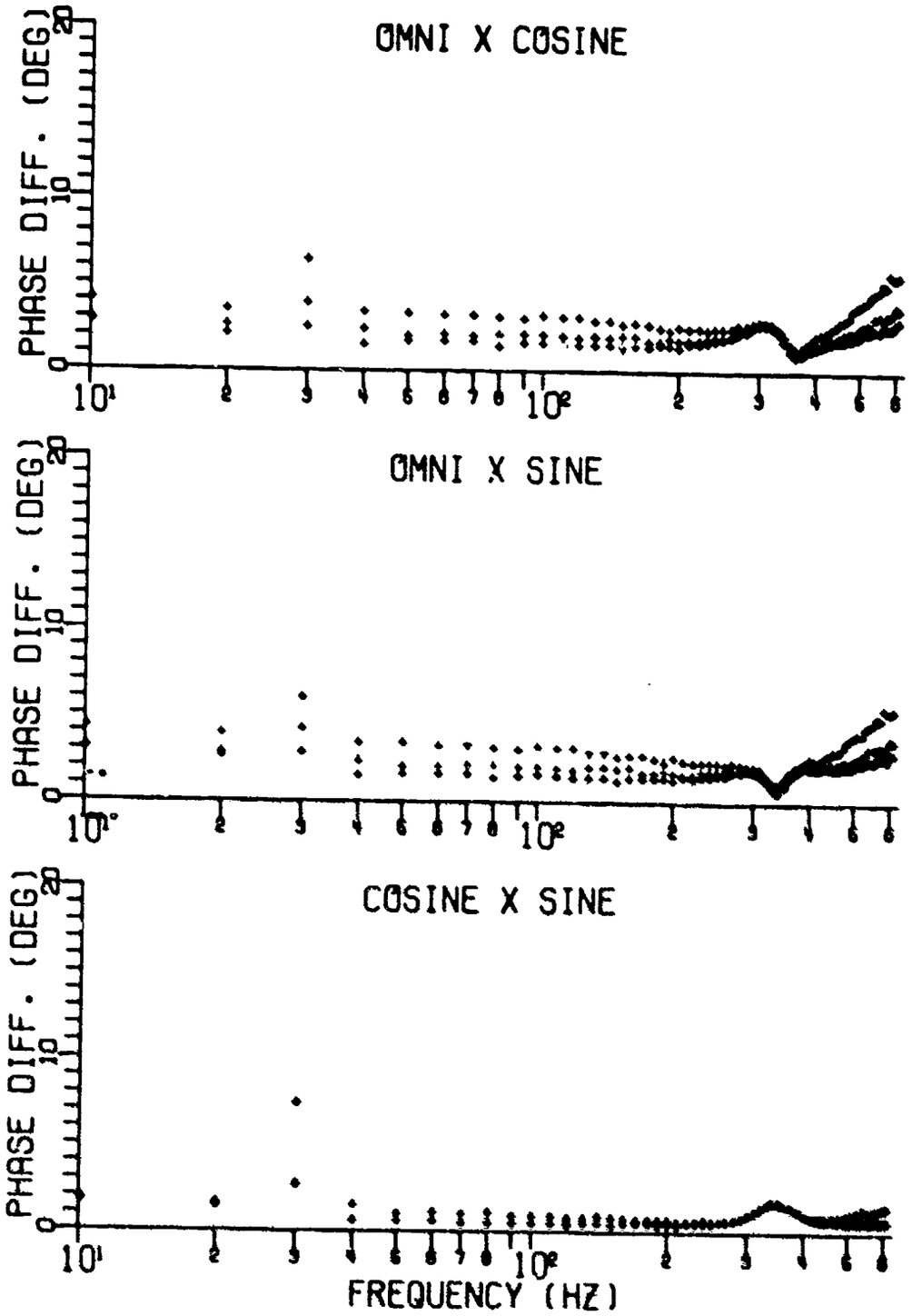

Figure A-2

AS-79-55

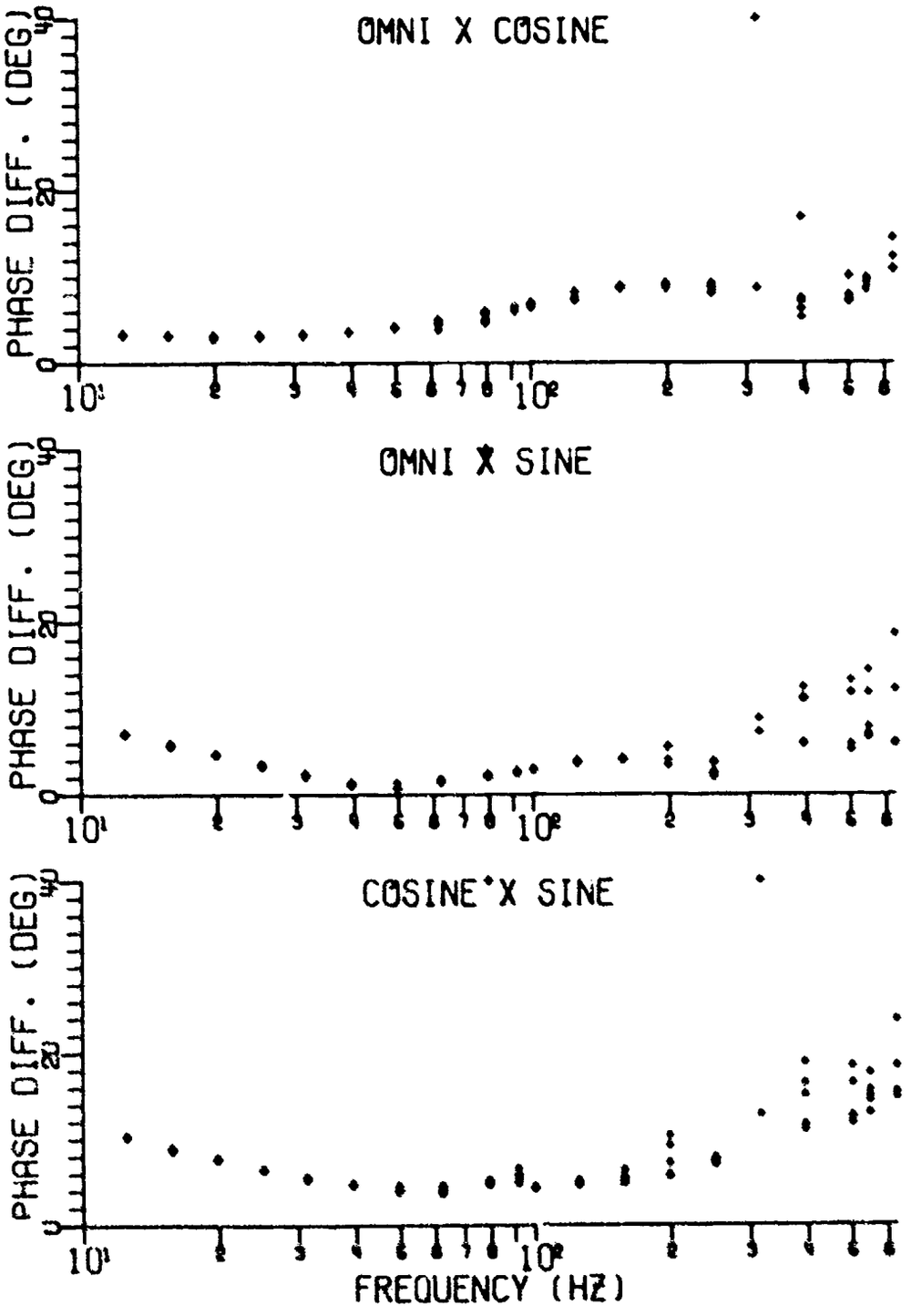

1SHC1

Figure A-3

AS-79-56

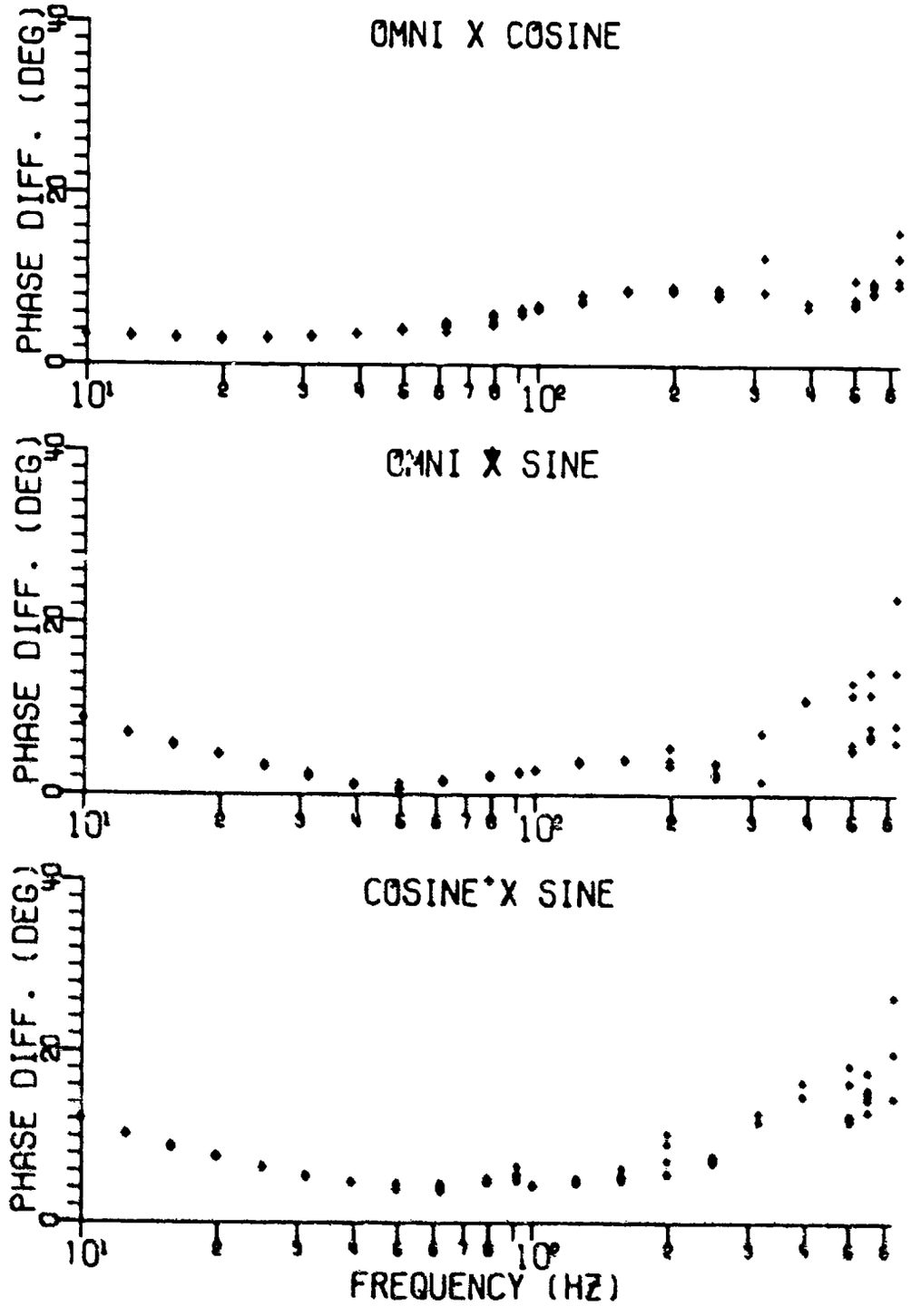

1SHC2

Figure A-4

AS-79-57

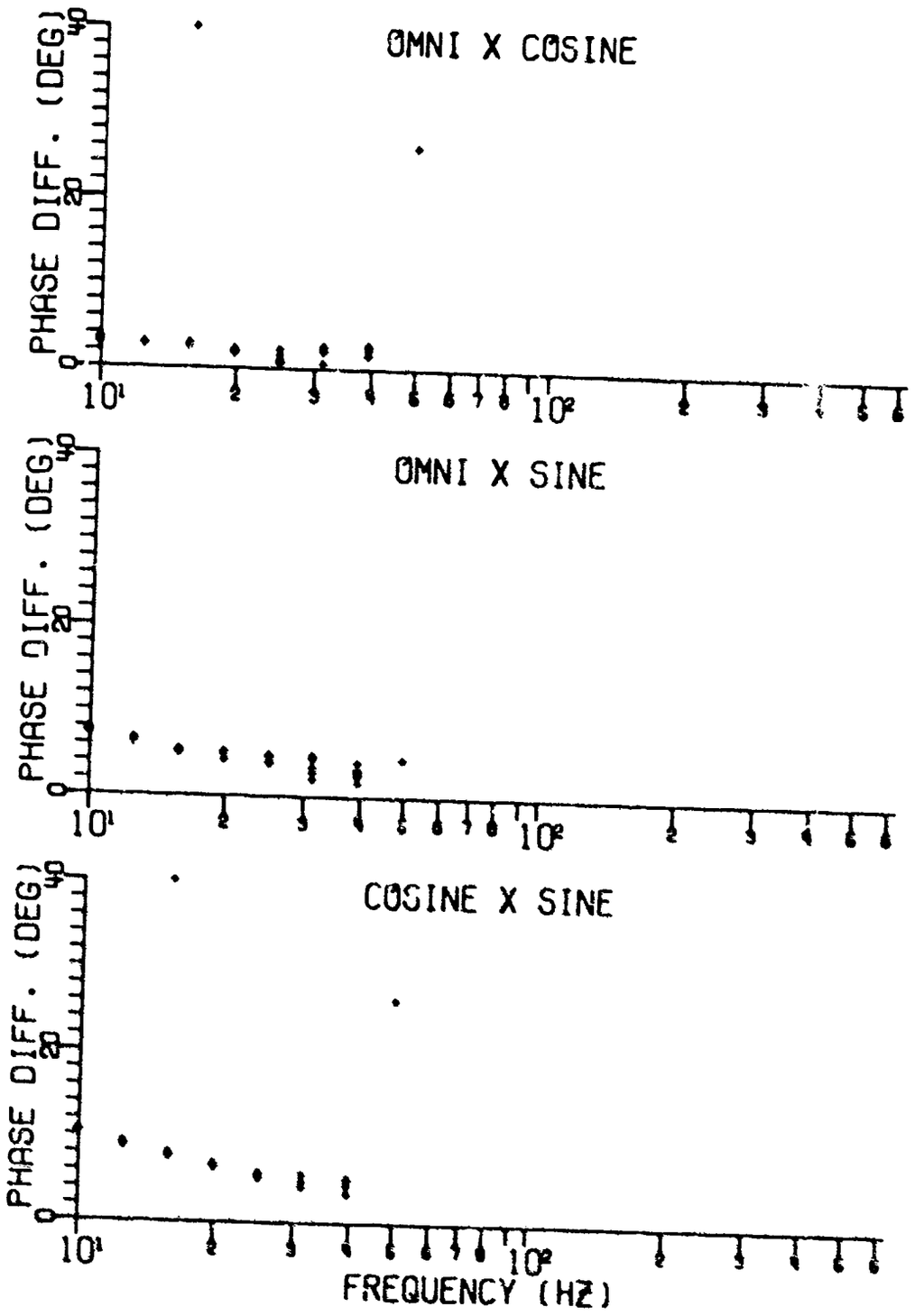

Figure A-5

AS-79-58

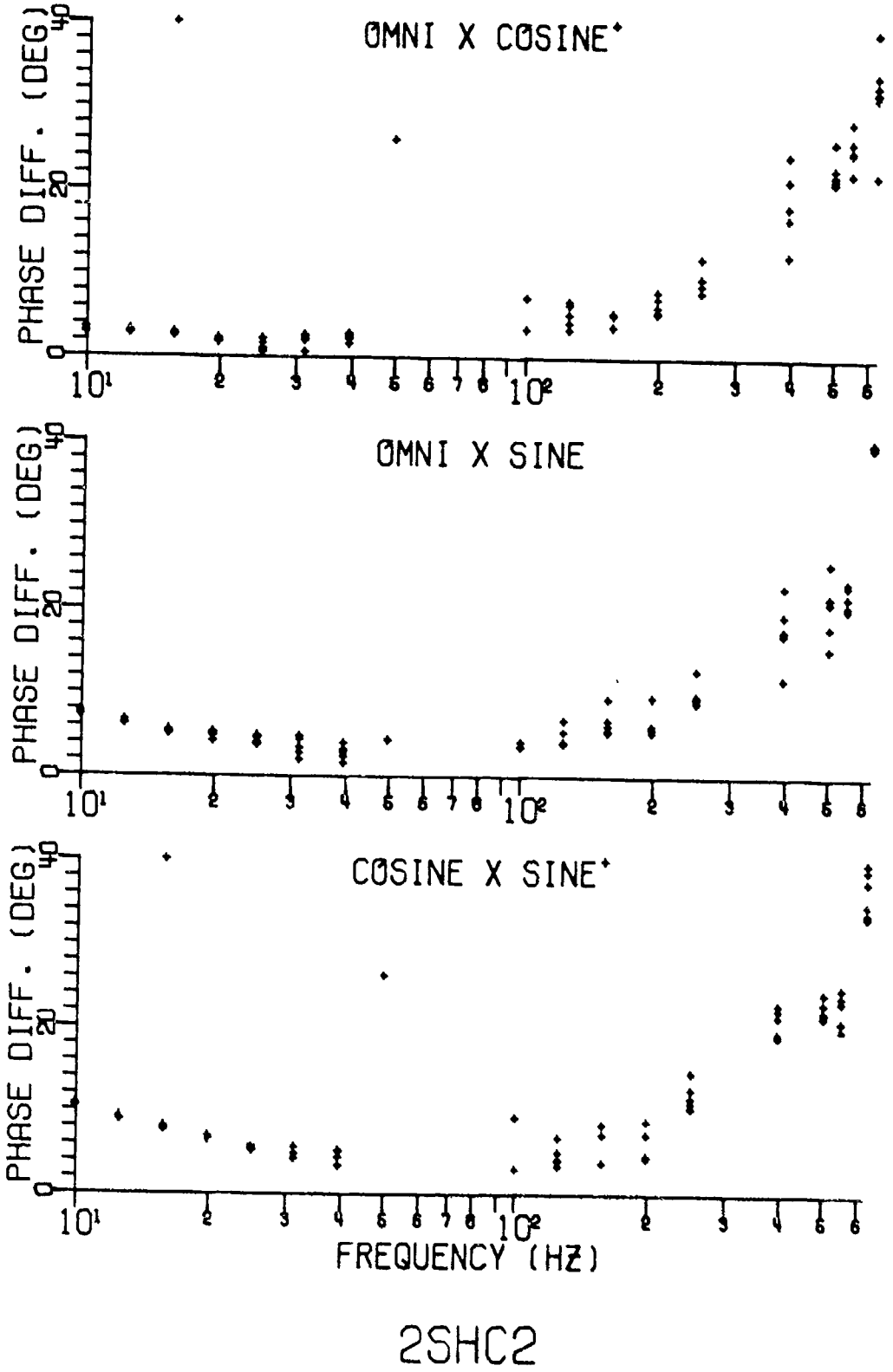

Figure A-6

AS-79-59

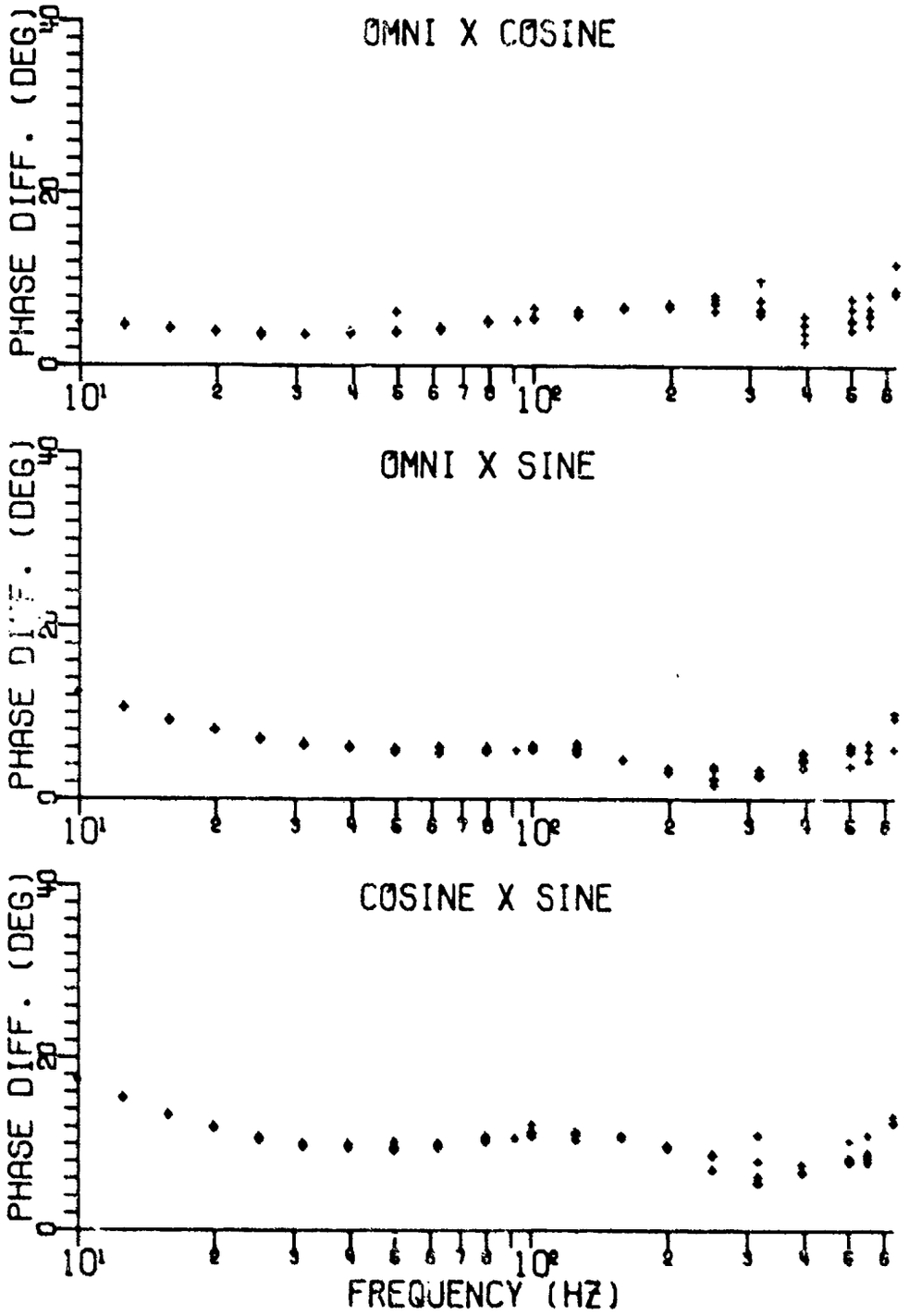

3SHC1

Figure A-7

AS-79-60

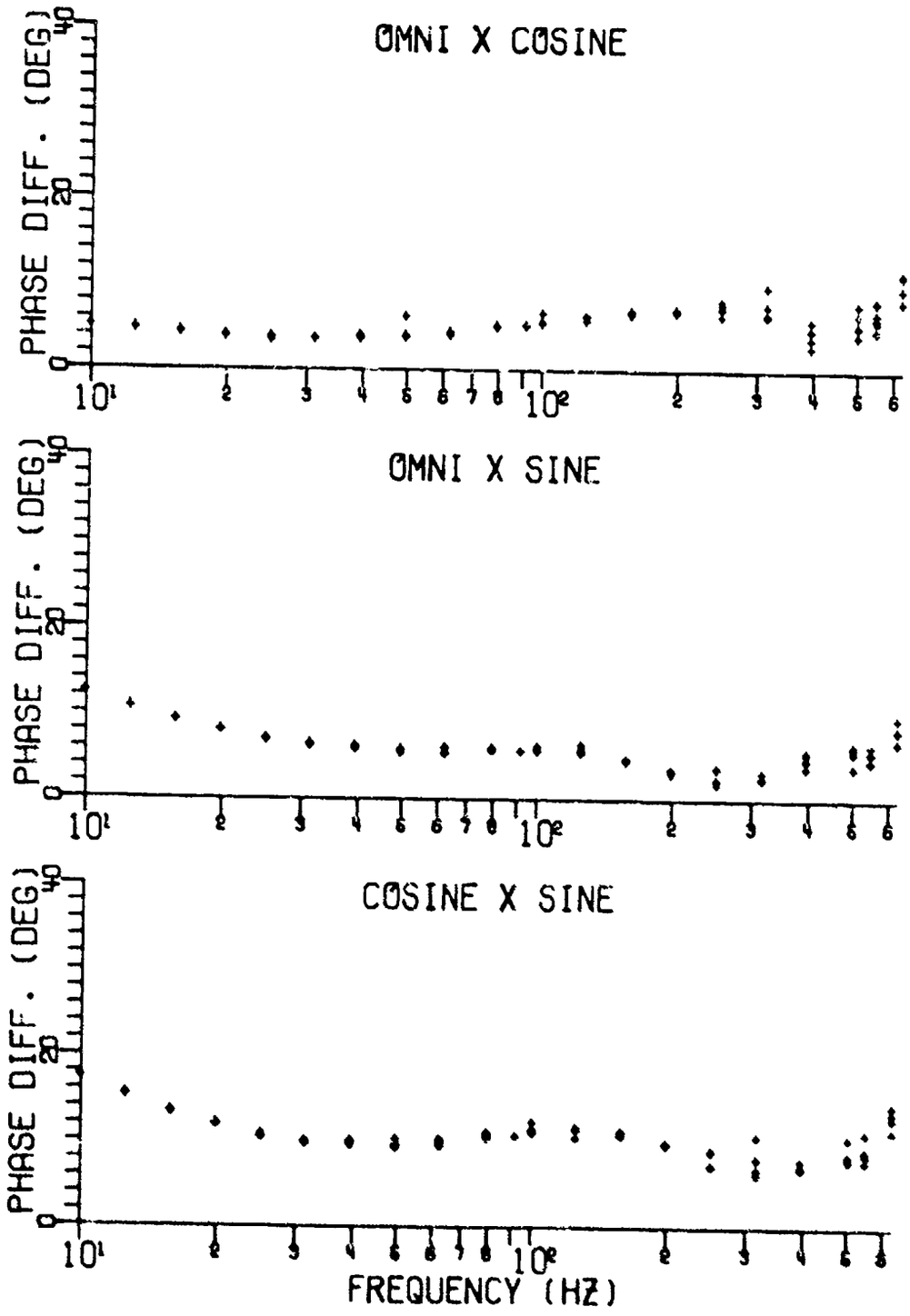

Figure A-8

AS-79-61

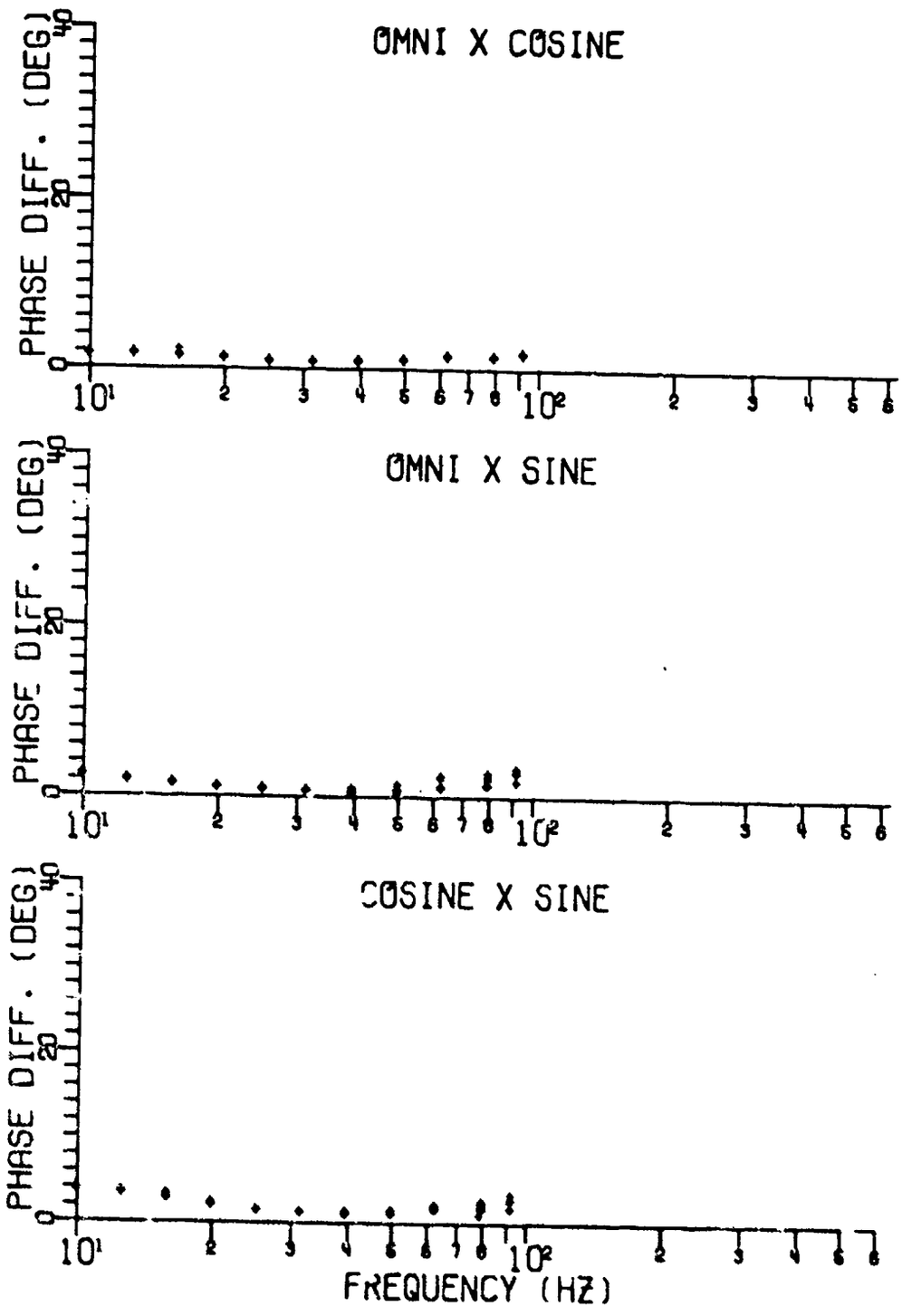

1DHC1

Figure A-9

AS-79-62

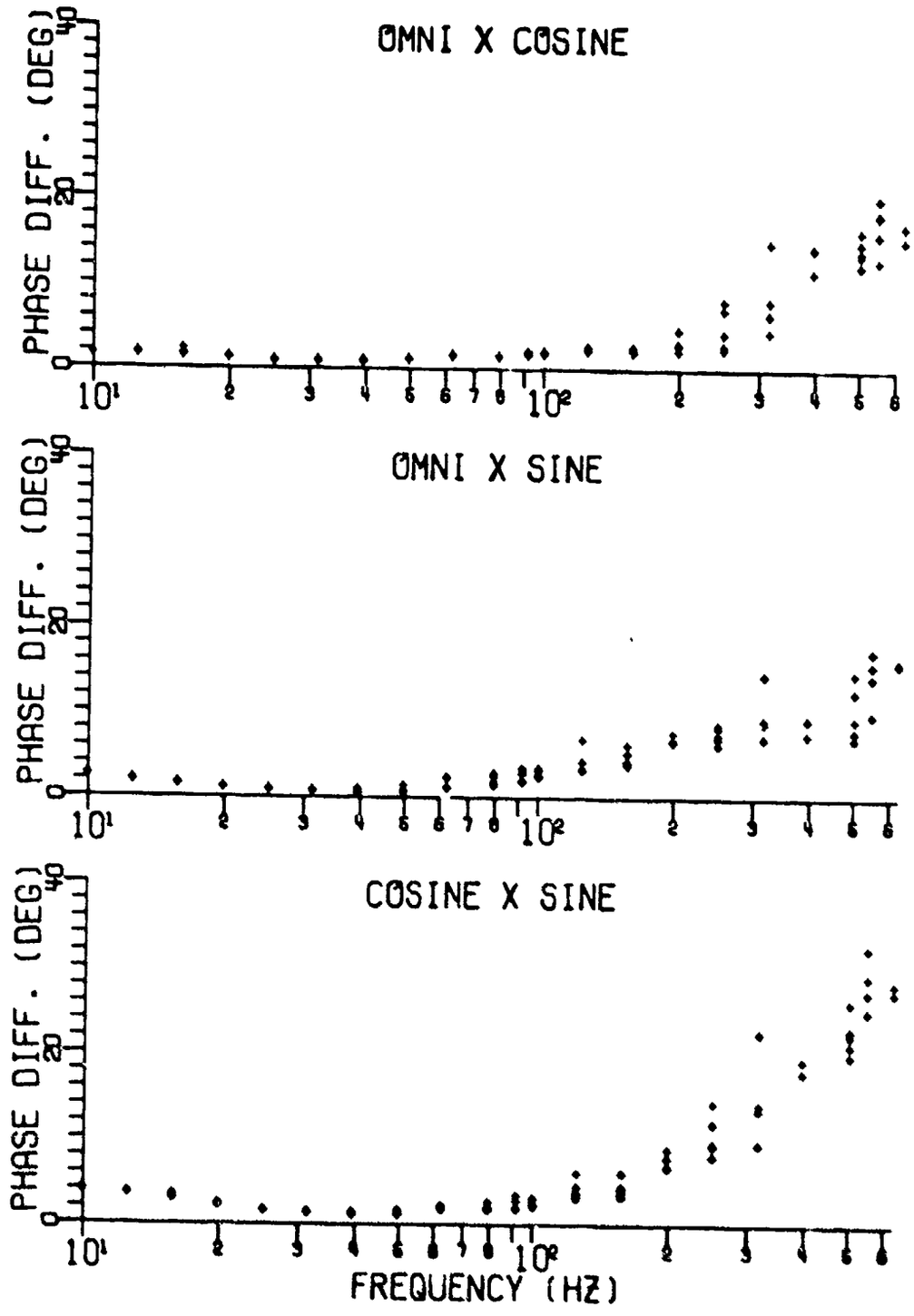

1DHC2

Figure A-10

AS-79-63

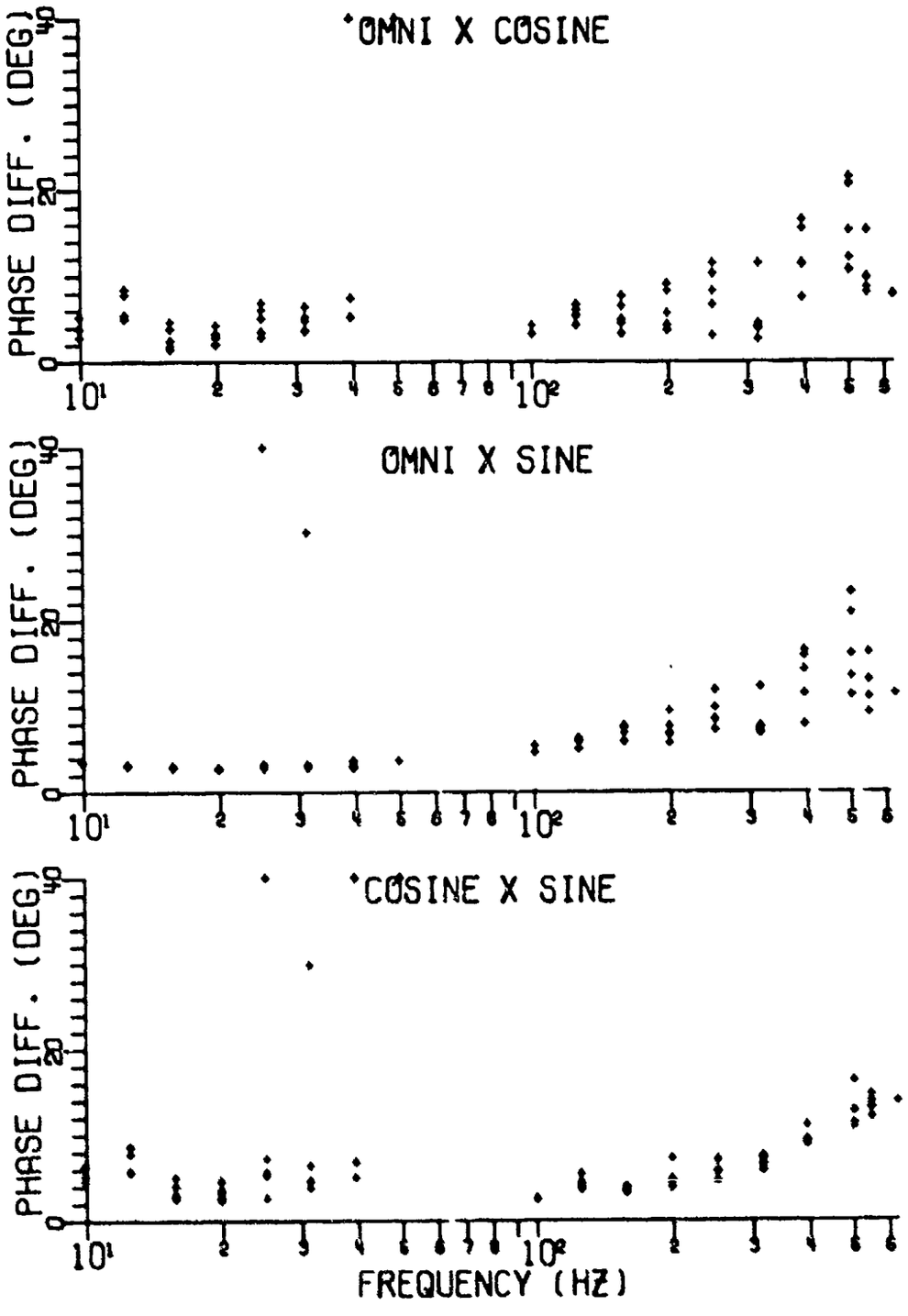

Figure A-11

AS-79-64

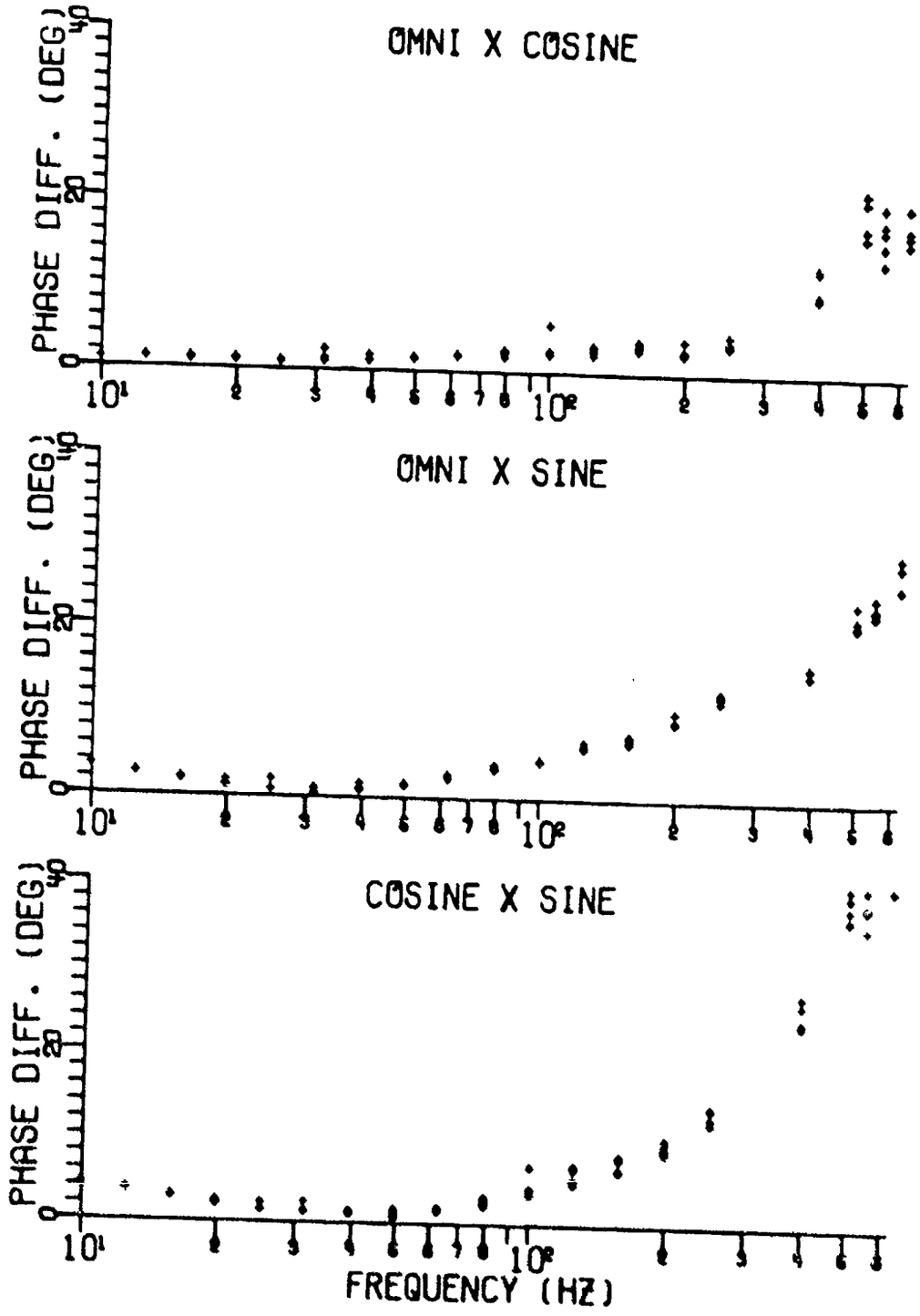

Figure A-12

AS-79-65

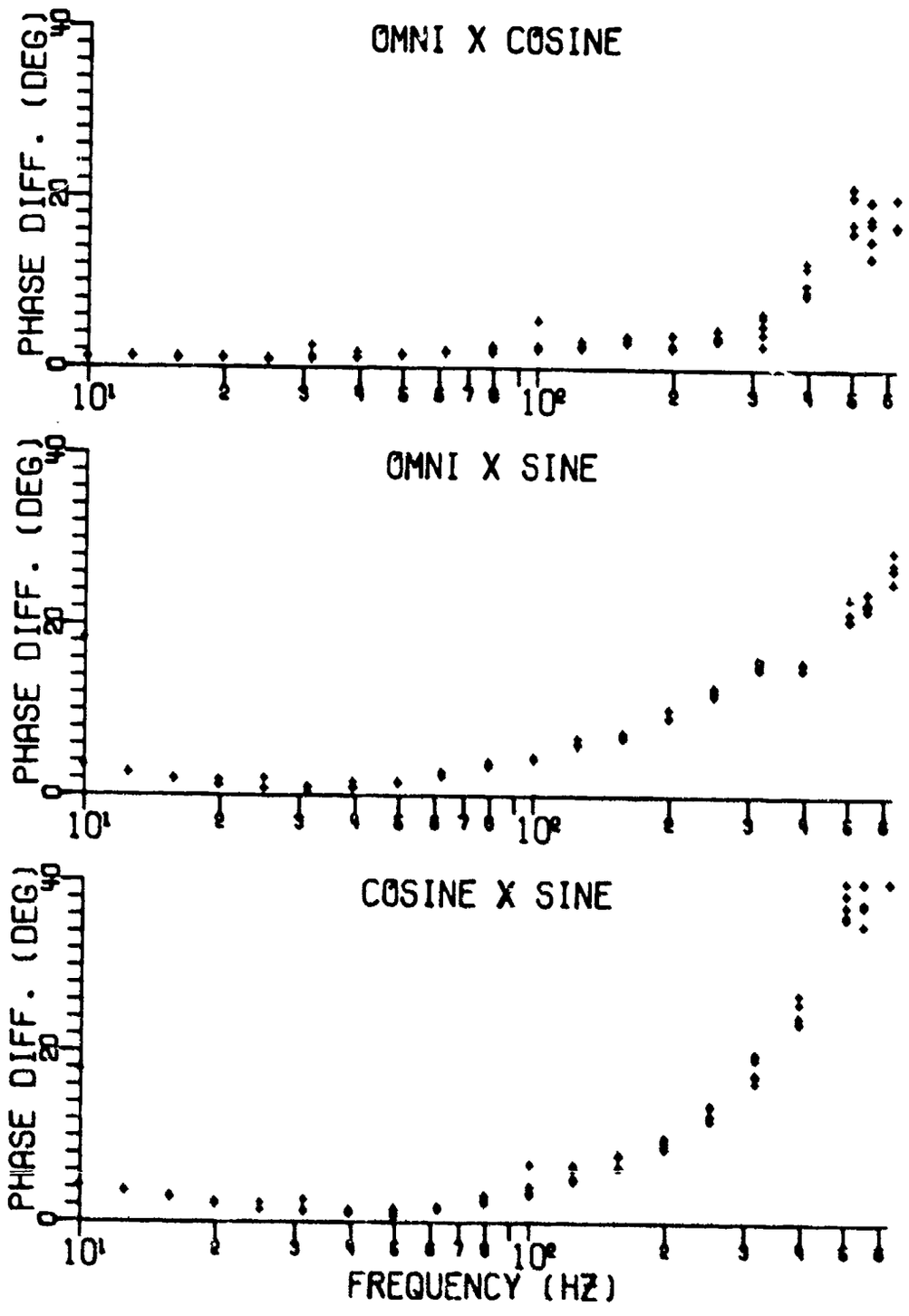

Figure A-13

AS-79-66

APPENDIX I-B

STATISTICAL STABILITY OF AMBIENT SOUND FIELD MEASUREMENTS

(The reverse of this page is blank.)

(U) An estimate of the statistical stability of the ambient sound field (ASF) measurements reported in this study can be obtained by modeling the ASF as a stationary Gaussian random process. The output of a FFT processor, such as that used herein, for such input will follow a distribution which can be closely approximated by a chi-square distribution (Ref. 15). The chi-square distribution is completely specified by a single parameter, the number of degrees of freedom. In this appendix, results will be shown regarding the number of equivalent degrees of freedom possessed by an estimate of the average amount of power of a Gaussian random noise process in a given frequency band, where the estimate is to be obtained by combining adjacent bins of a higher resolution power spectrum estimate. (The number of equivalent degrees of freedom (EDF) of an estimate refers, as usual, to the chi-square approximation to the actual distribution of the estimate.) The results are derived in Ref. 16, where it is shown that, when the high resolution spectral estimates are obtained by averaging 50% overlapped FFTs, the number of equivalent degrees of freedom of an estimate of the power in a band containing K+1 FFT bins is given by

(U)

$$EDF = \frac{2PI_0^2\left\{\sum_{k=-\frac{K}{2}}^{\frac{K}{2}} a_k\right\}^2}{\sum_{k=-\frac{K}{2}}^{\frac{K}{2}}\sum_{\ell=-\frac{K}{2}}^{\frac{K}{2}} a_k a_\ell\left[I_1^2(k,\ell) + \frac{2(P-1)}{P} I_2^2(k,\ell)\right]} \quad , \qquad \text{(B1)}$$

(U) where

(1) $$I_o = \int_{-\infty}^{\infty} |W(f)|^2 df ,$$

(2) $$I_1(k,\ell) = \left| \int_{-\infty}^{\infty} W(f)W^*(f+\Delta_{k,\ell})df \right|,$$

(3) $$I_2(k,\ell) = \left| \int_{-\infty}^{\infty} W(f)W^*(f+\Delta_{k,\ell})e^{j\pi Lf}\, df \right|,$$

(4) P is the number of FFTs used to form the high resolution spectral estimate,

(5) L is the length of each FFT in seconds,

(6) $$\Delta_{k,\ell} = \frac{k-\ell}{L},$$

(7) $a_{-\frac{K}{2}}, \ldots, a_{\frac{K}{2}}$ are the weighting coefficients assigned to the FFT

(8) bins which are summed to produce the estimate, and

(9) W(f) is the spectral window employed.

(U) For Hanned spectra,

$$W(f) = \frac{L\ \mathrm{sinc}(Lf)}{2\left[1-(Lf)^2\right]} \quad ,$$

and a numerical evaluation of the integrals $I_1(k,\ell)$ and $I_2(k,\ell)$ yields

$$|I_1(k,\ell)|^2 = \begin{cases} 1.40625 \times 10^{-1}\ L^2 \ , & k = \ell \\ 6.25000 \times 10^{-2}\ L^2 \ , & |k-\ell| = 1 \\ 3.90625 \times 10^{-3}\ L^2 \ , & |k-\ell| = 2 \\ = 0 \ , & |k-\ell| \geq 3 \end{cases}$$

and

$$|I_2(k,\ell)|^2 = \begin{cases} 3.90625 \times 10^{-3}\ L^2 \ , & k = \ell \\ 2.81448 \times 10^{-3}\ L^2 \ , & |k-\ell| = 1 \\ 9.76562 \times 10^{-4}\ L^2 \ , & |k-\ell| = 2 \\ 1.12579 \times 10^{-4}\ L^2 \ , & |k-\ell| = 3 \\ = 0 \ , & |k-\ell| \geq 4 \end{cases} \quad .$$

A straightforward computation for I_o gives

$$I_o = 1.40625 \times 10^{-1}\ L^2 \quad .$$

(U) Substituting back into Eq. (B2), we have, for Hanned spectra,

$$EDF = \frac{2.8125 \times 10^{-1}\, P\left\{\sum_{k=-\frac{K}{2}}^{\frac{K}{2}} a_k\right\}^2}{\sum_{i=0}^{3}\left\{C_i\left[\sum_{\substack{k,\ell \\ |k-\ell|=i}} a_k a_\ell\right]\right\}} \quad , \tag{B2a}$$

where

$$C_0 = 1.40625 \times 10^{-1} + \frac{2(P-1)}{P}(3.90625 \times 10^{-3}) \quad , \tag{B2b}$$

$$C_1 = 6.25000 \times 10^{-2} + \frac{2(P-1)}{P}(2.81448 \times 10^{-3}) \quad , \tag{B2c}$$

$$C_2 = 3.90625 \times 10^{-3} + \frac{2(P-1)}{P}(9.76562 \times 10^{-4}) \quad , \text{ and} \tag{B2d}$$

$$C_3 = \frac{2(P-1)}{P}(1.12579 \times 10^{-4}) \quad . \tag{B2e}$$

(U) This result was used to compute the EDF for each frequency band from which ASF measurements were obtained. Selected percentile levels denoting the spread of the corresponding chi-square distribution about its mean value were plotted in Fig. I-19.

(U) Equation B(2) was also used to predict the statistical variation in noise gain which could be expected in the absence of a signal when the noise process was isotropic, stationary, and Gaussian. Here the

(U) noise gain Z(f) is defined as the ratio $\chi(f)/Y(f)$, where $\chi(f)$ is an estimate of the noise power contained in a frequency band about f as measured by a directional receiver, and Y(f) is the corresponding estimate for a nondirectional receiver. In this case, 50% overlapped Hanned FFTs were used to form estimates of the power spectra for both the directional and nondirectional receivers. It was desired to convert the standard uniform resolution of these spectral estimates to logarithmic resolution by dividing the frequency range into 1/10-octave bands and summing all the FFT bins in each band (with uniform weighting across the band). Using Eq. (B2), the number of degrees of freedom ν for the approximating chi-square distribution could be determined for both $\chi(f)$ and Y(f) for each 1/10-octave band. Then, assuming the directional and nondirectional measurements were statistically independent, standard techniques can be applied to show

$$P\left\{Z(f) \leq z\right\} = \int_0^\infty \int_0^{yz} f(x)f(y)dxdy \quad ,$$

where

$$f(x) = \begin{cases} \left[2^{\nu/2}\Gamma\left(\frac{\nu}{2}\right)\right]^{-1} x^{\nu/2-1}e^{-x/2} \quad , & x > 0 \\ 0 \quad . & x \leq 0 \end{cases} \quad .$$

This integral was evaluated numerically for several values of z, and the results were also plotted in Fig. I-19.

(The reverse of this page is blank.)

APPENDIX I-C

BIAS OF BACKGROUND AMBIENT SOUND FIELD MEAN LEVEL ESTIMATOR IN THE ABSENCE OF ANY SIGNALS

(The reverse of this page is blank.)

(C) The background ambient sound field (ASF) mean level estimator used by the cw signal processor in this study was based on a clipper/ replacement technique. The sound pressure level (SPL) of each frequency cell which exceeds a clipping threshold is replaced by an estimate of the medium SPL. A frequency band of the clipped spectrum is then averaged to estimate the mean background ASF SPL. When no signals are present, the clipping of high level ASF levels will result in the background estimator being biased low. The amount of bias, for stationary Gaussian input data, will now be derived.

(U) When stationary Gaussian data is processed by a FFT technique such as that used in this study, the distribution of the output spectra is closely approximated by the product of a chi-square distribution (χ^2_γ) and a scaling term which can be neglected in what follows. The mean value of the distribution is

$$E[x(f)] \approx \int_0^\infty x\, \chi^2_\gamma(x)\,dx$$

$$= \gamma \quad ,$$

where γ is the number of degrees of freedom defining the chi-square discribution.

(C) Define the clipping threshold (T_c) and replacement value T_R as

$$T_c = \gamma C_c$$

and

$$T_R = \gamma C_R \quad ,$$

where C_c and C_R are termed the clipper and replacement coefficients and are chosen to set the clipper threshold and replacement values at the desired probabilities (P_c and P_R). The expected value of the clipped spectrum is

$$E[x_c(f)] = \int_0^{T_c} x\, \chi^2_\gamma(x)dx + \int_{T_c}^{\infty} T_R\, \chi^2_\gamma(x)dx \quad ,$$

where

$$\chi^2_\gamma(x) = \left[2^{\gamma/2}\Gamma\left(\frac{\gamma}{2}\right)\right]^{-1} x^{\gamma/2-1}e^{-x/2} \quad .$$

The bias of the ASF estimate is

$$\text{bias} = \frac{E[x_c(f)]}{E[x(f)]}$$

$$= \left[\gamma 2^{\gamma/2}\Gamma\left(\frac{\gamma}{2}\right)\right]^{-1} \int_0^{T_c} x^{\gamma/2} e^{-x/2}dx + C_R(1-P_c) \quad .$$

For values of γ which are even integers, the bias becomes

$$\text{(C) bias} = \left[\gamma 2^{\gamma/2}\,\Gamma\left(\frac{\gamma}{2}\right)\right]^{-1}\left[e^{-T_c/2}\sum_{k=0}^{\gamma/2}(-1)^K\frac{(\gamma/2)!\;T_c^{(\gamma/2)-K}}{\frac{\gamma}{2}-K!\left(-\frac{1}{2}\right)^{K+1}} - (-1)^{\gamma/2}\frac{(\gamma/2)!}{\left(-\frac{1}{2}\right)\frac{\gamma}{2}+1}\right.$$

$$\left. + C_R(1-P_c)\right] \quad .$$

(U) This function is plotted in Fig. I-24 as a function of γ and P_c for a replacement coefficient corresponding to a probability of 50%.

(The reverse of this page is blank.)

31 December 1978

DISTRIBUTION LIST FOR
ARL-TR-78-1
FINAL REPORT UNDER CONTRACT N00039-77-C-0003, ITEMS 0003 AND 0004
SECRET

Copy No.

Commander
Naval Electronic Systems Command
Department of the Navy
Washington, DC 20360
1 Attn: PME 124
2 PME 124-30
3 PME 124-40
4 PME 124-60
5 PME 124TA
6 EI 320

7 Office of Assistant Secretary of the Navy
(RE&S) Room 5E813, Pentagon
Washington, DC 20360
Attn: Mr. G. Cann

Chief of Naval Operations
Department of the Navy
Washington, DC 20350
8 Attn: OP-095
9 OP-951F
10 OP-951F1
11 OP-981

Commander
Naval Air Development Center
Department of the Navy
Warminster, PA 18974
12 Attn: Code 3091
13 Code 303

14 Commander
Naval Air Systems Command
Department of the Navy
Washington, DC 20360
Attn: Code PMA-264A

Dist. List for ARL-TR-78-1 under Contract N00039-77-C-0003, Items 0003 and 0004 (Cont'd)

Copy No.

15 Commanding Officer
Naval Intelligence Support Center
4301 Suitland Road
Washington, DC 20390
Attn: Code 222

16 Project Manager
Anti-Submarine Warfare Systems Project Office
Department of the Navy
Washington, DC 20360
Attn: ASW 01T

Commanding Officer
Naval Ocean Research and Development Activity
Department of the Navy
NSTL Station, MS 39529
17 Attn: S. Marshall, Code 340
18 G. Lewis, Code 500

19 - 20 Commanding Officer and Director
Defense Documentation Center
Cameron Station, Building 5
5010 Duke Street
Alexandria, VA 22314

21 TRW, INC.
TRW Defense and Space Systems Group
Washington Operation
7600 Colshire Drive
McLean, VA 22101
Attn: W. Morley

22 Sanders Associates, Inc.
95 Canal Street
Nashua, NH 03606
Attn: L. Gagne

23 Office of Naval Research
Resident Representative
Room 508, Federal Building
Austin, TX 78701

24 Glen E. Ellis, ARL:UT

25 Loyd D. Hampton, ARL:UT

Dist. List for ARL-TR-78-1 under Contract N00039-77-C-0003, Items 0003 and 0004 (Cont'd)

Copy No.

26 Kenneth E. Hawker, ARL:UT

27 Stephen K. Mitchell, ARL:UT

28 Clark S. Penrod, ARL:UT

29 Jack A. Shooter, ARL:UT

30 Library, ARL:UT

DEPARTMENT OF THE NAVY
OFFICE OF NAVAL RESEARCH
875 NORTH RANDOLPH STREET
SUITE 1425
ARLINGTON VA 22203-1995

IN REPLY REFER TO:

5510/1
Ser 321OA/011/06
31 Jan 06

MEMORANDUM FOR DISTRIBUTION LIST

Subj: DECLASSIFICATION OF LONG RANGE ACOUSTIC PROPAGATION PROJECT (LRAPP) DOCUMENTS

Ref: (a) SECNAVINST 5510.36

Encl: (1) List of DECLASSIFIED LRAPP Documents

1. In accordance with reference (a), a declassification review has been conducted on a number of classified LRAPP documents.

2. The LRAPP documents listed in enclosure (1) have been downgraded to UNCLASSIFIED and have been approved for public release. These documents should be remarked as follows:

   Classification changed to UNCLASSIFIED by authority of the Chief of Naval Operations (N772) letter N772A/6U875630, 20 January 2006.

   DISTRIBUTION STATEMENT A: Approved for Public Release; Distribution is unlimited.

3. Questions may be directed to the undersigned on (703) 696-4619, DSN 426-4619.

BRIAN LINK
By direction

Subj: DECLASSIFICATION OF LONG RANGE ACOUSTIC PROPAGATION PROJECT (LRAPP) DOCUMENTS

DISTRIBUTION LIST:

NAVOCEANO (Code N121LC – Jaime Ratliff)
NRL Washington (Code 5596.3 – Mary Templeman)
PEO LMW Det San Diego (PMS 181)
DTIC-OCQ (Larry Downing)
ARL, U of Texas
Blue Sea Corporation (Dr.Roy Gaul)
ONR 32B (CAPT Paul Stewart)
ONR 321OA (Dr. Ellen Livingston)
APL, U of Washington
APL, Johns Hopkins University
ARL, Penn State University
MPL of Scripps Institution of Oceanography
WHOI
NAVSEA
NAVAIR
NUWC
SAIC

Declassified LRAPP Documents

Report Number	Personal Author	Title	Publication Source (Originator)	Pub. Date	Current Availability	Class.
Unavailable	Penrod, C. S., et al.	MOORED SURVEILLANCE SYSTEM FIELD VALIDATION TEST SENSOR PERFORMANCE ANALYSIS. VOLUME I. DATA COLLECTION AND MESUREMENT SYSTEM DESCRIPTION	University of Texas, Applied Research Laboratories	781231	ADC018009	C
Unavailable	Watkins, S. L., et al.	MOORED SURVEILLANCE SYSTEM FIELD VALIDATION TEST SENSOR PERFORMANCE ANALYSIS. VOLUME III. VERNIER RESOLUTION DATA PRODUCTS	University of Texas, Applied Research Laboratories	781231	ADC018373	C
Unavailable	Watkins, S. L., et al.	MOORED SURVEILLANCE SYSTEM FIELD VALIDATION TEST SENSOR PERFORMANCE ANALYSIS. VOLUME II. STANDARD RESOLUTION DATA PRODUCTS	University of Texas, Applied Research Laboratories	781231	ADC018374	C
NORDATN44	Bucca, P. J.	ENVIRONMENTAL VARIABILITY DURING THE CHURCH STROKE II CRUISE FIVE EXERCISE (U)	Naval Ocean R&D Activity	790201	ADC020353; NS; AU; ND	C
NADC7820830	Balonis, R. M.	TEST STEERED VERTICAL LINE ARRAY (TSVLA) MEASUREMENTS FOR BEARING STAKE SURVEYS (U)	Naval Air Systems Command	790301	ADC018003; NS; ND	C
USIControl674779	Williams, W., et al.	REPORT OF THE LRAPP EXERCISE PLANNING WORKSHOP TRACOR INC ROCKVILLE MD 16 - 17 OCTOBER 1978 (U)	Underwater Systems, Inc.	790302	NS; ND	C
NOSCTR357	Hamilton, E. L., et al.	GEOACOUSTIC MODELS OF THE SEAFLOOR: GULF OF OMAN, ARABIAN SEA, AND SOMALI BASIN (U)	Naval Ocean Systems Center	790615	ND	C
Unavailable	Unavailable	RAPIDLY DEPLOYABLE SURVEILLANCE SYST (RDSS) ACOUSTIC VALIDATION TEST (AVT) EXERCISE PLAN (U)	Naval Electronic Systems Command	790625	AU	C
LRAPPRC79027	Brunson, B. A., et al.	GULF OF MEXICO AND CARIBBEAN SEA DATA AND MODEL BASE REPORT (U)	Tracor, Inc.	790701	ADC019153; NS; ND	C
Unavailable	Unavailable	BEARING STAKE BMS DATA QUALITY ASSESSMENT REPORT (U)	University of Texas, Applied Research Laboratories	790705	AU	C
PME12430	Unavailable	RAPIDLY DEPLOYABLE SURVEILLANCE SYSTEM (RDSS) ACOUSTIC VALIDATION TEST (AVT) DATA REDUCTION AND ANALYSIS PLAN (U)	Naval Electronic Systems Command	790815	NS; AU	C
Unavailable	Unavailable	RAPIDLY DEPLOYABLE SURVEILLANCE SYSTEM (RDSS) ACOUSTIC VALIDATION TEST (AVT) EXERCISE PLAN (U)	Naval Electronic Systems Command	790917	AU	C
NOSCTR467	Pedersen, M. A., et al.	PROPAGATION LOSS ASSESSMENT OF THE BEARING STAKE EXERCISE (U)	Naval Ocean Systems Center	790928	ADC020845; NS; AU; ND	C
NOSCTR466	Anderson, A. L., et al.	BEARING STAKE ACOUSTIC ASSESSMENT (U)	Naval Ocean Systems Center	790928	ADC020797; NS; AU; ND	C